GEORG-AUGUST-UNIVERSITÄT
GÖTTINGEN

Fakultät für
Physik

Master's Thesis

Signal modelling and corresponding uncertainty studies for the search of the Higgs boson produced in association with a top-quark pair at the ATLAS experiment

Signal Modellierung und dazugehörige Unsicherheitsstudien für die Suche nach dem Higgs Boson in assoziierter Produktion mit einem Top-Quark Paar am ATLAS Experiment

prepared by

Steffen Henkelmann

from Osterode am Harz

at the II. Physikalischen Institut

Thesis number:	II.Physik-UniGö-MSc-2013/02
Thesis period:	1. April 2013 until 30. September 2013
First Referee:	Prof. Dr. Arnulf Quadt
Second Referee:	Prof. Dr. Ariane Frey

Abstract
The Higgs boson production in association with a top-quark pair provides key features to further investigate the nature of the recently discovered new boson at the LHC. Whereas its coupling to other bosons was discovered, evidence for its coupling to fermions is owing. The associated $t\bar{t}H$ production with the Higgs decay $H \to b\bar{b}$ provides a good opportunity to probe its coupling strength to top and bottom quarks in the production and decay, respectively.
In order to improve the signal sensitivity of the search, multivariate analysis techniques are used to enhance the background and signal separation power relying on persuasive signal and background models. Therefore, dedicated studies of the $t\bar{t}H$ signal predictions by various Monte Carlo generators at different orders in QCD perturbation theory including differing features are ascertained and presented in this thesis. The $t\bar{t}H$ signal model by POWHEL at NLO QCD accuracy is identified to provide a solid signal prediction with high theoretical accuracy including the evaluation of systematic uncertainties.

Zusammenfassung
Die assoziierte Higgs Boson Produktion mit einem Top-Quark Paar stellt wichtige Schlüsselmerkmale bereit, um die Natur des kürzlich entdeckten Bosons zu untersuchen. Obwohl die Kopplung dieses Teilchens an andere Bosonen bereits entdeckt wurde, steht der Beweis für dessen Kopplung an Fermionen noch aus. Die assoziierte $t\bar{t}H$ Produktion mit dem Higgszerfall $H \to b\bar{b}$ stellt eine gute Möglichkeit dar, um dessen Kopplungsstärke an Top Quarks in der Produktion und Bottom Quarks im Zerfall zu erforschen.
Für eine Verbesserung der Signalsensitivität werden multivariate Analysetechniken verwendet. Diese gewährleisten eine Erhöhung der Trennungskraft zwischen Signal und Untergrund und hängen von zuverlässigen Signal und Untergrund Modellen ab. Aus diesem Grund werden in dieser Masterarbeit Studien für die Signalvorhersagen verschiedener Monte Carlo Generatoren einschließlich unterschiedlicher Eigenschaften für das $t\bar{t}H$ Signal in verschiedenen Ordnungen der QCD Störungstheorie untersucht. Das $t\bar{t}H$ Modell von POWHEL, beschrieben in der nächst-führenden Ordnung in der QCD Störungstheorie, konnte als solides Signalmodell mit hoher theoretischer Genauigkeit identifiziert werden. Darüber hinaus wurden die dazugehörigen systematischen Unsicherheiten bestimmt und bewertet.

—Für meine Eltern.

CONTENTS

CHAPTER

ONE

INTRODUCTION

> Wir fühlen, dass selbst, wenn alle möglichen wissenschaftlichen Fragen beantwortet sind, unsere Lebensprobleme noch gar nicht berührt sind. Freilich bleibt dann eben keine Frage mehr; und eben dies ist die Antwort.
>
> —*Ludwig Wittgenstein: Logisch-Philosophische Abhandlung. Tractatus Logico Philosophicus. Frankfurt a.M.: Suhrkamp 1963*

The extraordinary and dedicated physics program pursued at the Large Hadron Collider (LHC) at CERN succeeded in the observation of a new particle in the search for the Standard Model (SM) Higgs boson as announced on the 4^{th} July 2012 by both the ATLAS [1] and the CMS [2] collaborations with a local significance of 5.9 and 5.0 standard deviations, respectively, at a mass of around $m_H = 125$ GeV. The observation was mainly driven by the combination of di-bosonic decay modes of the Higgs boson, $H \to \gamma\gamma$, $H \to ZZ^{(\star)}$ and $H \to W^+W^-$. The dominant production mechanism of the Higgs boson is the gluon-gluon fusion ($gg \to H$) where the Higgs boson couples to gluons through a heavy quark loop. The analyses of ATLAS (CMS) was based on data sets corresponding to 4.8 (5.1) fb^{-1} collected at $\sqrt{s} = 7$ TeV in 2011 and 5.8 (5.3) fb^{-1} at $\sqrt{s} = 8$ TeV in 2012. However, no significant excesses were observed for fermionic decay modes such as $H \to b\bar{b}$ or $H \to \tau^+\tau^-$ so far.

It is of eminent importance to investigate the production and decay modes as well as fundamental properties predicted by the SM to understand the nature of the Higgs boson. Thus, searches for a signal in a wide mass range and testing whether the possible signal excess is consistent with the recently observed Higgs mass of around 125 GeV are necessary.

The dominant decay mode of a SM Higgs boson is $H \to b\bar{b}$ for low Higgs mass regions (up to around 135 GeV). The main challenge when investigating this decay is the tremendous multijet background. The latter prevents searching for an isolated Higgs boson in the $gg \to H \to b\bar{b}$ channel. Hence, the associated production of a Higgs boson with a vector boson (WH, ZH) or a top-quark pair ($t\bar{t}H$) is considered when searching for the Higgs boson in the $H \to b\bar{b}$ channel [3–10].

The production of a Higgs boson in association with a top-quark pair is furthermore sensitive to the Yukawa coupling between the Higgs boson and the top-quark. The masses of the fermions are generated by Yukawa couplings between the Higgs and the fermion fields where the coupling strength is proportional to the fermion masses. Therefore, the top quark is expected to couple most strongly to the Higgs boson either via Higgs radiation or top-quark fusion [11–13]. Moreover, the $t\bar{t}H$ process can open a window to distinguish different new physics contributions in the top-quark and Higgs sector when sufficient sensitivity will be achieved [14]. Hence, the $t\bar{t}H$ process is both challenging due to the large background and the relatively small production rate, and is providing access to a large variety of physics aspects that have the opportunity to uniquely extend and sharpen our understanding of nature.

The ATLAS collaboration performed a search for the Higgs production in association with a top-quark pair. The analysis used data recorded at 7 TeV corresponding to an integrated luminosity of 4.7 fb^{-1} and focused on the ℓ+jets decay mode of the $t\bar{t}$-system. The scalar sum of the jet transverse momenta H_T and the invariant mass of the b-quarks originating from the Higgs $m_{b\bar{b}}$ were used to set a limit on the Higgs production cross-section [9]. The $t\bar{t}H$ analysis of the full data set collected in 2011 and 2012 at 7 TeV and 8 TeV, respectively, is planned to include the ℓ+jets, the dileptonic and the fully hadronic decay mode of the $t\bar{t}$-system. In addition, instead of using a single variable approach, the analysis is striving to use multivariate analysis (MVA) techniques for a better separation between signal and background and to gain sensitivity to a Higgs boson signal by including all possible decay modes. The MVA uses complex variables for the signal and background separation that strongly rely on the validity of modelling variables. Thus, the investigation of a persuasive $t\bar{t}H$ signal model serving a description with high theoretical accuracy and the evaluation of associated signal uncertainties is important. The former and the latter present the scope of this master thesis.

The thesis is organised as follows. Chapter 2 gives an overview of the theoretical background of particle physics starting with general concepts becoming more specific with regard to the thesis' prospect. Chapter 3 briefly discusses the LHC and the ATLAS detector. A short summary of the $t\bar{t}H$ analyses is given in Chapter 4 and a selection of studies that were performed concerning the evaluation of the $t\bar{t}H$ signal modelling and corresponding systematic uncertainties can be found in Chapter 5. Chapter 6 includes a summary, conclusions and an outlook.

CHAPTER
TWO

THEORETICAL OVERVIEW

This chapter provides an introduction to the Standard Model of Particle Physics and particle production at the LHC. Furthermore, a short overview on top-quark physics, Higgs physics and on the $t\bar{t}H$ phenomenology is given.

2.1. The Standard Model of Particle Physics

All fundamental interactions (excluding gravity) and the known elementary particles are described by relativistic quantum field theories. Each elementary particle, assumed to be point-like, is associated with a field that holds suitable Lorentz group transformation properties depending on the quantum numbers of the particle. The set of forces shown in Table 2.1 (excluding gravity) is described by a gauge theory that is called the Standard Model of Particle Physics (SM) [15–19] and forms the theoretical basis of elementary particle physics since the mid-seventies. The SM is experimentally tested

interaction	boson	mass [GeV]	Q [e]	range [m]
strong	Gluon g	0	0	$2.5 \cdot 10^{-15}$
electromagnetic	Photon γ^*	0	0	∞
weak	Z^0	91.188 ± 0.002 [20]	0	10^{-18}
	$W^\pm$	80.388 ± 0.023 [20]	± 1	
gravity	(graviton G)	0	0	∞

Tab. 2.1.: The interactions and exchange particles described by the SM (except gravity) with their according mass, charge and range.

with extraordinarily high precision and describes three of the four fundamental forces of nature, namely the electromagnetic, the weak and the strong force. The fundamental particles are organised according to their spin properties (see Figure 2.2). The first type of particles are vector bosons with spin 1 and the second type are referred to as fermions constituted of quarks and leptons carrying half-integer spin.

2.1.1. Gauge fields and interactions

The fundamental interactions are mediated by vector bosons. Due to the fact that the SM is formulated as a gauge theory, the interactions can be expressed by local gauge symmetries that are either described by unitary $U(N)$ or special unitary $SU(N)$ Lie groups. The former have N^2 generators while the latter have $N^2 - 1$ generators reflecting the number of gauge bosons that are associated with the corresponding group. The SM interactions are determined by the gauge group

$$SU(3)_C \times SU(2)_L \times U(1)_Y, \tag{2.1}$$

that is a combination of the strong and the electroweak interaction. The group has $8 + 3 + 1 = 12$ non-commuting generators. Hence, the SM is represented as a non-Abelian gauge theory and incorporates twelve gauge bosons.

The strong interaction

The $SU(3)_C$ gauge group, also called the "colour" group (as implied by the index C), represents the strong force that is described by quantum chromo dynamics (QCD). The eight gauge bosons that are associated to the $SU(3)$ colour generators are called gluons. Those mediators of the strong force are massless, colour-charged (colour and anti-colour) and do not carry electromagnetic charge. Hence, gluons couple only to colour-charged fermions (quarks) and are self-interacting due to the non-Abelian structure of QCD. In QCD, the strength of the measured strong coupling $\alpha_S = g^2/4\pi$ depends on the so-called process or probing scale Q^2 (see Section 2.2). It is given by the leading-order equation:

$$\alpha_S(Q^2) = \frac{1}{b \ln\left(Q^2/\Lambda^2_{\mathrm{QCD}}\right)}, \tag{2.2}$$

where b is a known constant depending on the number of quark flavours at a certain probing scale Q^2 and $\Lambda_{\mathrm{QCD}} \approx 200$ MeV represents the QCD confinement scale parameter[1]. In quantum theory large momenta imply short wavelengths:

$$\lambda\!\!\!^{-} = \frac{\hbar}{\sqrt{Q^2}}, \tag{2.3}$$

as manifested by de Broglie [21]. The strength of the strong coupling $\alpha_S(Q^2)$ decreases for increasing Q^2 (or short distances) and vanishes asymptotically. Thus, at large energy scales ($Q^2 \gg \Lambda^2_{\mathrm{QCD}}$), quarks behave like free particles (*asymptotic freedom*) and the usage of perturbation theory in QCD (pQCD) becomes valid [22,23]. In this case, the potential between two colour-charged particles is similar to the Coulomb potential $\alpha_S(r)/r$. The opposite is the case if low energies and thus large distances are ascertained. In that scenario, the strength of the strong coupling becomes large and "free" quarks

[1]This scale parameter describes the transition region where perturbative QCD devolves in a non-perturbative regime and was determined by measurements.

start to form bound states which is referred to as *confinement*. Due to this confinement restrictions, they form quantum states with compensating colour charges so that they have a net colour charge of zero at sufficiently low energies ($Q^2 \lesssim \Lambda^2$). These kinematic regimes are described by non-perturbative theories. Particles that are composed of a quark and an anti-quark ($q\bar{q}$) are called mesons whereas particles built of three quarks (qqq) are called baryons. In general, particles composed by quarks are called hadrons, after "hadrós", the Greek word for "strong" [18,19,24,25].

The electroweak interaction

The electroweak interaction described by the $SU(2)_L \times U(1)_Y$ symmetry group unifies the electromagnetic and the weak interaction as proposed by Glashow, Weinberg and Salam in 1967 [15–17]. The index L of the gauge group $SU(2)_L$ implies that the weak isospin current couples exclusively to left-handed fermions due to the "vector minus axial vector" coupling ($V - A$) structure of the weak theory (see also Section 2.3.1). The electric charge can be expressed as the sum of one of the generators of the $SU(2)$ group (the third component of the isospin T_3) and the generator of the $U(1)$ group (the weak hypercharge Y):

$$Q = T_3 + Y/2, \tag{2.4}$$

which is referred to as the Gell-Mann-Nishijima relation. The four gauge bosons of the electroweak interaction are represented by massless fields. The group $SU(2)_L$ consists of an isotriplet of gauge fields W_i^μ with $i = 1,2,3$, whereas the $U(1)_Y$ consists of an isosinglet gauge field B^μ. The electroweak symmetry breaking introduces the mixing of these fields to the mass eigenstates resulting in fields which are a linear combination of the gauge fields $W_{1,2,3}^\mu$ and B^μ and that incorporate the massless photon γ and the massive $W^\pm$ and Z^0 boson:

$$W^{\pm\mu} = \frac{1}{\sqrt{2}} \left(W_1^\mu \mp i W_2^\mu \right). \tag{2.5}$$

The third gauge field assigned to the $SU(2)_L$ mixes with the singlet gauge field B^μ

$$\begin{array}{l} \text{photon}: \\ Z^0: \end{array} \begin{pmatrix} A^\mu \\ Z^\mu \end{pmatrix} = \begin{pmatrix} \cos\theta_W & \sin\theta_W \\ -\sin\theta_W & \cos\theta_W \end{pmatrix} \cdot \begin{pmatrix} B^\mu \\ W_3^\mu \end{pmatrix}, \tag{2.6}$$

where θ_W describes the Weinberg mixing angle that connects the masses of the weak gauge bosons. The coupling constants g and g' of the $SU(2)_L \times U(1)_Y$ define θ_W as follows:

$$\cos\theta_W = \frac{g}{\sqrt{g^2 + g'^2}}, \quad \sin\theta_W = \frac{g'}{\sqrt{g^2 + g'^2}}, \quad M_Z = \frac{M_W}{\cos\theta_W}. \tag{2.7}$$

The Weinberg angle θ_W has a measured value of $\sin^2\theta_W = 0.21316 \pm 0.00016$ [20]. The electric charge e can be expressed in terms of θ_W, $e = g\sin\theta_W = g'\cos\theta_W$. At the electroweak scale, the $SU(2)_L \times U(1)_Y$ breaks down into the subgroup $U(1)_Q$ which

remains symmetric and thus the photon γ remains massless. This is the reason why the electromagnetic interaction has an infinite range. The photon is of neutral charge and couples only to charged fermions. The fields $W^{\mu}_{1,2}$ and thus the associated massive $W^{\pm}$ bosons which carry electromagnetic charge couple only to left-handed particles. The field B^{μ} couples to both left- and right-handed fermions. Consequently, the same applies to the associated Z^0 boson that is of neutral charge and the photon γ, though with a different coupling strength. Due to the large mass of the electroweak gauge bosons, the weak force has only a limited range and dominates exclusively at high energies. Table 2.1 depicts the relative strength of the different interactions.
Nevertheless, the SM Lagrangian needs to preserve local gauge invariance which results in the condition that gauge bosons need to be massless. Only the γ and the eight gluons of the former listed gauge bosons are massless because the symmetry that is induced by the three generators that are associated to the massive $W^{\pm}$ and Z^0 boson is spontaneously broken. This can be described by the so-called *Higgs mechanism* (see Section 2.1.2) that predicts the existence of a particle explaining the origin of the gauge boson masses and possibly of the other fundamental particles as well: the Higgs boson.

2.1.2. The Higgs mechanism

The introduction of the Higgs mechanism ensures the existence of mass terms for the weak gauge bosons and fermions without giving up the principle of local gauge invariance. The mediators of the electromagnetic (γ) and the strong force (g) appear to be massless and thus do not require mass terms in the SM Lagrangian. Experimental measurements have shown that this is not the case for the gauge bosons of the weak force ($W^{\pm}$, Z^0). Due to the fact that the introduction of mass terms for gauge bosons breaks gauge invariance, a mechanism needs to be implemented in the theory to explain the spontaneous symmetry breaking. This mechanism was introduced by Peter Higgs, Robert Brout, Francois Englert, Gerald Guralnik, Carl R. Hagen and Thomas W.B. Kibble [26–28]. They showed that the combination of a gauge theory with an additional scalar field that introduces spontaneous symmetry breaking, results in a consistent theory with gauge bosons having a non-zero rest mass. Thus, a mechanism was developed that can describe the generation of particle masses by spontaneous symmetry breaking without violating the gauge invariance of the SM Lagrangian. The explicit choice of the Higgs potential results in a breaking of the $SU(2)_L \times U(1)_Y$ symmetry that is called spontaneous symmetry breaking. The subgroup $U(1)_Q$ remains symmetric and therefore the γ remains massless. By choosing the Higgs field as a complex scalar $SU(2)$ doublet

$$\phi(x) = \begin{pmatrix} \phi^+(x) \\ \phi^-(x) \end{pmatrix} = \sqrt{\frac{1}{2}} \begin{pmatrix} \phi_1(x) + i\phi_2(x) \\ \phi_3(x) + i\phi_4(x) \end{pmatrix} \tag{2.8}$$

the underlying electroweak theory has four degrees of freedom (d.o.f.). Three of the d.o.f.'s are absorbed by the longitudinal polarisation of the gauge bosons. Figure 2.1 shows an illustration of a potential where the lowest energy state is non-zero and therefore the symmetry of the potential is broken by choosing an arbitrary ground state

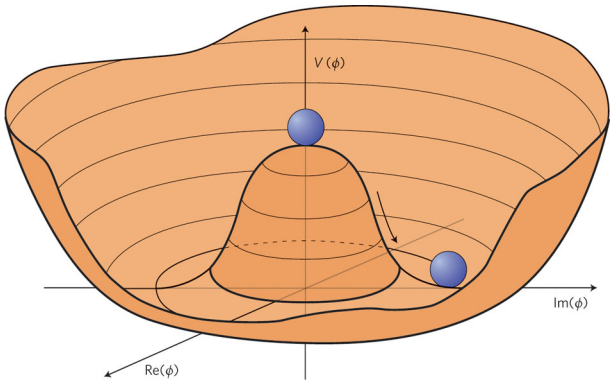

Fig. 2.1.: The illustration of a Higgs potential. A symmetrical potential where the ground state is not equal to zero and thus the potential obtains a non-zero vacuum expectation value accompanied by a spontaneous symmetry breaking.

(*electroweak symmetry breaking*). As it is shown in Figure 2.1, the polarisation modes along the circle correspond to the electroweak gauge bosons that acquire mass terms due to the finite expectation value and the gauge field terms, whereas the transverse mode (the left d.o.f.) corresponds to a Higgs boson which arises by a perturbation transverse to the circle. There are several mechanisms in several theories accompanied by the existence of a field that provides new particles. The simplest mechanism consistent with the SM provides the existence of just one Higgs boson with spin 0. It is predicted to have neither charge nor colour. The fundamental particles in the SM acquire masses by interacting with the Higgs field. The Higgs Yukawa coupling to fermions ($g_{\phi \mathrm{ff}}$) and vector bosons ($g_{\phi \mathrm{VV}}$) is proportional to the mass of the particles:

$$g_{\phi \mathrm{ff}} \sim m_{\mathrm{f}}/v \text{ and } g_{\phi \mathrm{VV}} \sim 2M_{\mathrm{V}}^2/v, \tag{2.9}$$

where $v = (\sqrt{2}G_F)^{-1/2} \simeq 246$ GeV is the vacuum expectation value (ground state of the Higgs field). $G_F \sim g^2/8m_W^2$ denotes the fermi constant and its most precise experimental determination arises from the measurement of the lifetime of the muon [29].

2.1.3. Field content

The introduced gauge fields form the basis for interactions with fermions. The fermionic matter fields of the SM are quarks (Q_L^i, u_R^i or d_R^i) and leptons (L_L^i or ℓ_R^i) where the index $i = 1, 2, 3$ denotes the different generations of the fermions. The number of fermions is equal to the number of anti-fermions that have the same mass but opposite charge and weak isospin values. The quark doublet Q_L^i comprises an up- (u, c, t) and a down-type (d, s, b) quark which have a charge of either $q = +2/3$ or $q = -1/3$ in units of the elementary charge e. Each quark is a colour triplet which means that each quark flavour exists in three colours (r, g or b). Leptons are colourless and thus do not interact strongly but they have electroweak charges. The lepton doublet L_L^i, in particular, contains an electrically neutral neutrino and a charged lepton $q = -e$. Assuming the neutrinos to be massless, their chirality is always left-handed. This results in the existence of

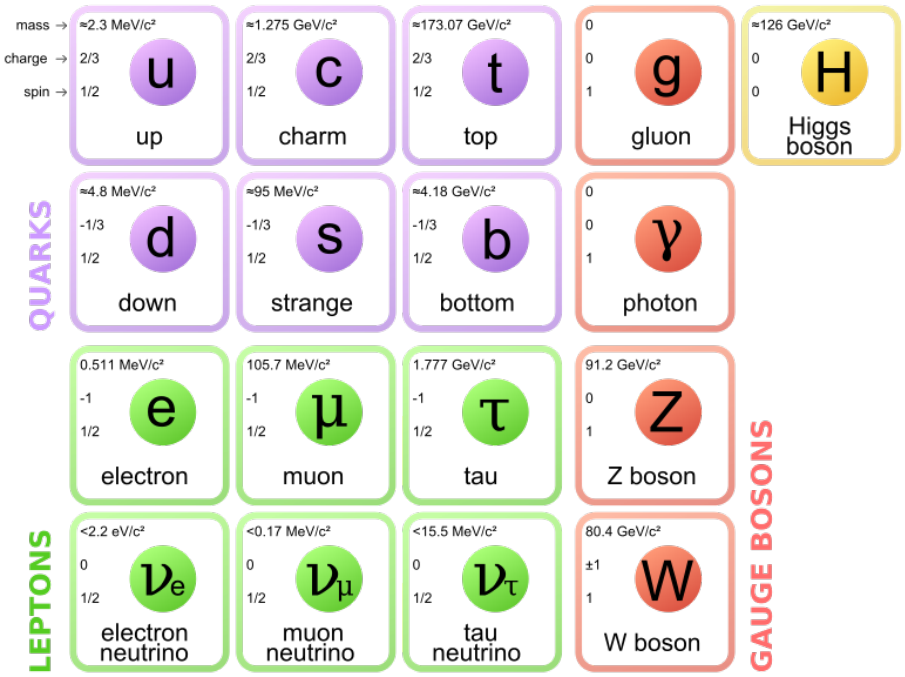

Fig. 2.2.: The elementary particles predicted by the SM including the mass, charge and spin information.

fermions	fields	generation i 1	2	3	Y	T_3	Q [e]	colour
leptons	L_L^i	$\begin{pmatrix} \nu_e \\ e \end{pmatrix}_L$	$\begin{pmatrix} \nu_\mu \\ \mu \end{pmatrix}_L$	$\begin{pmatrix} \nu_\tau \\ \tau \end{pmatrix}_L$	-1	$+1/2$	0	-
					-1	$-1/2$	-1	-
	ℓ_R^i	e_R	μ_R	τ_R	-2	0	-1	-
quarks	Q_L^i	$\begin{pmatrix} u \\ d \end{pmatrix}_L$	$\begin{pmatrix} c \\ s \end{pmatrix}_L$	$\begin{pmatrix} t \\ b \end{pmatrix}_L$	$+1/3$	$+1/2$	$+2/3$	r,g,b
					$+1/3$	$-1/2$	$-1/3$	r,g,b
	u_R^i	u_R	c_R	t_R	$+4/3$	0	$+2/3$	r,g,b
	d_R^i	d_R	s_R	b_R	$-2/3$	0	$-1/3$	r,g,b

Tab. 2.2.: The fields of the SM with a selection of their quantum numbers, weak hypercharge Y, the third component of the weak isospin T_3, the electric charge Q and the colour [30].

only left-handed weak isospin doublets L_L^i and right-handed singlets ℓ_R^i (see Figure 2.2 and Table 2.2). The electromagnetic current couples to left-handed and right-handed types, whereas the weak currents only couple to left-handed states. The weak charged current vertices are unique in the SM as they change the flavour of the left-handed fermion fields. If an up-type quark u, defined in the mass eigenbasis, radiates a W^+, it turns into a down-type quark d' (the weak isospin partner of the up-type quark) in a weak eigenstate. The eigenstates of d'-type quarks are linear combinations of the mass eigenstates u. However, for the case of a non-vanishing rest mass of a particle, mass eigenstates and weak flavour eigenstates can be distinguished in the theory. If

the particles are not degenerated in terms of mass, an allocation of different bases for the interaction and the mass is possible. This theoretical construct is called *mixing*. It is described by two unitary matrices. On the one hand it is known as the *Cabibbo-Kobayashi-Maskawa* matrix V_{CKM} in the quark sector [31,32] and on the other hand it is described by the *Pontecorvo-Maki-Nakagawa-Sakata* matrix U_{PMNS} in the leptonic sector [33]. The former generates a unitary transformation between different eigenstates. The CKM matrix satisfies $VV^{\dagger} = \mathbb{1}$ and is defined as follows:

$$\begin{pmatrix} d' \\ s' \\ b' \end{pmatrix} = \begin{pmatrix} V_{ud} & V_{cd} & V_{td} \\ V_{us} & V_{cs} & V_{ts} \\ V_{ub} & V_{cb} & V_{tb} \end{pmatrix} \cdot \begin{pmatrix} d \\ s \\ b \end{pmatrix} = V_{\mathrm{CKM}} \cdot \begin{pmatrix} d \\ s \\ b \end{pmatrix}. \tag{2.10}$$

It acts on down-type quark mass-eigenstates for conventional reasons. It is constructed under the assumption that unitarity holds and only three quark generations exist in nature. The CKM-Matrix is determined by four parameters - three mixing angles and one complex CP-violating phase. This phase is the only source for CP-violation in the SM [34]. Due to the fact that the mass eigenstates and the weak eigenstates do not coincide (V $\neq \mathbb{1}$), transitions occur between the up- and down-type quarks within and across generations (flavour changing charged currents). The neutral current couplings where the Z boson mediates the weak interaction are diagonal in both bases and no deviation in form of the observation of flavour changing neutral currents (FCNC) is raised so far [35].
The PMNS matrix was introduced to explain the effect of neutrino oscillations [36,37] which are correlated to the mass of neutrinos. Since neutrinos are likely to have non-zero rest masses [20], the mass eigenstates $\mid \nu_i \rangle$ transform into the flavour eigenstates $\mid \nu_\alpha \rangle$ as follows

$$\mid \nu_\alpha \rangle = U_{\mathrm{PMNS}} \mid \nu_i \rangle \text{ and } \mid \nu_\alpha \rangle = \sum_i U_{\alpha i} \mid \nu_i \rangle,$$

where $|U_{\alpha i}|^2$ is proportional to the probability that a neutrino of a given flavour $\alpha = e, \mu, \tau$ is found in a specific mass eigenstate $i = 1, 2, 3$.

2.1.4. Shortcomings of the SM

The bulk of experimental data in particle physics supports the SM with high precision. Furthermore, precise predictions for new particles and decay channels being observed and measured are provided in the context of the SM. Nevertheless, there are a variety of phenomena that cannot be described by the SM, such as the hierarchy problem [38], the asymmetry between matter- and antimatter (recent results could resolve that question as suggested in Ref. [39]) and the origin of dark matter (there is a possibility that the recent excess of positrons observed by the AMS experiment is consistent with the signature of dark matter [40]). Dark matter and dark energy are known to account for the major part of the energy density of the universe and it is assumed that it is composed of a not yet discovered particle. A possible candidate according to supersymmetric models (SUSY) could be the lightest supersymmetric particle (LSP). In addition, the SM makes

no predictions for the unification of the three interactions and the gravity at the Planck scale ($\sim 10^{19}$ GeV). That and the fact that the SM contains 19 free parameters which cannot be explained by first principles is the reason why the SM is believed to be just an effective theory emerging from a more fundamental theory.
Moreover, the SM does not give a united description of the electroweak and the strong force which is predicted to occur at energies of $\sim 10^{16}$ GeV (see Figure 2.3). Theoretical

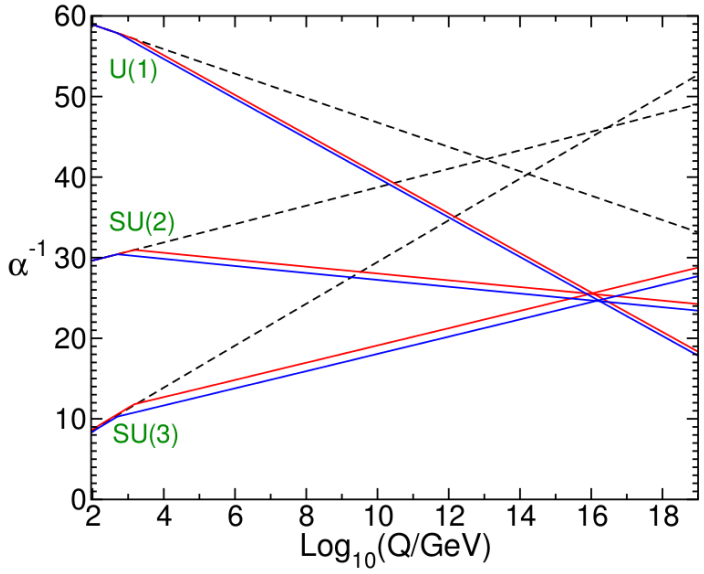

Fig. 2.3.: The inverse of the running coupling α_i^{-1} of the three interactions described in the SM (dashed lines) and for the MSSM (blue and red solid lines) with respect to the probing scale Q. The solid lines imply different assumptions for the masses of particles [38].

models such as SUSY, which assigns bosons supersymmetric fermionic partners, or grand unifying theories (GUTs) that are based on the assumption that all forces existing today have evolved from just one force existing at an early stage of the universe, have the potential to describe the unification of the strong and the electroweak force. Figure 2.3 illustrates the running coupling depending on the energy both for the SM (dashed lines) and for the *Minimal Supersymmetric Standard Model* – the MSSM (blue and red solid lines) [38,41,42]. A unification of all known forces is provided by theoretical frameworks such as quantum gravity or different string theories. The main problem with treating the gravity analogous to the other three interactions lies in the renormalisation of quantum field theories [43].

2.2. Particle production at the LHC

The hard scattering process at hadron colliders is driven by the interactions of the constituents of the colliding hadrons. Hence, in the case of the LHC in the proton-proton mode a profound knowledge of the internal structure of the proton is needed. Feynman proposed that the results in lepton-hadron scattering experiments for short distances (large momentum transfers Q^2) can be explained by the so-called *parton model* [44].

This model postulates that the proton inherently disposes of a structure that is made

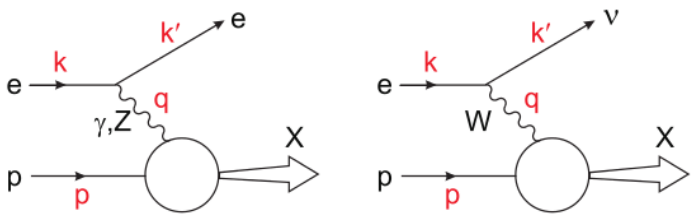

Fig. 2.4.: Neutral- and charged-current DIS mediated by γ, Z and W exchange, respectively [45]. The momentum transfer Q^2 is defined as $Q = q = k - k'$.

of point-like partons or constituents. Bjørken [46] formulated that these partons carry a finite fraction $0 < x < 1$ of the total momentum of the hadron which later became known as the Bjørken x. Elaborating on the former approaches, Drell and Yan [47]

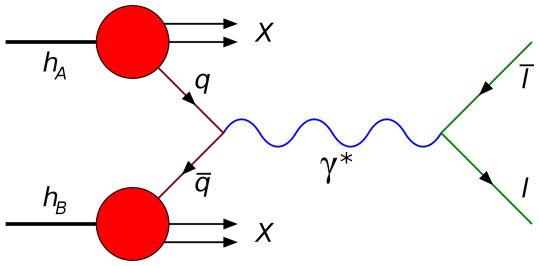

Fig. 2.5.: A Feynman diagram illustrating the Drell-Yan process.

suggested that the hadronic cross-section $\sigma(h_A h_B \to \ell^+\ell^-)$ is a convolution of the short distance hard scattering partonic cross-section $\hat{\sigma}(ij \to \ell^+\ell^-)$ for the partons of type i and j and the corresponding *parton distribution functions* (PDFs) $f_{i(j)/h_A(h_B)}(x_A(x_B))$ that depend on the Bjørken x:

$$\sigma_{h_A h_B} = \sum_{i,j} \int\int \mathrm{d}x_A \mathrm{d}x_B \, f_{i/h_A}(x_A) f_{j/h_B}(x_B) \, \hat{\sigma}(ij \to \ell^+\ell^-). \tag{2.11}$$

It was later shown in deep-inelastic scattering (DIS) experiments at SLAC and HERA that equation (2.11) only holds in the asymptotic scaling limit where $Q^2 \to \infty$ and x is fixed. It was observed that the measured cross-sections are eventually scale dependent which can be theoretically described using the approach of Dokshitzer-Gribov-Lipatov-Altarelli-Parisi (DGLAP equations). When applying the *factorisation theorem* [48] that allows the separation of non-perturbative (long distance) from perturbative (high energy) dynamics in QCD in certain kinematic regimes under the presence of a large hard

probing scale Q^2, the following equation is obtained:

$$\sigma_{h_A h_B} = \sum_{i,j} \int \int \mathrm{d}x_A \mathrm{d}x_B \, f_{i/h_A}(x_A, \mu_F^2) f_{j/h_B}(x_B, \mu_F^2) \, \hat{\sigma}(x_i, x_j, \mu_R^2). \tag{2.12}$$

This equation shows that the PDFs $f_{i(j)/h_A(h_B)}(x_A(x_B), \mu_F^2)$ are dependent on a certain scale μ_F^2 that is called *factorisation scale*. At that scale the short distance hard scattering cross-section is separated from the low momentum regime that is covered by the PDFs. The PDFs can be interpreted as the probability of finding a parton of type $i(j)$ in the hadron carrying a momentum fraction $x_A(x_B)$ when the hadron is probed at a certain scale $\mu^2 = Q^2$. The PDFs cannot be calculated by pQCD, thus they are extracted

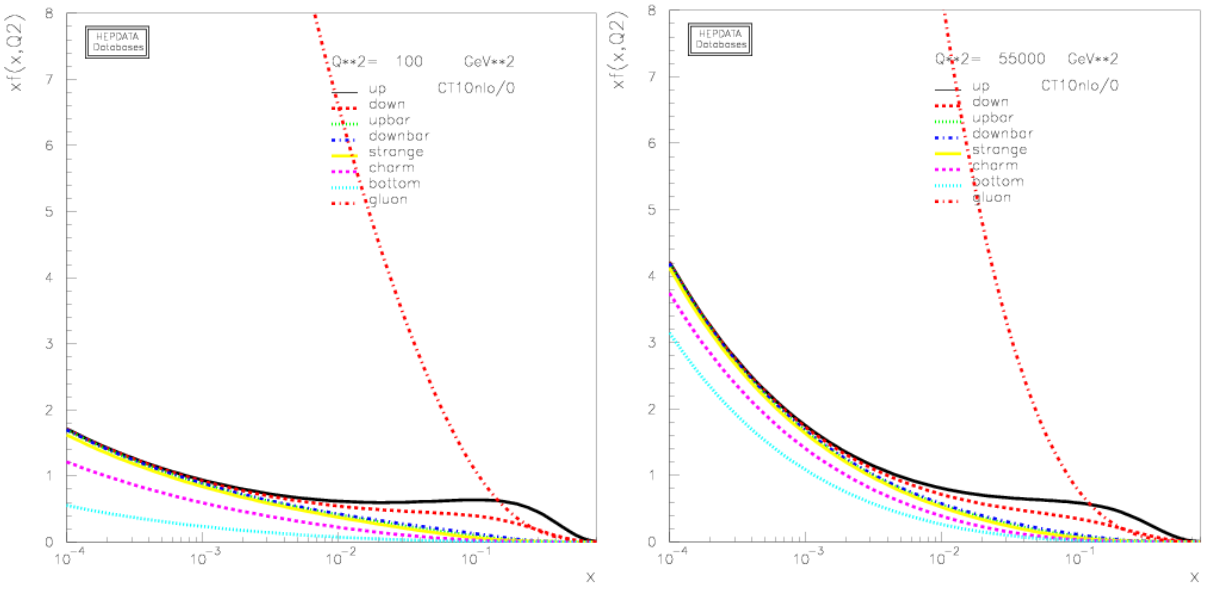

(a) *(b)*

Fig. 2.6.: CT10nlo PDFs at $Q^2 = 100\ \mathrm{GeV}^2$ (a) and $Q^2 = (m_t + m_H/2)^2 \approx 5.5 \cdot 10^4\ \mathrm{GeV}^2$ (b) [49].

from global QCD fits to data [50–53] mostly obtained in DIS ep collisions at the HERA accelerator at DESY. The DIS Feynman diagrams for neutral- and charged-current DIS are depicted in Figure 2.5. The PDFs for two different scales, parametrised as a function of x, that were obtained by the CTEQ collaboration [49] are shown in Figure 2.6. For large values of x, the quark PDFs dominate the gluon PDF while for small x the opposite is the case.

2.2.1. The hard scattering partonic cross-section

The hard scattering partonic cross-section or hard process $\hat{\sigma}_N^{ij}$ is essentially providing information on a specific N-particle final state in collisions of parton i with parton j and can depend on kinematic variables of particles that are produced in the hard-process such as energies, momenta and angles. The hard process is given by the following

phase-space integral over the differential cross-section:

$$\hat{\sigma}_N^{ij} = \int_{\text{cuts}} \mathrm{d}\hat{\sigma}_N^{ij} = \int_{\text{cuts}} \underbrace{\left[\prod_{i=1}^{N} \frac{\mathrm{d}^3 q_i}{(2\pi)^3 2E_i}\right] \delta^4\left(p_1 + p_2 - \sum_i^N q_i\right)}_{N\text{-dimensional phase space}} \underbrace{\left|\mathcal{M}^{ij}_{p_1 p_2 \to \vec{q}}\right|^2}_{\text{matrix element squared}} . \quad (2.13)$$

To calculate the hard scattering partonic cross-section, it is essential to compute the hard matrix element (ME) $\mathcal{M}^{ij}_{p_1 p_2 \to \vec{q}}$ fully differential and to integrate the output over the N-dimensional phase-space where N denotes the number of final state particles. The latter needs to be performed in an efficient way. Cuts on the phase-space regions can be applied to accelerate the computation. In the case of the LHC, the hard MEs are calculated at scales which need to be treated perturbatively. Thus, integrations over large phase-space regions can lead to many additional particles. The integrand $\mathrm{d}\hat{\sigma}_N^{ij}$ represents a weight for a specific kinematic configuration $p_1 p_2 \to \vec{q}$. This weight is used to produce fully differential events resulting in the partonic cross-section $\hat{\sigma}_N^{ij}$ after performing the integration. At leading-order and for processes that do not have high final-state particle multiplicities, the number of MEs that need to be calculated is rather small whereas for increasing orders in perturbation theory and particle multiplicities, the number of MEs that need to be taken into consideration significantly increases. Thus, sophisticated and automated computer programs are needed to build and calculate a large number of Feynman diagrams[2]. For higher-order processes the multidimensional phase-space integration becomes inefficient due to its time consumption and CPU intensity [54]. However, Monte Carlo (MC) methods can be used to reduce the event generation time. The partonic cross-section $\hat{\sigma}(x_i, x_j, \alpha_S(\mu_R^2), \mu_R^2)$ in equation (2.12) is expressed as a power series dependent on the renormalisation scale μ_R:

$$\hat{\sigma}(x_i, x_j, \mu_R^2) = \sum_{n=0}^{\infty} \hat{a}_n \alpha_S^n(\mu_R), \quad (2.14)$$

where $\hat{a}_n$ denotes the coefficient of the perturbative series at n^{th} order. The non-physical scale μ_R, that reflects the momentum scale at which particles couple to each other, are introduced in order to deal with infrared (IR) divergencies occurring at higher-orders in perturbation theory due to both real-radiation and virtual contributions. However, such divergencies must cancel out for the calculation of inclusive cross-sections following the KLN-theorem [55, 56]. For the calculation of exclusive cross-sections at a specific resolution scale, the divergencies remain at n orders in the perturbative expansion in form of terms including logarithms dependent on the ratio of the hard probing scale Q^2 and the chosen resolution scale μ^2:

$$g^{2n}(Q^2) \ln^{an}\left(\frac{Q^2}{\mu^2}\right), \quad (2.15)$$

[2] As depicted in Figure 2.24 in Section 2.5, nine subprocesses with 448 independent Feynman diagrams need to be calculated for the $t\bar{t}H$ process at NLO QCD accuracy.

where $g(Q^2) \sim 1/\ln(Q^2/\Lambda^2_{\mathrm{QCD}})$ is the running coupling and $a = 1$ or 2. The logarithmic terms appear in each order in the perturbation expansion and thus hinder the perturbation series to converge. The probing scale Q^2 determines the typical size of μ_F

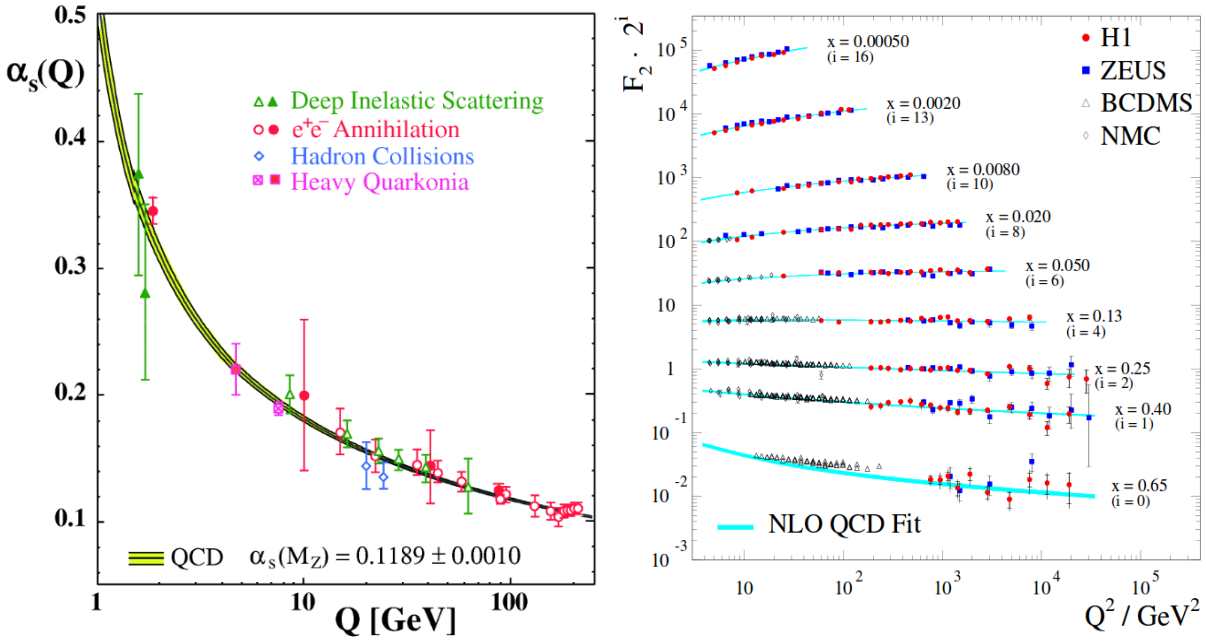

Fig. 2.7.: Summary of $\alpha_S(Q)$ measurements as a function of the energy scale Q (left) [57]. The summary of measurements of the structure function F_2 dependent on the momentum scale Q^2 (right) [58].

and μ_R since the logarithms and inherently the higher-order terms do not become sufficiently large if Q^2 is of order μ_F and μ_R. However, higher-order terms will not converge if the coupling constant $g(Q)$ that is expressed in inverse powers of the logarithms depending on the introduced scales is sufficiently high. To guarantee convergence of the perturbation series, the logarithmic terms need to be resummed to all orders which is either done analytically or numerically. The former approach is carried out by different substraction schemes, such as the FKS substraction scheme [59], that are used to serve as a universal formalism for the analytic cancellation of shower dependent IR singularities. The latter method is performed by the so-called parton shower (PS) Monte Carlo (MC) algorithm. Although the terms cancel out when taking into account all orders of the perturbative expansion, they remain when fixing the expansion at a certain order. Depending on the order at which order the perturbation series is fixed, the running coupling is referred to as having leading-order (LO), next-to-leading order (NLO), next-to-next-leading order (NNLO), etc. QCD accuracy.
The effect of the scales on physical observables can be seen in Figure 2.7. The strong coupling α_S illustrated in Figure 2.7a decreases with increasing $\mu_R = Q$ (asymptotic freedom) and the measured PDFs (see Figure 2.7b) increase slightly with $\mu_F^2 = Q^2$ (in regimes that are of interest at the LHC) [57].

2.2.2. Parton showers, hadronisation and decay

At the LHC, particles are produced at large scales or high energies which is described by the hard scattering partonic cross-section as described above. PSs ensure the evolution of those particles from their production scale to the so-called hadronisation scale (low energy) where pQCD is not valid anymore and effective non-perturbative theories are applicable. Hence, the PS approach can be connected to models that simulate the hadronisation and handle the decay of the formed hadrons universally and thus independent of the hard scattering partonic process. Hence, the particle generation is model

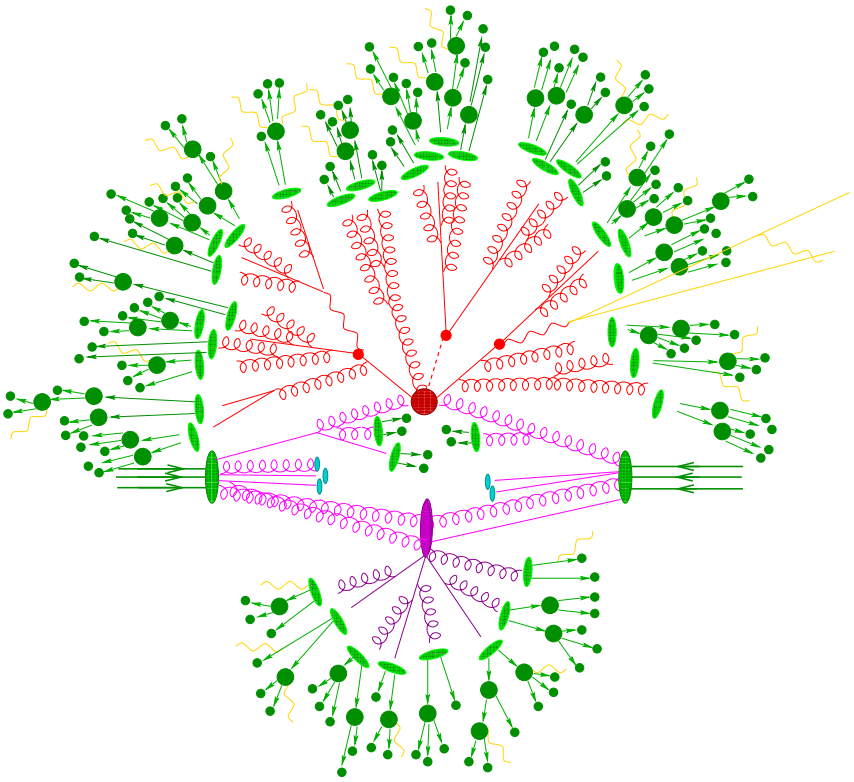

Fig. 2.8.: A sketch of the evolution of a $t\bar{t}H$ event after an initial hadronic collision. The different stages from the collision to the decay of stable hadrons is illustrated including various models.

dependent and factorises into different steps of event generation. Each step involves approximations and interfacing the different parts is essential to provide a full picture of the model of interest.
To illustrate the different generation steps, Figure 2.8 shows a collision of two hadrons producing a $t\bar{t}H$ final state. The dark green blobs represent the PDFs that describe the content of the incoming hadrons. The particles depicted by pink lines originate from the PDFs and most likely emit further gluons followed by the creation of quark-anti-quark pairs (QCD Bremsstrahlung). The factorisation scale μ_F serves to separate the part of the calculation that is described by the PDFs and the part which is described by the hard scattering process. The latter one is illustrated by the big red blob (located in the center of the Figure) and can be calculated at fixed orders in perturbation theory dependent

on the strong coupling α_S in QCD for example. This part is taken into account via the computation of the MEs that are embedded in special programs called *parton level* or *matrix element* generators.
The particles sketched in red are described by the PS and the process is called QCD evolution. As explained, the PS connects the particles produced at the hard scale carrying colour information after simulating appropriate QCD Bremsstrahlung processes to the primary colourless hadrons which start to form around the hadronisation scale (light green blobs). This transition is simulated by phenomenological hadronisation models such as string and cluster fragmentation which include free parameters that are fitted to data. After the hadronisation step, the primary hadrons are decayed into stable particles. Photon (yellow lines) and gluon radiation (curly lines) are taken into consideration at any stage, both as radiation off initial (ISR) and radiation off final state particles (FSR). The beam remnants can interact and a secondary or further hard interactions may occur (big purple blob) which are called underlying events (UE) caused by multi-parton interactions (MPI) [30, 48, 54, 60–64].

2.2.3. Higher-order contributions and scale variations

If the perturbation series was calculated retaining all orders in perturbation theory there would be no source of a theoretical uncertainty associated with the scales. Due to the fact that the theoretical calculations are performed only to a limited order in perturbation theory, the results obtained by the variation of the factorisation and the

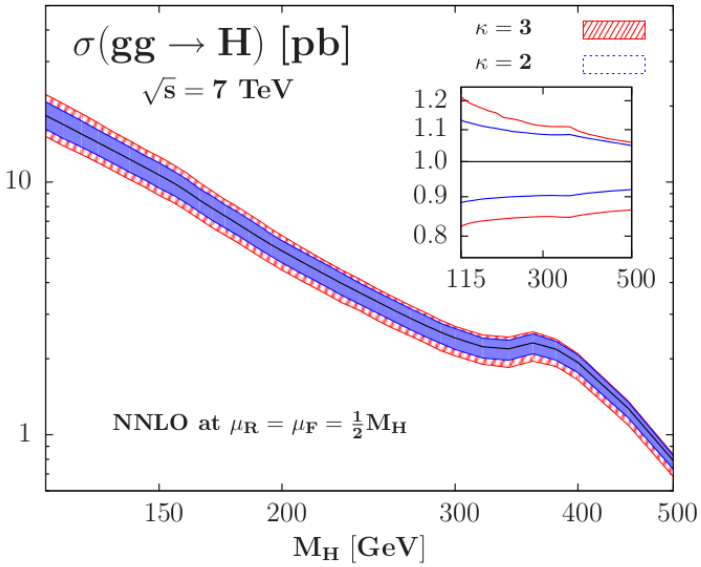

Fig. 2.9.: The scale uncertainty band of $\sigma^{\mathrm{NNLO}}(gg \to H)$ at the LHC as a function of M_H for scale variation in the domain $M_H/\xi \leq \mu_R, \mu_F \leq \xi \times M_H$ for $\xi = 2, 3$ [65].

renormalisation scales are considered to be an estimate of the unpredicted higher-order terms. To assign the theoretical uncertainty due to the chosen scales the nominal scale $\mu_0 = \mu_F = \mu_R$ used to obtain the central result is varied by a factor ξ within the interval

$\mu_0/\xi \leq \mu_R, \mu_F \leq \xi \times \mu_0$. The constant factor ξ is chosen to be $\xi = 2, 3, 4, \ldots$ which is rather subjective [65]. It is common to use a factor of $\xi = 2$. In some processes, it is sufficient to estimate missing contributions from virtual, initial or final state radiation. However, this is inadequate when important new processes appear at higher-orders. The accuracy of assigning the theoretical uncertainty to estimate the contributions of higher-order terms depends on whether the uncalculated terms are of the same size as the calculated ones. As explained in Section 2.2, the choice of the nominal scale μ_0 should anticipate divergencies for higher-order contributions. This can be ensured by keeping the product of equation (2.15) in Section 2.2 small. That is the case if the hard probing scale Q^2 is of the order of the resolution scale μ which is either the factorisation or the renormalisation scale in the processes that are of interest in this work. It is common to set $\mu_R = \mu_F$ but the values for both scales can also be chosen independently since the two scales might correspond to different kinematic regimes depicted by individual MEs. However, this underlines the subjectivity of the choice of the scale. The scale variations serve only as one possibility of estimating higher-order corrections. Procedures of applying theoretical uncertainties depend on the models and should be evaluated on a case-by-case basis. In general, for the calculation of the cross-section the order in QCD accuracy for both the used PDFs and the perturbative expansion in the hard partonic cross-section calculation must be the same. Figure 2.9

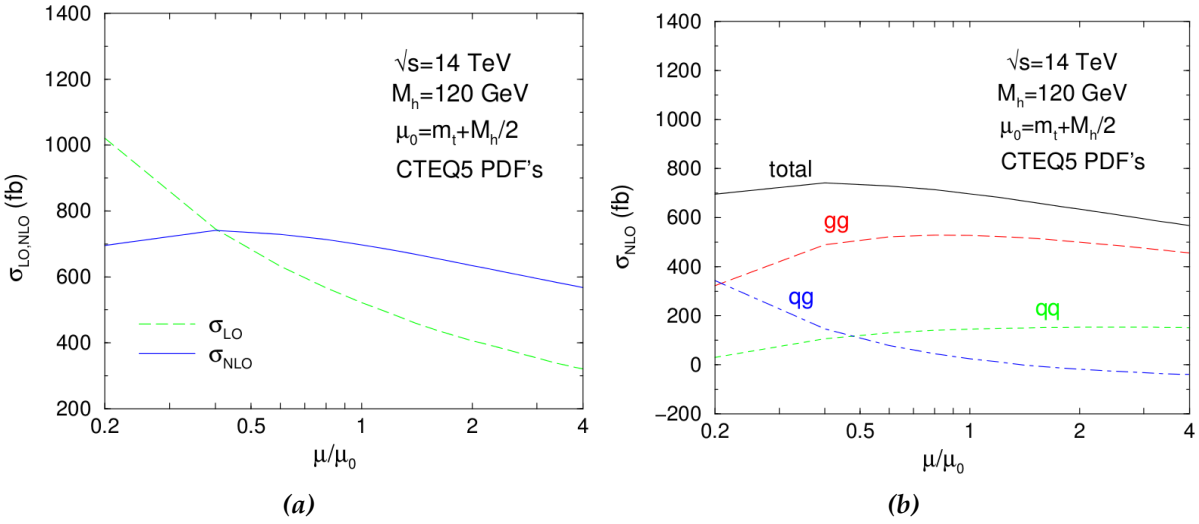

Fig. 2.10.: Dependence of $\sigma_{\mathrm{LO,NLO}}(pp \to t\bar{t}H)$ (left) and $\sigma_{\mathrm{NLO}}(gg\ q\bar{q}\ qg + \bar{q}g \to t\bar{t}H)$ (right) on the renormalisation/factorisation scale μ normalised to the nominal scale $\mu_0 = m_t + m_H/2$ for $\sqrt{s} = 14$ TeV and a SM Higgs mass of $m_H = 120$ GeV [66].

shows the application of the described procedure of varying the nominal scale by a factor of 2 for the $\sigma^{\mathrm{NNLO}}(gg \to H)$ process. The partonic cross-sections for gg fusion initiated processes are proportional to α_S^2 at LO. Thus, they decrease significantly as μ_R increases.
Figure 2.10a represents the dependence of $\sigma(pp \to t\bar{t}H)$ on the scale μ at LO (dashed-green) and NLO (solid blue) QCD accuracy normalised to the nominal scale $\mu_0 = m_t + m_H/2$. The nominal scale μ_0 will be referred to as the static scale in the following

since it does not depend on the individual event kinematic. A static scale is often chosen for processes that are probed at their production threshold, whereas dynamic scales are used for the description in regimes with higher transverse momentum p_{T}. The scales are set to $\mu = \mu_R = \mu_F$ since no significant deviation from the case where both scales were treated independently was observed for σ_{NLO}. The CTEQ5L (CTEQ5M) [67] is used for the LO (NLO) cross-section calculation. Figure 2.10a illustrates a weaker scale dependence for the NLO cross-section compared to the one at LO. The NLO prediction is more stable with respect to the choice of different scales than the one at LO. In general however, a residual dependence remains due to the unknown higher-order contributions. The variation of $\mu = \mu_R = \mu_F$ according to $\mu_0/\xi \leq \mu_R, \mu_F \leq \xi \times \mu_0$ with $\xi = 2$ implies a higher (lower) cross-section $\sigma_{\mathrm{NLO}}(\xi\mu_0)$ ($\sigma_{\mathrm{NLO}}(\mu_0/\xi)$) with respect to the nominal cross-section $\sigma_{\mathrm{NLO}}(\mu_0)$. Figure 2.10b shows the μ dependence of the cross-section at NLO for the individual production channels of the $t\bar{t}H$ process. Summing up the individual contributions results in the total NLO cross-section that is shown in Figure 2.10a. Beside the impact on the cross-section, the scale variation influences the shape of kinematic distributions. The shape differences occur due to the fact that the variation of the chosen scale affects the theoretical description of the process.
The impact of NLO corrections with respect to LO predictions is defined by the so-called K-factor:

$$K = \frac{\sigma_{\mathrm{NLO}}}{\sigma_{\mathrm{LO}}}. \tag{2.16}$$

Thus, Figure 2.10a suggests a K-factor larger than unity for values $\mu \geq 0.4\mu_0$ by assuming a SM Higgs mass of $m_H = 120$ GeV and a nominal scale of $\mu_0 = m_t + m_H/2$. This implies that the NLO corrections increase the LO cross-section for a wide spectrum of common choices of scales μ [66].

2.3. Top-quark physics

The top quark is the heaviest known elementary particle and is thus assumed to play a special role amongst the other quarks and leptons with regard to the mechanism of electroweak symmetry breaking. In 1973, the top quark was predicted by Kobayashi and Maskawa as the weak-isospin partner of the b-quark forming the basis to explain the observed $\mathcal{CP}$ violation in kaon decays [32]. According to the SM, the top quark is an up-type fermion transforming as a colour-triplet under the $SU(3)_C$ symmetry group. It was discovered in 1995 at the TEVATRON collider at FERMILAB [68, 69]. It has been predominantly studied in hadron-hadron collisions where it is mainly produced in pairs via strong interactions and it decays almost exclusively through the single mode $t \to Wb$ (see Section 2.3.3). Thus, the strong interaction can be probed in the top-quark pair production, whereas the weak interaction is measured in the top-quark decay and the production of single top quarks. The latter process was observed in 2009 by both the CDF [70] and the DØ [71] experiment at FERMILAB. The top quark serves as a multi-purpose physics standard candle at the LHC since the top-quark precision measurements drive improvements in the detector and physics tools understanding.

The data collected by the ATLAS experiment at 8 TeV includes $\sim$ 5.5 ($\sim$ 2.6) million top-quark pair (single-top) events which emphasises why the LHC is often referred to as a "top-factory". The top quark allows for stringent tests of the SM and its extensions, for probing the electroweak symmetry breaking and it enables for searches for physics beyond the SM (BSM). Due to its relatively high mass it has a correspondingly short life-time which results in the fact that it decays before forming hadrons:

$$\tau_t = \frac{1}{\Gamma_t(m_t = 172.5\,\text{GeV})} \sim 5 \times 10^{-25}\,\text{s} < \frac{1}{\Lambda_{\text{QCD}}}, \tag{2.17}$$

where Λ_{QCD} is the QCD confinement scale - the scale where quarks form bound states. Thus, the top quark is the only quark that provides the opportunity of investigating its "bare" properties. Furthermore, according to the SM, it is predicted to most likely couple to the Higgs boson with respect to other fermions (see Section 2.1.2).

2.3.1. Top-quark pair production

The production of top-quark pairs occurs mainly through two processes via the strong interaction at leading-order (LO) in pQCD – namely the gluon-gluon fusion (gg) and the quark-anti quark annihilation ($q\bar{q}$) process (see Figure 2.11). Since the constituents of the two colliding hadrons interact carrying a fraction x of the momentum of the parent hadron, it results in a reduced center-of-mass energy squared, $\hat{s} = x_1 x_2 s$. x_i is the momentum fraction carried by one constituent and s is the nominal center-of-mass energy squared (see a detailed description in Section 2.2). The top-quark pair

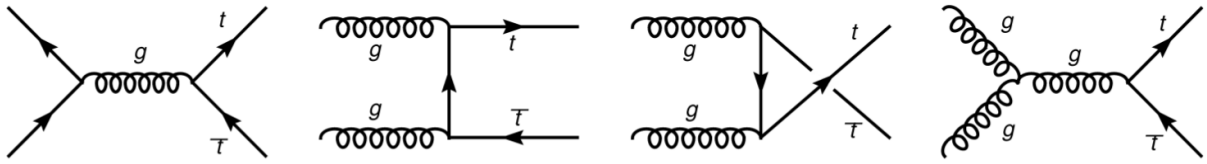

Fig. 2.11.: LO Feynman diagrams for the $t\bar{t}$ production in the $q\bar{q}$ annihilation (first on the left) and the gg fusion process (the remaining three).

production at the LHC is dominated by gg fusion rather than $q\bar{q}$ annihilation whereas at the TEVATRON the opposite was true. This is due to the PDFs describing the particle content of the colliding hadrons (a more detailed description can be found in Section 2.2). The higher the center-of-mass energy the smaller the momentum fraction x carried by the constituents of the colliding hadrons (see Figure 2.6 in Section 2.2). Thus, the interaction of particles dominant for small values of x becomes more likely. In the case of $t\bar{t}$ production assuming that the partons have an equal x the center-of-mass energy of

the collider needs to be sufficient to produce a top-quark pair at rest according to

$$\begin{aligned} x &\sim 2m_t/\sqrt{s}, \\ &\approx 0.19 \text{ at the TEVATRON Run I}, \\ &\approx 0.18 \text{ at the TEVATRON Run II}, \\ &\approx 0.043 \text{ at the LHC (8 TeV)}, \\ &\approx 0.025 \text{ at the LHC (14 TeV)}. \end{aligned}$$

Thus, at the LHC partons are probed with smaller average values of x compared to the TEVATRON. In regimes of small x, the gluon PDFs dominate the quark PDFs as depicted in Figure 2.6 in Section 2.2. One additional, more phenomenological argument is that valence-quarks (valence-anti quarks) are present in protons (anti-protons) colliding at the TEVATRON. Hence, the $q\bar{q}$ production mechanism is favoured whereas at the LHC that only collides protons, the anti quarks are available only as suppressed sea-quarks [30, 72].

2.3.2. Top-quark decay

The top quark decays almost exclusively into a W boson and a b-quark as the branching ratio $\mathcal{BR}(t \to Wb)$ is expected to be ~ 1 assuming three generations of quarks and the unitarity of the CKM matrix (see Section 2.3.3). This is experimentally underlined and described in Section 2.3.3. Thus, the top-quark pair final states will always contain two

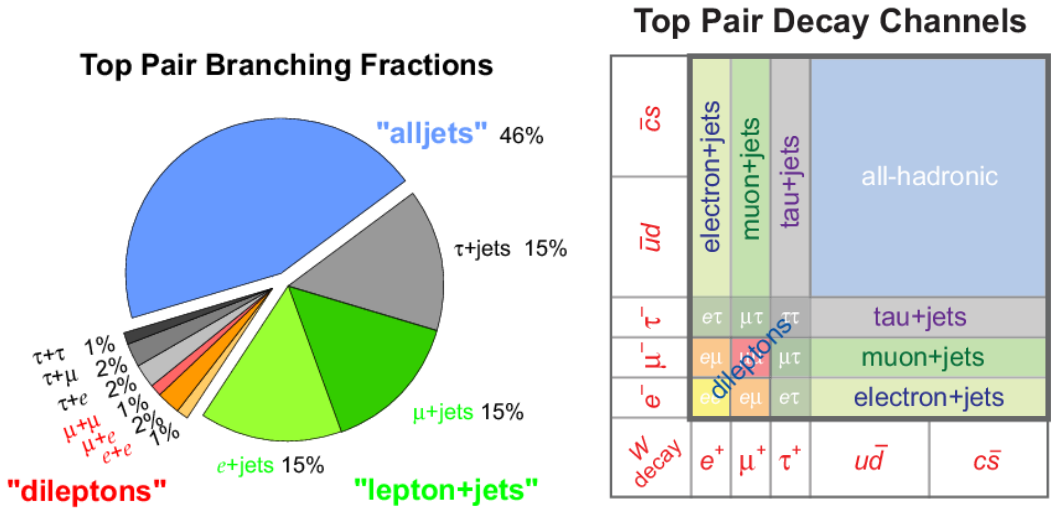

(a) *(b)*

Fig. 2.12.: The branching ratios for the $t\bar{t}$ pair decay (left) and the $t\bar{t}$ pair decay channels.

b-quarks and the decay products of the W bosons. The former particles will hadronise and form jets in the detector. These jets contain B hadrons that can further decay semileptonically after traveling a resolvable distance in the detector. Thus, by locating this so-called secondary vertex, displaced from the interaction point or primary vertex, it

is possible to distinguish between jets originating from the production of a b-quark and those originating from light quarks. This method is called b-tagging and is illustrated in Figure 2.13. Taking the decay of the two W bosons into account, the $t\bar{t}$ pair decay can be

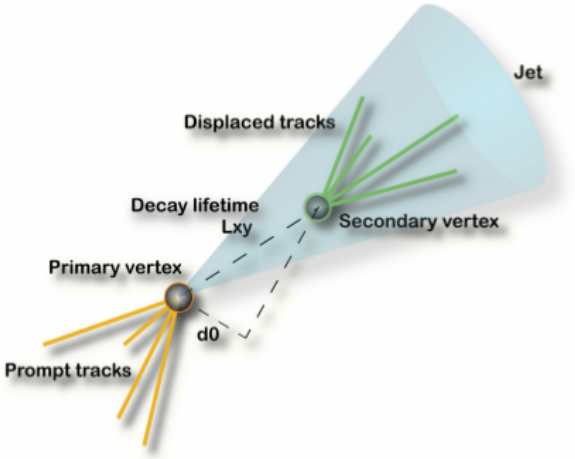

Fig. 2.13.: A sketch illustrating the displacement of the secondary from the primary vertex and the formation of jets [73].

classified by three different decay modes [20] (also illustrated in Figure 2.12):

All-hadronic channel

The all-hadronic decay channel contains only jets in the final state. Both W bosons decay hadronically. Hence, the total number of jets is six, four evolving from the W decay and two from the b-quark. This decay channel has a $\mathcal{BR} = 0.462$ and is characterised by an overwhelming QCD multijet background.

Lepton plus jets channel

In the lepton plus jets channel (ℓ+jets), one W decays leptonically (e, μ or τ and the corresponding neutrinos) and the other one decays hadronically. This results in four jets (two b-jets, two jets from the W), one high-p_{T} lepton and missing transverse energy $\not{E}_{\mathrm{T}}$. The τ lepton decays predominantly hadronically and in about 17 % leptonically ($\ell_i \bar{\nu}_{\ell_i} \nu_\tau$) where $i = e, \mu$. Hence, the reconstruction of the τ channel is a bit more challenging compared to the other decays. However, the leptonic decays of the τ contribute to the e/μ+jets channels. The dominant background process is W + jets. The ℓ + jets channel has a modest signal-over-background ratio and a high branching ratio $\mathcal{BR} = 0.435$. The ℓ + jets channel is often referred to as the "golden channel" since it has both a high branching ratio and a decay signature that can be separated from the large QCD background.

Dileptonic channel

The dilepton decay mode is defined via two leptons, missing transverse energy $\not{E}_{\mathrm{T}}$ and two b-jets in the final state. The two W's decay leptonically. Hence, two neutrinos

escape the detector (high $\not{E}_T$ contribution). Compared to the former decay modes, the dileptonic channel has the smallest background (mainly Z + jets) but the branching ratio is only $\mathcal{BR} = 0.103$.

2.3.3. A selection of top-quark properties

In general the properties of the top quark can be separated in two categories. The *intrinsic* properties refer to the top quark and its "bare" properties, and the other properties are defined by the top-quark pair production (see Section 2.3.1).

Mass

The *mass* of the top quark was measured by both the ATLAS and CMS experiments using 7 TeV data corresponding to an integrated luminosity of up to 4.9 fb^{-1} (see Section 2.3.2). Figure 2.14 shows the combination of mass measurements at the LHC from September 2013 compared to the combined results of the DØ and CDF experiment at the TEVATRON from March 2013 [74]. The respective TEVATRON and the LHC combination

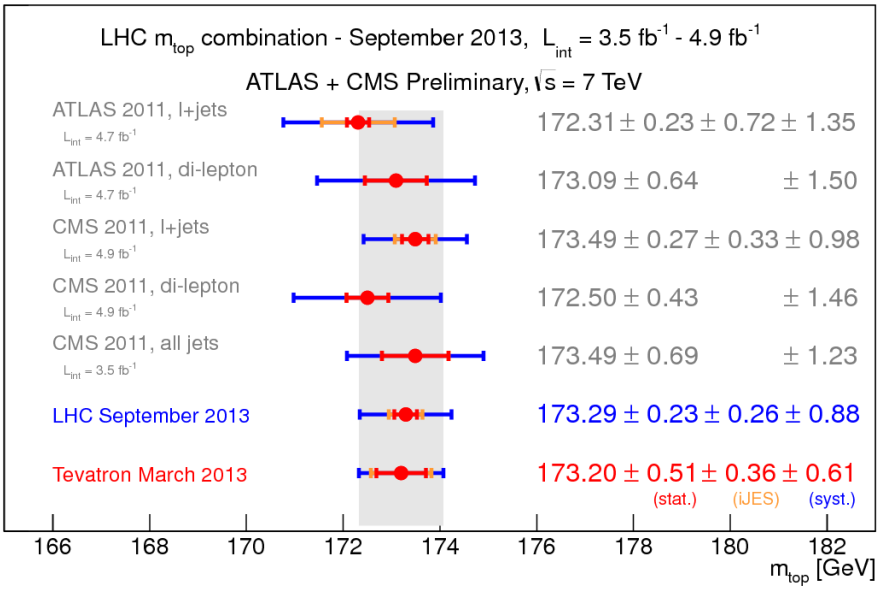

Fig. 2.14.: The LHC and TEVATRON combination for the measurement of the top-quark mass [75].

weres performed using the BLUE method [74,75] and yields $m_t = 173.29 \pm 0.23\,(\text{stat.}) \pm 0.92\,(\text{syst.})$ GeV [75] at the LHC. The LHC and the TEVATRON combinations are in good agreement. However, the measurement of the top mass runs into difficulties when the precision becomes smaller than the top width. This is due to arising problems when defining a pole mass for a coloured and unstable particle. The measurement can be potentially biased kinematically by taking the invariant mass of the decay products of the top quark as an observable for the mass measurement due to colour reconnection effects, ISR/FSR and the kinematics of the b-quark [76].

Charge

Last ATLAS results confirm the SM prediction for the top-quark *charge* that yields $Q_t = 0.64 \pm 0.02\ (\text{stat.}) \pm 0.08\ (\text{syst.})$ in units of the elementary charge e. A top-quark charge of $-4/3e$ as predicted by exotic models is excluded with a significance of more than 8 σ [77].

Width

The CDF experiment performed the first direct measurement of the top-quark *width*. It yields $\Gamma_t = 2.21^{+1.84}_{-1.11}$ GeV which corresponds to the following lifetime of the top quark:

$$\tau_t = 2.98^{+3.00}_{-1.35} \times 10^{-25}\ \text{s [78].} \tag{2.18}$$

The V_{tb} CKM matrix element (see Section 2.1) determines the coupling strength at the Wtb vertex. It was measured to be $|V_{tb}| = 1.04^{+0.10}_{-0.11}$ [79] which is consistent with unity. The measurement of the $\Gamma_{Wb}/\Gamma_q = 0.91 \pm 0.04$ [20] ratio where q is a running index for $q = d, s, b$ underlines the decay characteristics of the top quark.

Cross-Section

The top-quark pair production *cross-section* is measured with high precision (shown in Figure 2.15) and agrees with the theoretical predictions up to NNLO QCD accuracy ($\mathcal{O}(\alpha_S^4)$) [80]. The ATLAS combination for the 7 TeV yields $\sigma_{t\bar{t}} = 177^{+11}_{-10}$ pb [81,82].

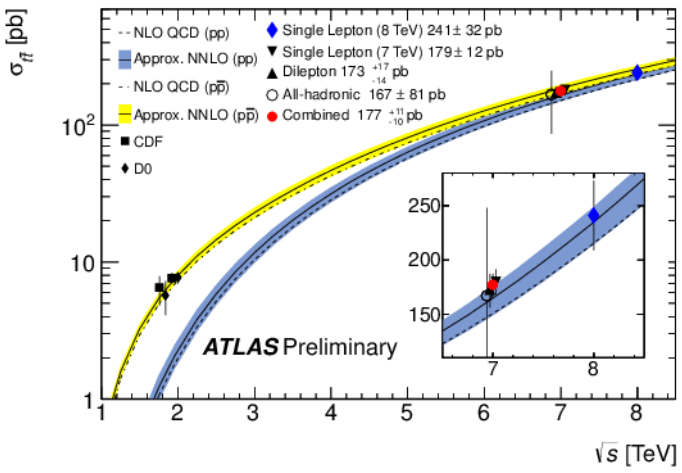

Fig. 2.15.: Summary plot showing the top pair production cross-section as a function of the LHC proton proton center of mass energy. The experimental results in the various top decay channels (and their combination) at 7 TeV and the recent result at 8 TeV are compared to an approximate NNLO QCD calculation [80]. The Figure serves as an update of the statistical combination of the ATLAS results in all $t\bar{t}$ decay channels at 7 TeV [81] taking into account updates at 8 TeV given in Ref. [82].

Top-quark polarisation

The short life-time of the top quark prevents its spin to get depolarised by the strong interaction. Thus, the *polarisation* of the top quark can be measured by studying the polar angle θ_i of the charged lepton in the parent top-quark rest frame. However, only the spin polarisation of an ensemble of top quarks can be measured rather than the spin of an individual top quark. The distribution $W(\cos\theta_i) \propto 1 + \alpha_i p \cos\theta_i$, where any daughter particle of the top is labeled with i with respect to a quantisation axis, is measured. The degree of polarisation along the quantisation axis is p and α_i is the spin analysing power [83]. The spin analysing powers vary among different daughter particles of the top quark. Charged leptons have the largest sensitivity to the spin state of the top quark ($\alpha_\ell = 1$). The top-quark polarisation is measured by performing a fit to data using the simulated signal events corresponding to both a negative and a positive polarisation combined with background templates. To determine $\cos\theta_i$ a full reconstruction of the $t\bar{t}$ event is required. The fit returns a fraction of positively polarised top quarks f which is translated into the degree of polarisation as follows:

$$\alpha_\ell p = 2f - 1. \tag{2.19}$$

The measured top polarisation $f = 0.470 \pm 0.009\ (\text{stat.})^{+0.023}_{-0.032}\ (\text{syst.})$ is compatible with the SM prediction of $f = 0.5$ [84].

W **boson polarisation**

The decay products of the top, namely the b-quark and the W boson, have a relative spin orientation which is constrained by the SM prediction that W bosons are mainly produced in a left-handed helicity state. All fermions, including the top quark, are predicted to interact via the vector-minus-axial-vector $(V - A)$ charged current coupling because their decay proceeds entirely via the weak interaction:

$$-i\frac{g}{\sqrt{2}} V_{tb} \gamma^\mu \frac{1}{2}(1 - \gamma_5). \tag{2.20}$$

The helicity is defined as the projection of the spin orientation $\widehat{\vec{\sigma}}$ onto the momentum direction of the particle:

$$H\Psi_{L,R} = \mp\Psi_{L,R} \text{ with } H = \frac{\widehat{\vec{\sigma}}\vec{p}}{|\vec{p}|}. \tag{2.21}$$

This means that if the spin orientation is opposite to the direction of motion of the W, it carries $H = -1$ and vice versa. Thus, in the limit of massless b-quarks the $V - A$ structure of the Wtb-vertex permits right-handed b-quarks in the top-quark decay. The latter one has a spin-angular momentum of $+1/2$ with respect to the decay axis and its decay products need to have opposite momenta in the top-quark rest frame. Hence, the existence of a right-handed W boson is forbidden by the conservation of angular momentum. Since the top quark decays before it can form a $t\bar{t}$-quarkonium bound

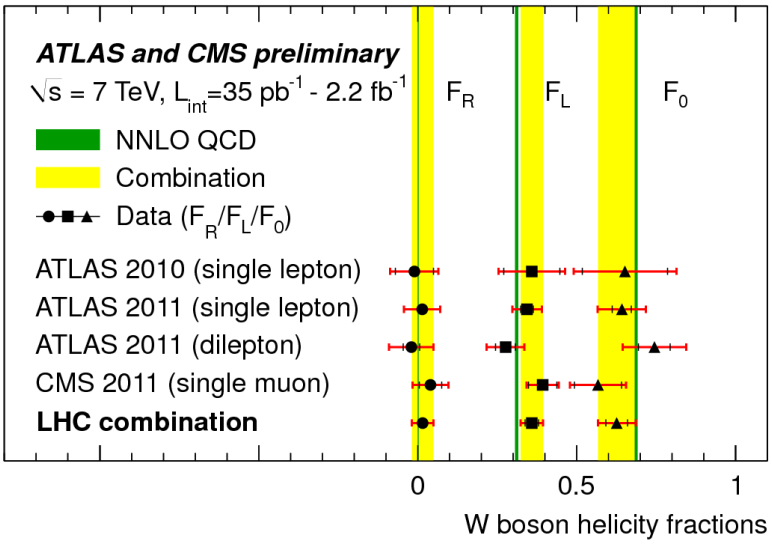

Fig. 2.16.: Overview of the four measurements included in the combination as well as the results of the combination. The inner and outer error bars correspond to the statistical and the total uncertainty, respectively. The green solid line indicates the predictions of NNLO QCD calculations [85].

state, its decay products inherit the spin information of the parent top quark. The $V-A$ structure of the Wtb coupling can be probed directly by studying the angular distribution of the decay products. The angular distribution is defined by θ^* which is the angle between the down-type fermion originating from the W and the top quark both in the W boson rest frame. Since b-quarks have non-vanishing masses, the partial decay width of the top quark can be parametrised in terms of left-handed $(\mathcal{F}_L)$, right-handed $(\mathcal{F}_R)$ and longitudinal $(\mathcal{F}_0)$ polarised W boson helicity fractions and the angular distribution θ^*:

$$W(\cos\theta^*) = \frac{3}{4}(1-\cos^2\theta^*)\mathcal{F}_0 + \frac{3}{8}(1-\cos\theta^*)^2\mathcal{F}_L + \frac{3}{8}(1+\cos\theta^*)^2\mathcal{F}_R, \text{ where} \quad (2.22)$$

$$1 = \frac{\Gamma_{\mathcal{F}_0}(t\to Wb) + \Gamma_{\mathcal{F}_L}(t\to Wb) + \Gamma_{\mathcal{F}_R}(t\to Wb)}{\Gamma(t\to Wb)} \text{ [86]} \quad (2.23)$$

is preserved. Both the ATLAS and the CMS experiment measured the W helicity fractions in $t\bar{t}$ events in dilepton and lepton plus jets final states [87–89] and combined the measurements at 7 TeV corresponding to an integrated luminosity of up to 2.2 fb^{-1} [85] as illustrated in Figure 2.16. The measured helicity fractions are

$$\mathcal{F}_0 = 0.626 \pm 0.034\ (\text{stat.}) \pm 0.048\ (\text{syst.}), \quad (2.24)$$

$$\mathcal{F}_L = 0.359 \pm 0.021\ (\text{stat.}) \pm 0.028\ (\text{syst.}), \quad (2.25)$$

$$\mathcal{F}_R = 0.015 \pm 0.034. \quad (2.26)$$

The measurements are consistent with the SM predictions at NNLO in QCD [90]. Deviations from the SM predictions could be a hint for BSM physics. Therefore, exclusion

limits are set on anomalous couplings for each discussed measurement [30]. The CDF

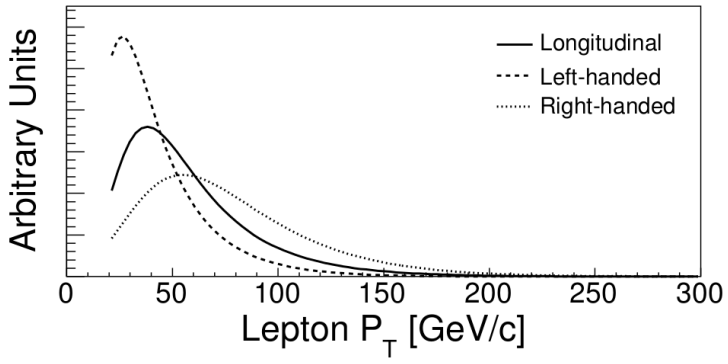

Fig. 2.17.: The charged lepton p_{T} spectrum for top quark decays to left-handed, right-handed, and longitudinally polarised W bosons [91].

experiment [91] used a different observable to determine the W boson polarisation. Because of the fact that charged leptons originating from left-handed W decays are predominantly emitted in the backward direction with respect to the W boson direction of motion in the lab frame, a softer lepton transverse momentum p_{T} distribution is the consequence, whereas the opposite is the case for charged leptons from right-handed W boson decays resulting in a harder p_{T} spectrum. The longitudinal polarisation shows a spectrum in between. Figure 2.17 depicts the p_{T} distribution for the charged lepton originating from W bosons in three different polarisation states assuming a top-quark mass of $m_t = 175$ GeV and after applying the event selection given in Ref. [91].

Top-quark spin correlations

The polarisation of the top and the anti-top quarks produced via hadronic collisions is very small in $t\bar{t}$ events. However, their spins are predicted to be correlated [92–94] and the spin information of the top quark is passed to its decay products enabling the measurement of the *spin correlation* between the top and the anti-top quark in $t\bar{t}$ events. As described in Section 2.3.1, the $t\bar{t}$ production is mainly driven by the gluon-gluon fusion process ($gg \rightarrow t\bar{t}$). In regimes where the invariant mass of the $t\bar{t}$-system is sufficiently low, the $t\bar{t}$ production is dominated by the fusion of like-helicity gluon pairs [95]. This results in common helicity states (left-left or right-right) of the top quarks. The decay products of the top and the anti-top quark possess correlations in the azimuthal angle $\Delta\phi$ (as defined in 3.2.1) between the two charged leptons in the dileptonic decay channel or between the down-type quark originating from the top quark that decays hadronically and the charged lepton of the leptonically decaying top quark in the lepton plus jets channel. Correlations are also expected to be observable for the $\cos\phi$ distributions where ϕ is defined as the angle between the direction of flight of the positively charged lepton or down-type jet in the top-quark rest frame and the direction of flight of the negatively charged lepton or down-type jet in the $\bar{t}$ rest frame [96]. As described in 2.3.1, the different production mechanisms and center-of-mass energies at the TEVATRON and the LHC result in complementary measurements of spin correlations at both colliders. Different spin correlation measurements were

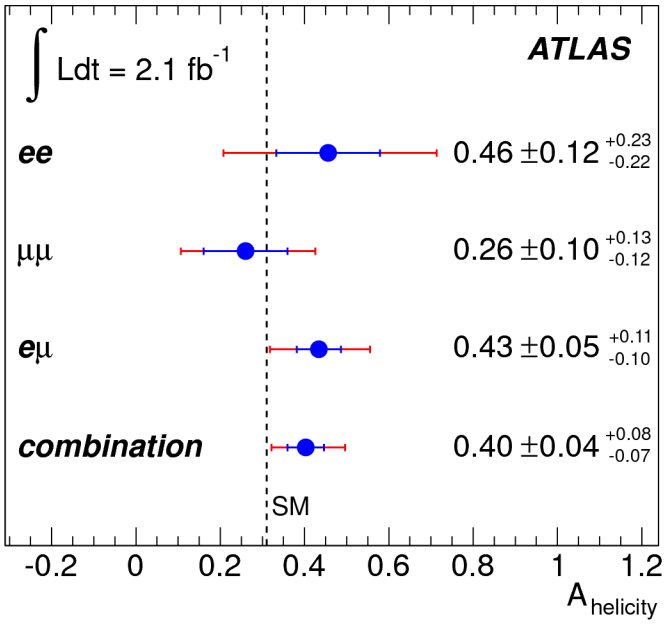

Fig. 2.18.: Value of A_{helicity} compared to the SM prediction for the *ee*, *eμ* and *eμ* channels and the combination. The results are consistent with the Standard Model prediction [97].

performed by the CDF and the DØ experiment [98–100] including the measurement of the DØ experiment claiming evidence for spin correlations in $t\bar{t}$ events according to a significance of 3.1 standard deviations [101].
The degree of correlation A is measured in order to test two different models which predict that spin correlations either exist or do not exist in nature. A is defined as the fractional difference between the number of events where the top and anti-top quark spin is aligned and those where the top and anti-top quarks spin alignments are opposite:

$$A = \frac{N(\uparrow\uparrow) + N(\downarrow\downarrow) - N(\uparrow\downarrow) - N(\downarrow\uparrow)}{N(\uparrow\uparrow) + N(\downarrow\downarrow) + N(\uparrow\downarrow) + N(\downarrow\uparrow)}. \tag{2.27}$$

The arrows are defined as the spin of the top or anti-top quarks with respect to a quantisation axis. The ATLAS collaboration observed spin correlations in $t\bar{t}$ events with a data set recorded at 7 TeV corresponding to an integrated luminosity of 2.2 fb^{-1} performing a fit to simulated event samples in the $\Delta\phi$ distribution extracting the correlation degree A from the fit result. By choosing the helicity basis that is defined as the direction of flight of the top quark with respect to the center-of-mass frame of the $t\bar{t}$-system as quantisation axis the degree of spin correlation is $A_{\text{helicity}} = 0.40^{+0.09}_{-0.08}$. This result is consistent with the NLO prediction of the SM and is illustrated in Figure 2.18 for the three tested channels *ee*, *eμ* and *eμ*. The hypothesis of a model with no spin correlations is excluded with 5.1 standard deviations [97].

2.4. Higgs boson physics

The Higgs boson is the last missing piece of the SM to explain the mechanism of electroweak symmetry breaking. Since the 4$^{\text{th}}$ July 2012, the day of the announcement of the discovery of a new boson at the LHC, there is a constant strive to uncover the nature of this new boson. To answer that question a wide variety of dedicated analyses are being performed. All decay modes of the Higgs boson are under study to measure their rate and compare it with the SM prediction. Furthermore, the underlying production

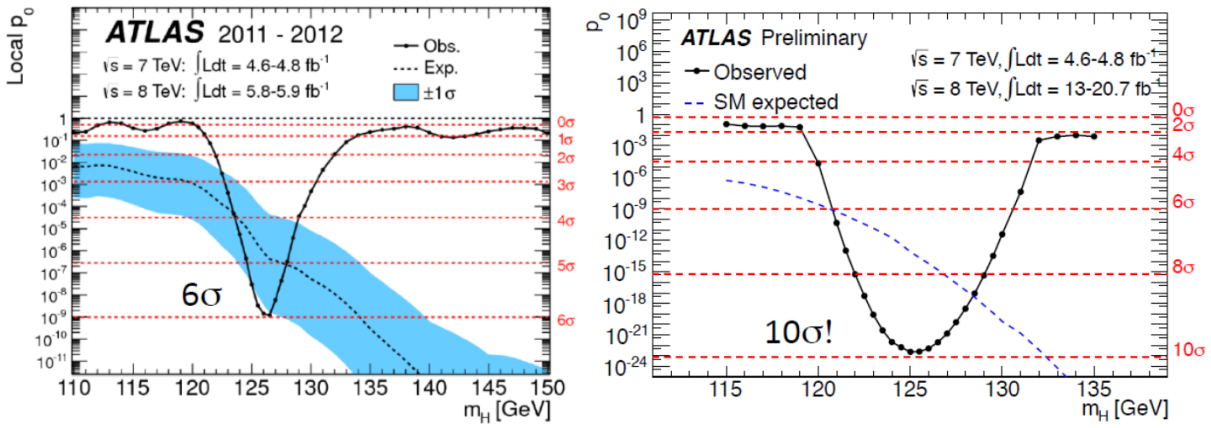

(a) *(b)*

Fig. 2.19.: The local p_0-value testing the hypothesis of a SM Higgs boson with respect to different Higgs boson masses [102].

mechanism as well as the fundamental properties of the new boson such as the mass (see Section 1), spin, parity or its couplings are being investigated. However, evidence that the discovered new boson is the Higgs boson predicted by the SM is already quite compelling [103–127]. The resulting rates and distributions are compatible with a scalar coupling of the Higgs boson to other SM particles with a strength that is proportional to their masses. Figure 2.19 exemplifies the gain in the observed significance for a Higgs boson mass at around $m_H = 125$ GeV from the 4$^{\text{th}}$ July 2012 to July 2013. An observed significance for a Higgs boson at around $m_H = 126$ GeV of $\sim 6\sigma$ corresponding to the public results provided by the ATLAS experiment in July 2012 [1] is shown in Figure 2.19a, whereas Figure 2.19b depicts the same for results published before July 2013 [103]. The observed significance for the existence of a Higgs boson increased by $\sim 4\sigma$ within one year. The $\sim 10\sigma$ excess corresponds to a p_0-value at $m_H = 125$ GeV implying the probability that the data under the assumption of the correctness of the null hypothesis (SM without a Higgs boson) corresponds to $\sim 10^{-22}$. Hence, it is extremely likely that the data can not be described by a SM without a Higgs boson although small p-values should be treated with caution since the systematic biases and uncertainties in the model of the null hypothesis are known with finite precision. The signal strength μ or best fit $\sigma/\sigma_{\text{SM H}}$ plots provide an overview of the consistency of the Higgs boson with the SM prediction of a complex-scalar Higgs boson. As described in Section 2.4.2, the Higgs decays in several channels. The plots in Figure 2.20 depict decay channels of the

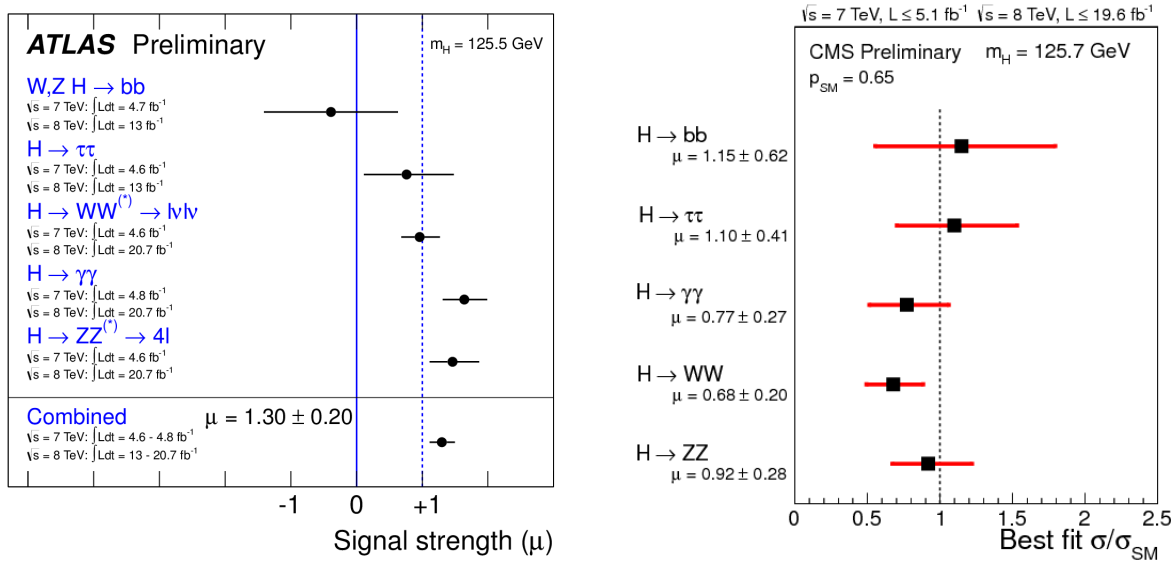

(a) *(b)*

Fig. 2.20.: Measurements of the signal strength parameter μ and $\sigma/\sigma_{\mathrm{SM}}$ for the individual channels and their combination. The left (right) plot represents the measurement of the ATLAS experiment (CMS experiment) for a Higgs mass of $m_H = 125.5$ GeV ($m_H = 125.7$ GeV) [128, 129].

Higgs boson observed so far and illustrate the corresponding measured cross-section normalised to the cross-section that is expected for a SM Higgs boson. A signal strength of unity means that the observed cross-section in a specific decay mode coincides with the SM Higgs boson. No signal is present in a decay mode if $\mu = \sigma/\sigma_{\mathrm{SMH}} = 0$. The black dots represent the measured values and the horizontal lines show the error bars for the measurement. Numerous analyses are being performed using the most recent data from the first LHC run and more results are published almost on a monthly basis successively providing elicitation of the nature of the Higgs boson. The $H \to \tau^+\tau^-$ channel for example got gradually more consistent with unity by expanding the analysis to the 8 TeV data of the 2012 run. This channel is of particular interest since no fermionic coupling of the Higgs boson has been observed yet. The latest results of the ATLAS experiment show a combined signal strength of $\mu = 1.30 \pm 0.20$ (see Figure 2.20) including up to 4.8 fb^{-1} of data at $\sqrt{s} = 7$ TeV and up to 20.7 fb^{-1} at $\sqrt{s} = 8$ TeV for the $H \to WW^* \to \ell\nu\ell\nu$ channel. In channels where ATLAS and CMS have reached sensitivity, the measurements are consistent with the SM predictions for a Higgs boson so far. However, undiscovered particles that could for example be produced loop-induced (see Section 2.4.1) would affect the decay channels that are predicted for the Higgs boson by the SM. As a result, more signal events than expected from the SM could be observed or, if additional Higgs bosons exist (as predicted by supersymmetric models such as the MSSM), less signal strength could be observed in some channels.

In the SM, the profile of the Higgs boson is determined uniquely once its mass M_H is fixed. Physical observables such as the decay width, the branching ratios and the

production cross-section are dependent on the strength of the Higgs Yukawa coupling to fermions and gauge bosons (see Section 2.1.2).

2.4.1. Higgs boson production

The production mechanisms for a SM Higgs boson at the LHC are illustrated in Figure 2.21. The coupling of a Higgs boson to another particle is proportional to its mass, thus it couples more likely to particles that have high masses such as the top quark or the electroweak bosons. The dominating production mechanism is the gluon-gluon fusion

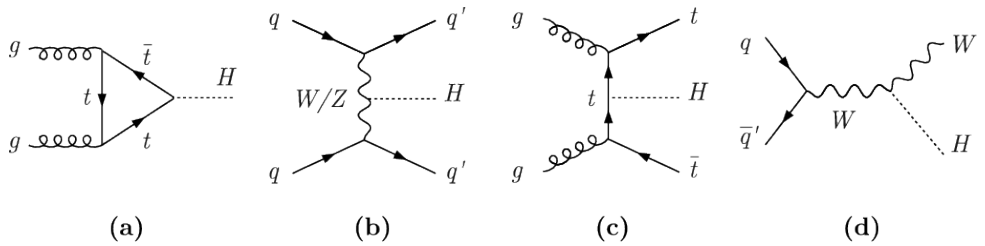

Fig. 2.21.: The four dominating production mechanisms for a SM Higgs boson at the LHC.

(see Figure 2.21a) for all possible Higgs masses (see Figure 2.22). The gluon-gluon fusion production mechanism is known to NNLO in theoretical calculations with a theoretical uncertainty of $\mathcal{O}(15\%)$ [130]. The SM Higgs is produced by the fusion of a top-quark loop initiated by two gluons. Another important production mechanism is the vector boson fusion (VBF) channel which is known to NLO with a theoretical uncertainty of $\mathcal{O}(5\%)$ [130]. In this process two vector bosons, mediated by two initial quarks, fuse to a SM Higgs boson (see Figure 2.21b). Compared to the gluon-gluon

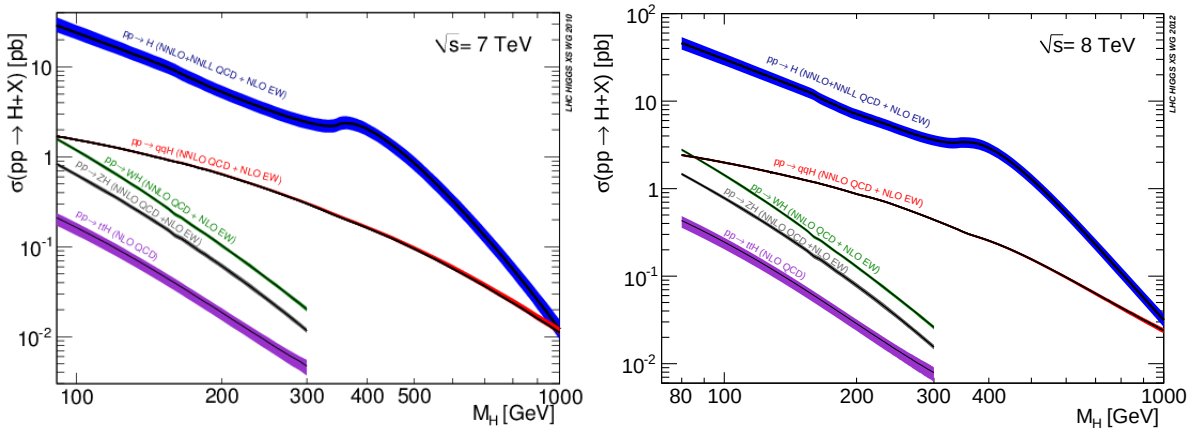

Fig. 2.22.: The production cross-section for the SM Higgs boson at 7 TeV (left) and 8 TeV (right) at the LHC [130].

fusion production, the VBF creates additional particles. A characteristic signature in the detector for VBF are two jets in the forward region and a gap in the rapidity distribution.

The two associated processes (VH and $t\bar{t}H$) shown in Figure 2.21c and 2.21d are less likely for the production of a SM Higgs (see Figure 2.22). However, the associated channels preserve the possibility to search for the Higgs boson in decay channels that are embedded in a large QCD multijet background such as $H \to b\bar{b}$. Moreover, the searches in the associated production processes are sensitive to the Yukawa coupling between the Higgs boson and the vector bosons (VH) or the top quark ($t\bar{t}H$). The arrangement of the production mechanisms shown in Figure 2.22 remains by increasing the center-of-mass energy but the cross-section for each individual process increases.

2.4.2. Higgs boson decay

Due to the fact that the SM Higgs boson cannot be detected directly because of its small lifetime, the different decay channels of the SM Higgs need to be investigated (see Figure 2.23). The Higgs boson partial decay width into a pair of fermions at tree-level is given by

$$\Gamma(H \to f\bar{f}) = \frac{N_c G_F}{4\pi\sqrt{2}} m_f^2 m_H \beta_f^3, \tag{2.28}$$

where the colour factor $N_c = 1(3)$ for leptons (quarks) and $\beta = \sqrt{1 - 4m_f^2/m_H^2}$ is a phase-space factor that accounts for the velocity of the fermion in the center-of-mass system. The $\mathcal{BR}$s take higher-order QCD and electroweak corrections into account [131]. The Higgs boson decay into a pair of weak gauge bosons is described by

$$\Gamma(H \to VV) = \delta_V \frac{G_F}{16\sqrt{2}\pi} m_H^3 (1 - 4x + 12x^2)\beta_V, \tag{2.29}$$

with $x = m_V^2/m_H^2$ and $\delta_V = 1(2)$ for $V = Z$ ($V = W$). β_V describes a phase-space factor. The Higgs decay into a pair of gluons or photons occurs mainly via heavy quark loops such as top or bottom quark loops. In the case of the decay into photons also W boson loops arise. For $m_H \ll m_t$, the partial decay width is given by

$$\Gamma(H \to gg) = \frac{G_F \alpha_s^2(m_H^2)}{36\sqrt{2}\pi^3} m_H^3 \left(1 + \left(\frac{95}{4} - \frac{7N_f}{6}\right)\frac{\alpha_s}{\pi}\right) \text{ for gluons and} \tag{2.30}$$

$$\Gamma(H \to \gamma\gamma) = \frac{G_F \alpha_s^2}{128\sqrt{2}\pi^3} m_H^3 \left|\frac{4}{3} N_c e_t^2 - 7\right|^2 \text{ for photons ,} \tag{2.31}$$

respectively [132]. For Higgs masses below 130 GeV the dominant decay products of the Higgs are $b\bar{b}$ pairs. Table 2.3 shows the SM Higgs $\mathcal{BR}$s in fermionic and bosonic final states assuming $m_H = 125$ GeV [130]. The large QCD background is what makes this decay mode so challenging. Other decay channels in this region are the decay in $\gamma\gamma$ which has a small branching ratio but a very clean signature and $\tau^+\tau^-$ where the VBF can be used for background suppression. In higher SM Higgs mass regions the decay in vector bosons is dominant and hence WW and ZZ are sensitive channels. Also the decay in a top-quark pair is likely at SM Higgs masses larger than ~ 360 GeV. It

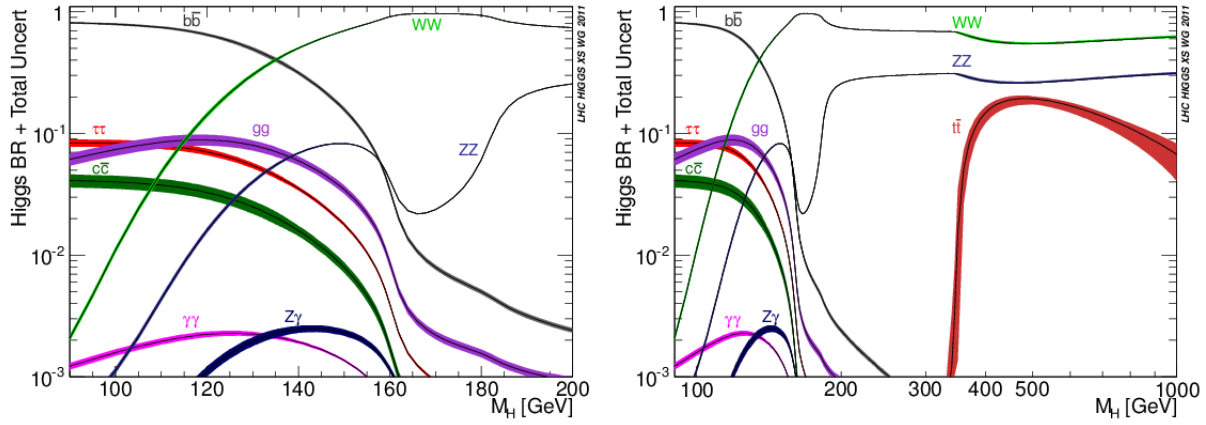

(a) *(b)*

Fig. 2.23.: The branching ratios for the decay of the SM Higgs boson [130].

$H \to b\bar{b}$	$H \to \tau^+\tau^-$	$H \to \mu\mu$	$H \to s\bar{s}$	$H \to c\bar{c}$	$H \to t\bar{t}$
$5.78 \cdot 10^{-1}$	$6.37 \cdot 10^{-2}$	$2.21 \cdot 10^{-4}$	$4.40 \cdot 10^{-4}$	$2.68 \cdot 10^{-2}$	0.00
$H \to gg$	$H \to \gamma\gamma$	$H \to Z\gamma$	$H \to WW$	$H \to ZZ$	Total Γ_H [GeV]
$8.56 \cdot 10^{-2}$	$2.30 \cdot 10^{-3}$	$1.55 \cdot 10^{-3}$	$2.16 \cdot 10^{-1}$	$2.67 \cdot 10^{-2}$	$4.03 \cdot 10^{-3}$

Tab. 2.3.: SM Higgs ($m_H = 125$ GeV) $\mathcal{BR}s$ in fermionic and bosonic final states including the total Higgs width Γ_H [130].

becomes obvious that the predicted branching fractions change a lot with respect to different Higgs masses. Thus, dedicated strategies are needed to identify the Higgs depending on its mass. The ATLAS collaboration has excluded a SM Higgs boson at mass ranges (m_H) between 111-122 GeV and 131-559 GeV at 95% confidence level (C.L.) based on 5 fb^{-1} data at 7 TeV and 6 fb^{-1} at 8 TeV [1]. The corresponding m_H exclusion region of CMS is between 110-121.5 GeV [2] and 127-710 GeV [133] at 95% CL.

2.5. $t\bar{t}H$ phenomenology

The Higgs boson can be produced in association with top-quark pairs ($t\bar{t}H$) as discussed in Section 2.4.1. In Figure 2.24, a subset of Feynman diagrams for the $t\bar{t}H$ signal process is presented. The $t\bar{t}H$ production is driven by two parton processes $q\bar{q} \to t\bar{t}H$ and $gg \to t\bar{t}H$. Following the approach in Section 2.3.1, the average x that needs to be carried by the colliding partons to create a $t\bar{t}H$ event at rest needs to be

$$x \sim 2m_t + m_H/\sqrt{s}, \tag{2.32}$$

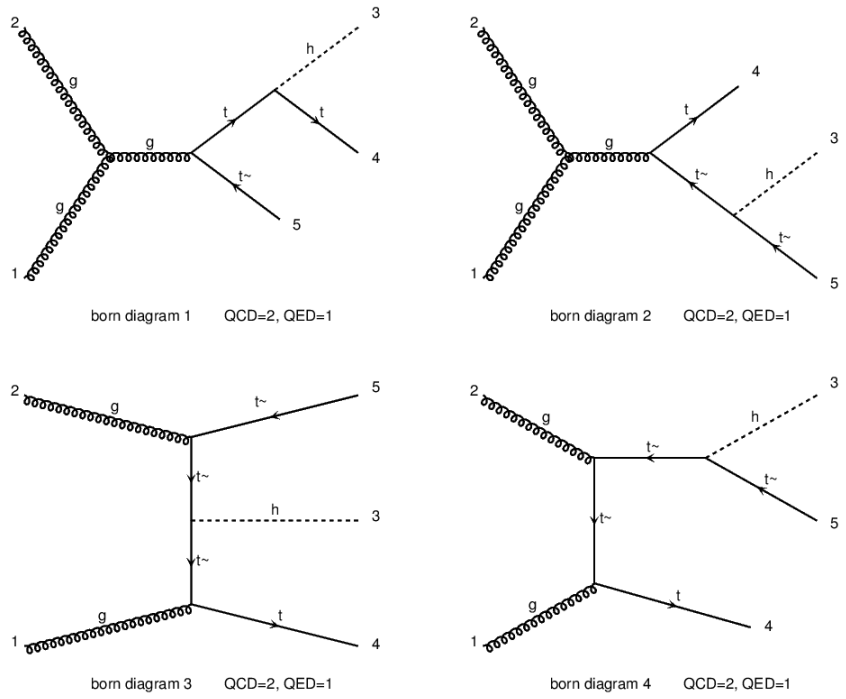

Fig. 2.24.: A subset of gluon initiated born level Feynman diagrams of the $t\bar{t}H$ signal produced with the Monte Carlo event generator aMC@NLO [134–136]. The NLO calculation includes nine subprocesses with a total number of 448 independent Feynman diagrams.

resulting in $x \approx 0.06$ for $\sqrt{s} = 8$ TeV, $m_H = 125$ GeV and $m_t = 172.5$ GeV. Thus, the $t\bar{t}H$ production via gg fusion and $q\bar{q}$ annihilation is about the same for 8 TeV (see Figure F.1 in Appendix F.1) at the LHC. This picture changes when increasing the center-of-mass energy to $\sqrt{s} = 14$ TeV, resulting in $x \approx 0.03$. In that scenario the gg fusion process dominates the $q\bar{q}$ annihilation process as depicted in Figure 2.10b in Section 2.2.3. The Higgs couples to the top quark either via Higgs strahlung or via top quark fusion [11–13]. The decay of the $t\bar{t}H$ process corresponds to the decay of the $t\bar{t}$ pairs described in Section 2.3.2 plus the decay of the Higgs boson in low-mass regions namely $H \to b\bar{b}, W^+W^-, gg, \tau^+\tau^-, ZZ, c\bar{c}, Z\gamma$ and $\gamma\gamma$ as described in Section 2.4.2. For low-mass regions that are favoured for a SM Higgs boson the dominant decay mode is $H \to b\bar{b}$. The final state of this channel consists of two W bosons and four b-jets. Two of the latter are originating from the Higgs and two from each top quark. The decay channel of the $t\bar{t}H$ process depends on the decay of the two W's. The semileptonic or "lepton plus jets" channel is illustrated in Figure 2.25. The dominant background contributions originate from the production of $t\bar{t}$ pairs with extra light, c- or b-jets, $\gamma\gamma$, Z, W^-W^+ depending on the final-state Higgs boson decay. Both the Higgs production through the gg fusion process and the decay of the Higgs into two photons provides the possibility of an indirect measurement of the Yukawa coupling between the Higgs and the top quark because both processes are dependent on a top-quark loop. However, the information which is gained by the top quark to Higgs boson Yukawa coupling in these scenarios is based on the assumption that no new massive BSM particles are

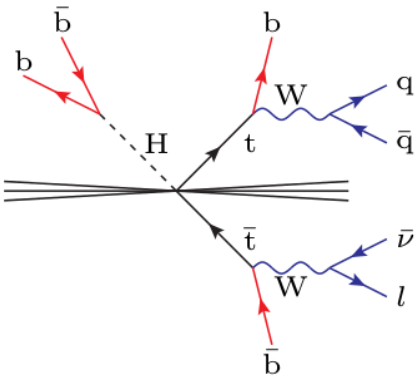

Fig. 2.25.: The lepton plus jets decay channel of the $t\bar{t}H$ process.

contributing in the top-quark loop. As described in Section 2.4.2, the Higgs boson is likely to exist in a mass region where the direct Higgs decay into two top quarks is disfavored. Hence, the Higgs production in association with a $t\bar{t}$ pair is the only way to probe the $t\bar{t}H$ vertex in a model independent manner [10, 137, 138].

CHAPTER

THREE

THE EXPERIMENTAL SETUP

This chapter gives a short summary of the LHC and a brief description of the main components of the ATLAS detector.

3.1. The Large Hadron Collider and its experiments

The Large Hadron Collider (LHC) [139, 140] at CERN located at the Swiss-French border near Geneva is the most powerful particle accelerator in the world. The tunnel in which the LHC is installed has a circumference of roughly 27 kilometers and lies ~ 100 meters underground. After a planning and construction phase of around twenty years, the LHC began its operations in the Fall 2009. The accelerator has two separated beam lines in which two proton beams (or lead ion beams) are accelerated in opposite directions. The center-of-mass energy was initially at $\sqrt{s} = 7$ TeV and was increased in the 2012 run to $\sqrt{s} = 8$ TeV. The LHC is designed for a center-of-mass energy of $\sqrt{s} = 14$ TeV and a luminosity of 10^{-34} cm^{-2}s^{-1}. The instantaneous luminosity is defined as

$$L = f N_B \frac{N_1 N_2}{4\pi\sigma_x\sigma_y}; \tag{3.1}$$

where N_B is the total number of injected bunches and $N_1(N_2)$ is the number of particles per bunch $1(2)$. The revolution frequency is labeled as f and σ_i is the so-called emittance that describes the beam spread in the horizontal and the vertical plane to the beam direction assuming Gaussian beam shapes. To investigate physical processes having a specific cross-section σ high event rates are essential. The number of expected events is described by the following equation

$$N = \sigma \int L \, \mathrm{dt} = \sigma\mathcal{L}, \tag{3.2}$$

where σ is the cross-section of a given process and $\mathcal{L}$ is the time integral of the instantaneous luminosity L. The beam is separated into 2808 proton bunches each containing

$1.15 \cdot 10^{11}$ protons per beam injection. Thus, every 25 ns a proton beam passes an experiment where the beams are collided. The protons are preaccelerated in a linear collider (LINAC2) to an energy of 50 MeV. Afterwards the BOOSTER accelerates the protons to an energy of 1.4 GeV. The protons are further accelerated in the Proton Synchrotron (PS) up to an energy of 25 GeV before being injected in the Super Proton Synchrotron (SPS) where they gain the LHC injection energy of 450 GeV. The proton bunches get injected into the two beam pipes and get accelerated to the final center-of-mass energy. The accelerator chain is illustrated in Figure 3.1. After around 20 minutes of acceleration

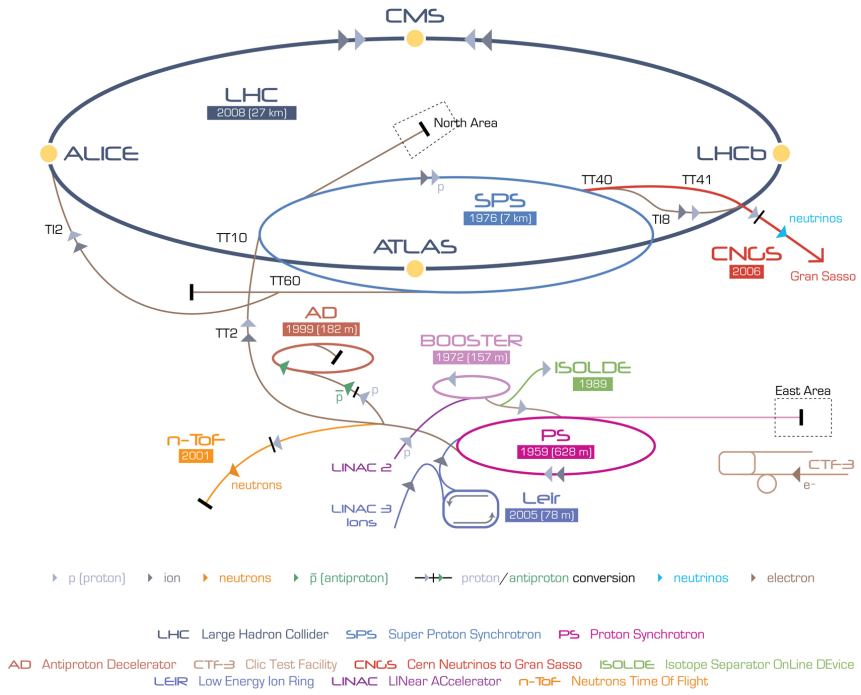

Fig. 3.1.: The accelerator chain including the four experiments that are located at the LHC.

and beam optimisation the proton bunches are brought to collision in the center of four experiments that are placed at the LHC accelerator ring, two of which are so-called multi purpose detectors – ATLAS (**A** **T**oroidal **LHC** **A**pparatu**S**) and CMS (**C**ompact **M**uon **S**olenoid experiment). Their physics programs include precise measurements of the SM, the search for the Higgs boson and physics phenomena beyond the SM. The two other experiments try to answer questions of nature in a less wide range. The LHCb experiment, which has the only asymmetric detector [141], focuses on CP violation in hadrons containing b-quarks. The ALICE (**A** **L**arge **I**on **C**ollider **E**xperiment) detector [142] investigates the quark-gluon plasma using lead ion (Pb^{82+}) collisions.

3.1.1. The LHC performance

The LHC is mainly operating since 2010 after the actual start was delayed by more than one year due to an incident that was caused by a failure in an electrical connection. In late November of 2009, the first data at $\sqrt{s} = 900$ GeV were recorded. In March 2010, the data taking period started with an increased center-of-mass energy of $\sqrt{s} = 7$ TeV.

At that point the LHC overtook the TEVATRON as the particle accelerator that provides the highest center-of-mass energy. Between March 2010 (2011) and the winter shutdown, the delivered integrated luminosity was 48 pb^{-1} (5.32 fb^{-1}). In March 2012, the center-of-mass energy was increased to $\sqrt{s} = 8$ TeV and an integrated luminosity of 23.26 fb^{-1} was recorded with a data taking efficiency (data used in physics analysis) of 95% (90%) [143]. Figure 3.2a depicts the delivered luminosity of the ATLAS experiment that

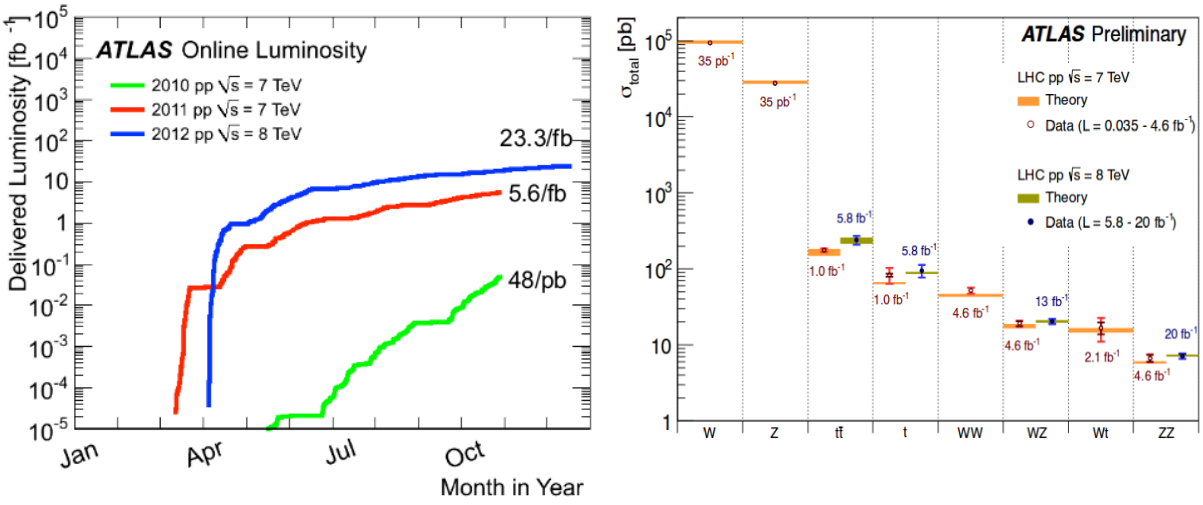

(a) *(b)*

Fig. 3.2.: The delivered luminosity of the ATLAS experiment with respect to the month in the years of 2010 to 2012 is shown on the left. On the right, the total cross-sections with respect to different SM processes is depicted [143].

was recorded in the first run of the LHC with respect to each year. The total cross-section for different SM processes is illustrated in Figure 3.2b and corresponds to the recorded data during the 7 TeV and 8 TeV run and it includes the number of events that were produced for a specific process such as $t\bar{t}$ or Z. The precision SM measurements are very important in terms of the understanding of the detector. Moreover, their understanding is essential to discover new physics.

3.2. The ATLAS detector

The ATLAS detector [144, 145] is a multipurpose detector with a cylindrical geometry which is forward-backward symmetric [146]. It was build to cover a large physics program with pp- and heavy ion collisions that appear at the highest energies and instantaneous luminosities, resulting in extremely high rates. With its length of 44 m and its diameter of 25 m, it is the largest detector at the LHC. It has a weight of $\sim$ 7000 t. Figure 3.3 shows the ATLAS experiment with its solenoid and toroid magnets and the different sub detector systems that are arranged in an onion-shell-like structure. The main detector systems – the inner detector, the calorimeters, the muon spectrometer and the magnet system – are briefly explained in Section 3.2.2.

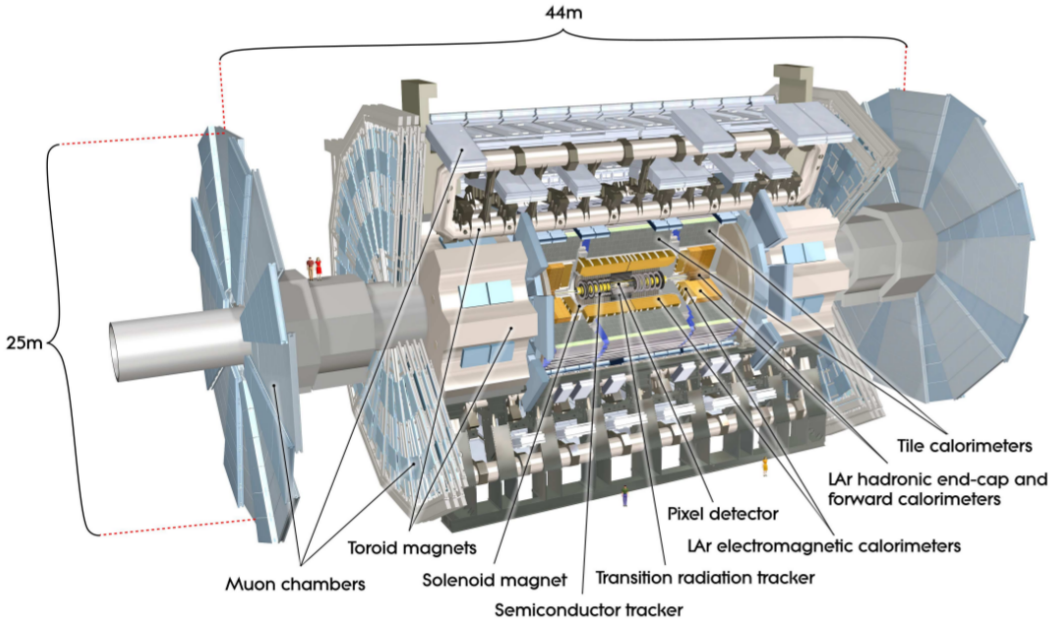

Fig. 3.3.: The profile of the ATLAS detector.

The design of the detector systems was adjusted to some challenges the ATLAS detector is confronted with. The high collision rates result in the need of radiation-hard electronics, fast read-out systems including efficient trigger and data acquisition systems (DAQ). The large event rates and pile-up events require a high-resolution particle identification and reconstruction system to overcome the significant QCD background contributions to enable searches and precise measurements.

3.2.1. Coordinate system and kinematic variables

The coordinate system of the detector has its origin in the interaction point and is right-handed. The axis along the beam line is the z-axis, the x-axis points to the middle of the LHC ring and the y-axis is aligned in the direction upward to a point on the surface that is located about half a kilometer to the CERN cafeteria. The cylindrical coordinates (r, ϕ) are aligned in the transverse plane. The azimuthal angle ϕ is the angle around the beam pipe with $\tan\phi = y/x$. The pseudorapidity η is defined as $\eta = -\ln[\tan\theta/2]$, where θ is the polar angle. Distances between two objects are described by $\Delta R = \sqrt{(\Delta\eta)^2 + (\Delta\phi)^2}$. Differences in the pseudorapidity $\Delta\eta$ are invariant under Lorentz transformations. The transverse momentum of a particle is defined as $p_{\mathrm{T}} = \sqrt{p_x^2 + p_y^2}$. The transverse energy $E_T = E\sin\theta$ and the missing transverse energy $\not{E}_{\mathrm{T}} = \sqrt{(E_x^{\mathrm{miss}})^2 + (E_y^{\mathrm{miss}})^2}$ are defined in the plane perpendicular to the beam axis. The transverse momentum and the transverse energy are identical within the relativistic limit. $\not{E}_{\mathrm{T}}$ is the magnitude of the negative vector sum of the momenta of all particles present in an event.

3.2.2. An overview of the sub detector systems

The different sub detector systems are arranged within different layers as sketched in Figure 3.4 and detect interactions of different particle types. The inner tracking detector (ID) [147–149] consists of a silicon pixel detector, a silicon micro strip detector and a transition radiation tracker. It covers the region $|\eta| < 2.5$ and measures the charge and the momentum of the interacting particles. Charged particles are traced via the creation of electron-hole pairs in semiconductors or by ionising gas. The next layer is a thin superconducting solenoid magnet [150–152] with an axial magnetic field (2 T). It enables the measurement of charged particle momenta in the ID by ascertaining the curvature of the tracks. Both former layers are surrounded by a high-granularity lead/liquid Argon (LAr) sampling calorimeter [153,154] – the electromagnetic calorimeter (ECAL). It measures the energy and the position of electromagnetic showers with a pseudorapdity coverage of $|\eta| < 3.2$. Due to the fact that the ECAL is massive, photons and electrons

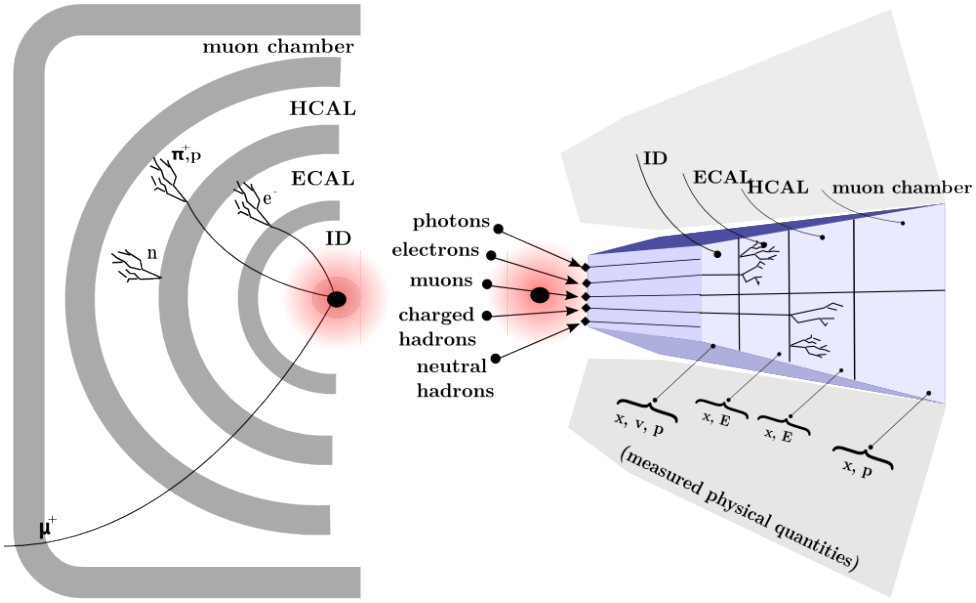

Fig. 3.4.: The profile of a detector and its layers fulfilling different tasks in particle reconstruction.

form electromagnetic showers by interacting with the detector material via alternating pair creation and Bremsstrahlung effects. LAr sampling calorimeters are also used to measure hadronic showers in the end-cap ($1.5 < |\eta| < 3.2$) and the forward ($3.1 < |\eta| < 4.9$) regions. An iron/scintillator tile calorimeter (as a next layer) measures hadronic showers in the central region ($|\eta| < 1.7$) – the hadronic calorimeter (HCAL). Hadronic showers are the result of various interactions of the hadrons with the detector material. Whereas electromagnetic showers are typically contained in the ECAL, hadron showers range into the HCAL. The energy resolution of the calorimeters follows poisson statistics and is parametrised by a convolution of three different terms:

$$\frac{\sigma_E}{E} = \frac{a}{\sqrt{E}} \oplus \frac{b}{E} \oplus c. \tag{3.3}$$

The first term covers basic phenomena in the shower evolution. Since those processes follow statistical fluctuations, the intrinsic limiting accuracy improves with increasing energy. The second component describes further effects that are due to instrumental effects such as noise. Its relative contribution to the energy resolution decreases by increasing the energy. This term limits the low-energy performance of the detector. The last contribution c accounts for calibration errors, non-uniformities such as dead material in the detector and limits the detector performance at high energies. The number of particles that are produced in the shower is proportional to the energy of the incoming particles. Thus, the energy resolution increases if the number of particles entering the detector increases. The muon spectrometer (MS) [155] surrounds the calorimeters and consists of three large superconducting air-core toroids [150, 156, 157], each with eight coils, a system of precision tracking chambers ($|\eta| < 2.7$) and fast tracking chambers for triggering. Since muons are generally produced as minimal ionising particles (MIPs),

Detector components	Required resolution	η coverage Measurement	Trigger
Tracking	$\sigma_{p_T}/p_T = 0.05\%\ p_T \oplus 1\%$	± 2.5	
ECAL	$\sigma_E/E = 10\%/\sqrt{E} \oplus 0.7\%$	± 3.2	± 2.5
HCAL:			
– barrel/end-cap	$\sigma_E/E = 50\%/\sqrt{E} \oplus 3\%$	± 3.2	± 3.2
– forward	$\sigma_E/E = 100\%/\sqrt{E} \oplus 10\%$	$3.1 < \|\eta\| < 4.9$	$3.1 < \|\eta\| < 4.9$
MS	$\sigma_{p_T}/p_T = 10\%$ at $p_T = 1$ TeV	± 2.7	± 2.4

Tab. 3.1.: General performance goals of the ATLAS detector. E and p_T are in GeV [144].

they are the only electrically charged particles that can pass the calorimeters and reach the MS. The large toroid magnets induce a field which results in a curvature of the measured muon tracks. Hence, the momentum and the position of the produced muons is measured. Due to the fact that the momentum resolution σ_{p_T}/p_T is proportional to the momentum of the particles, the resolution increases for particles with increasing momentum. The momentum resolution suffers from degradation if multiple scattering processes occur and improves when the applied magnet field is high. The performance goals with regard to the energy and momentum resolution for the individual detector components as well as the η coverage of its respective components is depicted in Table 3.1. Due to the very high instantaneous luminosity and bunch crossing rates of up to 40 MHz it is impossible to process, record, and store every single event. Thus, a three-level trigger system [158] is installed reducing the enormous amount of data to 200 Hz and selecting events which will be recorded for analysing the data offline. Mainly soft QCD events, so-called *minimum-bias* events, are rejected and only those data are stored that are of particular interest for performance studies, SM measurements and BSM searches.

CHAPTER

FOUR

THE $T\bar{T}H$ ANALYSES

This chapter summarises the most recent $t\bar{t}H$ analyses. The ATLAS $t\bar{t}H$ analysis performed with the data set recorded at 7 TeV in 2011 is outlined and the analysis strategy for the full 2011/12 data set is briefly introduced. In addition, an overview of the dominant systematic uncertainties taken into consideration for the ATLAS $t\bar{t}H$ analysis at 7 TeV is given.

4.1. Overview

The $t\bar{t}H$ analysis is one of the most challenging analyses performed at the LHC. The simultaneous production of three heavy particles requires a large center-of-mass energy for the initial partons and is strongly suppressed by the PDFs as described in Section 2.5. Current analyses focus on the dominant decay mode $H \to b\bar{b}$ and thus on a $W^+W^-b\bar{b}b\bar{b}$ final state. Other Higgs decays, such as $H \to W^+W^-$, $H \to \tau^+\tau^-$ and $H \to \gamma\gamma$, have a much lower production cross-section for a Higgs mass of around $m_H = 125$ GeV (see Section 2.4.2). Hence, for the latter decay channels, higher integrated luminosities are needed to gain sensitivity. Table 4.1 lists the most recent results for the Higgs production in association with a top-quark pair including three different Higgs decay channels, namely $H \to b\bar{b}, \tau^+\tau^-$, and $\gamma\gamma$. This chapter focuses on the ATLAS $t\bar{t}H(H \to b\bar{b})$ analyses. The final state $W^+W^-b\bar{b}b\bar{b}$ is affected by two different challenging background processes. These are $t\bar{t}$ + light or heavy flavour jets yielding enormous rates as well as the combinatorical background that coincides with the difficulty of identifying the two b-jets that originate from the Higgs boson out of the four b-jets in an event. In addition, the complexity of the final state impedes the kinematic reconstruction of the process.

4.1.1. The $t\bar{t}H$ analyses of the ATLAS experiment at 7 TeV

The first ATLAS $t\bar{t}H$ analysis was based on the full 2011 data set of 4.7 fb^{-1} and was focused on the Higgs decay mode $H \to b\bar{b}$, investigating the ℓ+jets decay channel of

experiment	$H \to$	$t\bar{t} \to$	$\sqrt{s}$ [TeV]	$\mathcal{L}$ [fb^{-1}]	obs. (exp.) $\sigma/\sigma_{\mathrm{SM}}$
CDF [159]	$b\bar{b}$	ℓ+jets	1.96	9.5	20.5 (12.6)
ATLAS [160]	$b\bar{b}$	ℓ+jets	7	4.7	13.1 (10.5)
ATLAS [111]	$\gamma\gamma$	ℓ+jets/ dilep./ allhad.	8	20.3	5.3 (6.4)
CMS [122]	$\gamma\gamma$	ℓ+jets/ dilep./ allhad.	8	19.6	5.4 (5.3)
CMS [161]	$b\bar{b}$	ℓ+jets/ dilep.	7 (8)	5.0 (5.1)	5.8 (5.2)
CMS [162]	$b\bar{b}/\tau^+\tau^-$	ℓ+jets/ dilep.	8	19.5	5.2 (4.1)
CMS (comb.) [162]	$b\bar{b}/\tau^+\tau^-$	ℓ+jets/ dilep.	7 (8)	5.0 (5.1/19.5)	3.4 (2.7)

Tab. 4.1.: Overview of the most recent $t\bar{t}H$ results for different decay channels including information on the decay channels of the Higgs boson and the $t\bar{t}$-system, center-of-mass energy, the corresponding integrated luminosity and the expected/observed limits on the production cross-section in terms of the SM prediction σ_{SM} at 95% C.L. A Higgs mass hypothesis of $m_H = 125$ GeV is tested in all analyses except for the ATLAS $t\bar{t}H(H \to \gamma\gamma)$ where $m_H = 126.8$ GeV is tested. The lepton decay channels of the $t\bar{t}$-system includes only electrons or muons.

the $t\bar{t}$-system (see Table 4.1). Thus, the typical final state signature is characterised by one isolated high-p_{T} electron or muon, high transverse missing energy $\not{E}_{\mathrm{T}}$ and at least six jets of which four b-jets originate from the Higgs and the top decays and two light jets originating from the hadronic decay of the W boson (see also Section 2.5). The large number of b-jets is of importance when distinguishing signal from background events. The main background contribution originates from $t\bar{t}$ events that were produced in association with at least two more jets – $t\bar{t}$ + jets. The additional jets originate either from light flavour (LF) or heavy flavour (HF) quarks. The $t\bar{t}\,b\bar{b}$ background contribution remains irreducible. The applied b-tagging algorithm limits the reconstruction of the reducible $t\bar{t}$ + jets background. This is due to the fact that it depends on the b-jet identification efficiency and misidentification rate for light jets.
Events that have the $t\bar{t}H$ final state signature in the ℓ+jets channel are selected and are categorised into 13 different event topologies that depend on their jet and b-tagged jet multiplicities (see Table 4.2). Four of them are defined as signal enriched regions (SR), five as background dominated regions (BR) and four as control regions (CR). The SR and BR topologies are used in the search and are analyzed separately.
Afterwards, they are combined in a profile likelihood fit. Nuisance parameters that describe the systematic uncertainties of the analysis are introduced and as a result the overall sensitivity is maximised. The limit on the $t\bar{t}H$ production cross-section is extracted from the fit. The SR consists of 5 jets where 3 or $\geq$ 4 jets are b-tagged

and ≥ 6 jets where 3 or ≥ 4 jets are b-tagged. These topologies have a larger signal-to-background ratio and thus a larger sensitivity to the signal. The signal topologies ($\geq$ 6 jets of which 3 or $\geq$ 4 jets are b-tagged) are reconstructed using a maximum likelihood method to assign four of the six jets to the top-quark pair. This is done by adjusting the energies of the jets to reconstruct the correct masses of the top quarks and W bosons. The invariant mass of the two remaining jets that are not assigned to the two top quarks is calculated and ensures the possibility of searching for a Higgs mass resonance in the $m_{b\bar{b}}$ spectrum. The remaining five topologies (4 jets of which 0, 1, and ≤ 2 are b-tagged, 5 jets of which 2 are b-tagged and ≤ 6 jets of which 2 are b-tagged) are dominated by different backgrounds and constrain the related systematic uncertainties that partially affect the background prediction in the SR regions. The

	0 b-tags	1 b-tag	2 b-tags	3 b-tags	≥ 4 b-tags
4 jets	BR, H_T^{had}	BR, H_T^{had}		BR, H_T^{had}	
5 jets	CR, H_T^{had}	CR, H_T^{had}	BR, H_T^{had}	SR, H_T^{had}	SR, H_T^{had}
≥ 6 jets	CR, H_T^{had}	CR, H_T^{had}	BR, H_T^{had}	SR, $m_{b\bar{b}}$	SR, $m_{b\bar{b}}$

Tab. 4.2.: Overview of the different topologies and their use in the analysis as well as the corresponding discriminating variable [163].

scalar sum of the jet transverse momenta $H_T^{\text{had}} = \sum_i p_{\text{T}i}^{\text{jet}}$ is used as a discriminant in the BR and CR regions because it is sensitive to uncertainties that are associated with the jet energy calibration and moreover the $t\bar{t}$ + jets background modelling. By performing the profile likelihood fit including the nuisance parameters of the BR regions to data, the background prediction is improved ("post-fit") with reduced uncertainties and thus the search sensitivity increases. Topologies that are not part of the search, such as 5 jets with 0 or 1 b-tag and 6 jets with 0 or 1 b-tag, are used for the validation of the improved predictions by extrapolating the "post-fit" background distributions across topologies. No significant excess above the background expectation was observed at 95% CL. Thus, an upper limit for the cross-section times branching ratio $\sigma(t\bar{t}H) \times \mathcal{BR}(H \to b\bar{b})$ was derived for a Higgs boson with an assigned mass of 125 GeV. The observed upper limit at 95% CL is $13.1 \times \sigma_{\text{SM}}$ and the expected limit is $10.5 \times \sigma_{\text{SM}}$ [160, 163].

$t\bar{t}H$ analysis strategy

The context of this thesis is a search that was performed early this year. It is based on the 2011 data set of 4.7 fb^{-1} at 7 TeV and the data set that was collected between April and October 2012 at 8 TeV. The latter corresponds to an integrated luminosity of 14.3 fb^{-1} – "HCP data set". Not only the ℓ+jets decay channel of the $t\bar{t}$-system is analyzed but also the dileptonic decay at 7 TeV and 8 TeV. Beside the Higgs decay in two bottom quarks the decay $H \to W^+W^-$ is taken into consideration with both W bosons decaying hadronically. The latter Higgs decay serves as a supplementary source of signal. The classification of event topologies changes slightly compared to the one described in Section 4.1.1 and is summarised in Table 4.3 for the 7 TeV and 8 TeV analysis. In contrast to the analysis in Ref. [160], both for 7 TeV and for 8 TeV, the

analysis is using multivariate analysis (MVA) techniques. In general, artificial neural networks (NN) are used to discriminate signal from background events and are of particular interest in analyses where single variables do not show a clear separation power between background and signal. Thus, in the ℓ+jets channel a neural network discriminant is used instead of the single variable H_T^{had} in the SR region 5 jets and ≥ 4 b-tagged jets. Instead of performing a kinematic fit to the $m_{b\bar{b}}$ single variable in six jets and 3 or more b-tagged jets, the NN discriminant is exploited to improve the separation between signal and background. Hence, more sensitivity to the signal is gained and systematic uncertainties are constrained by exploiting the NN output shape of the different backgrounds. All other topologies still use H_T^{had} as a discriminant in the CR and BR regions (see Table 4.3). The NN gets fed by samples including the $t\bar{t}H$

	0 b-tags	1 b-tag	2 b-tags	3 b-tags	≥ 4 b-tags
4 jets	BR, H_T^{had}	BR, H_T^{had}		BR, H_T^{had}	
5 jets	CR, H_T^{had}	CR, H_T^{had}	BR,H_T^{had}	BR, NN	SR, NN
≥ 6 jets	CR, H_T^{had}	CR, H_T^{had}	BR, H_T^{had}	SR, NN	SR, NN

Tab. 4.3.: Overview of the different topologies and their use in the analysis as well as the corresponding discriminating variables at 7 TeV and 8 TeV. The topologies referred to as SR were blinded.

signal model which is described in more detail in Section 5. The results for the 7 TeV data set used in Ref. [160] is re-analysed using MVA techniques and is compared to the previous result to verify if the performance improves when using MVA approaches. Tests have shown that the MVA improves the signal sensitivity by $\sim 20\%$ compared to the single variable fit. Hence, the analysis for 7 TeV is repeated with the additional Higgs decays and the dilepton channel as described before. The 8 TeV analysis used a blinding procedure in the SR regions to ensure that the nuisance parameters of the fit were consistently describing the uncertainties in the BR and CR region to avoid a bias. The SR regions in Table 4.3 were blinded in the ℓ+jets channel. The corresponding results are not yet published.
The current effort deals with analysing the full data set of the first run of the LHC that corresponds to 20.3 fb^{-1}at 8 TeV by benefiting from the expertise gained by the analysis performed with the HCP data set. The improvement of the background modelling is the main focus. In the ℓ+jets channel, input provided by the Matrix Element Method (MEM) will be implemented if it is available soon and substantial.

4.1.2. Systematic uncertainties

The analysis takes several sources of systematic uncertainties into account that can affect the normalisation and/or the shape of the signal and background distributions. Individual sources of systematic uncertainties are assumed to be uncorrelated. However, specific systematic uncertainties are preserved across processes and different channels. Table 4.4 summarises the systematic uncertainties that are considered in the ATLAS $t\bar{t}H$

analysis. It is indicated if those are taken into account with only the normalisation or both normalisation and shape [160]. An "N" refers to uncertainties that are taken as normalisation-only for all processes and channels that are affected. An "SN" means that the uncertainty is taken into account as both shape and normalisation. Some of the systematic uncertainties are split into several different components for a more accurate treatment. Each systematic uncertainty is associated to a nuisance parameter that is

Systematic uncertainty	Type	Components
Luminosity	N	1
Lepton ID+reco+trigger	N	1
Jet vertex fraction efficiency	N	1
Jet energy scale	SN	16
Jet energy resolution	N	1
b-tagging efficiency	SN	9
c-tagging efficiency	SN	5
Light jet-tagging efficiency	SN	1
$t\bar{t}$ cross-section	N	1
$t\bar{t}V$ cross-section	N	1
Single top cross-section	N	1
Dibosons cross-section	N	1
V+jets normalisation	N	3
Multijet normalisation	N	7
W+heavy-flavour fractions	SN	4
$t\bar{t}$ modelling	SN	3
$t\bar{t}$+heavy-flavour fractions	SN	1
$t\bar{t}H$ **modelling**	N	1

Tab. 4.4.: A list of systematic uncertainties considered in the ATLAS $t\bar{t}H$ analysis [160].

fitted to data in the profile likelihood fit that exploits the constraining power of the BR regions in Table 4.2 and 4.3 in Section 4.1.1. The various background contributions and the signal contribution in different event topologies is illustrated in the various pie charts in Figure 4.1. The systematic uncertainties of the $t\bar{t}$ background are dominated by the $t\bar{t}$ + HF jet modelling, the b-, c- and light-tagging efficiencies, the $t\bar{t}$ + light jet modelling and the jet energy scale (JES) assuming each contribution as uncorrelated [160].
The systematic uncertainty for the LO signal model listed in Table 4.4 was assessed by varying the relevant parameters responsible for the amount of ISR and FSR in PYTHIA 6. The ISR/FSR variation was chosen to be consistent with the experimental data in Ref. [164]. The evaluation of the systematic uncertainties for the $t\bar{t}H$ signal model for both normalisation and shape is part of the objective of the presented work and is described in more detail in Chapter 5.

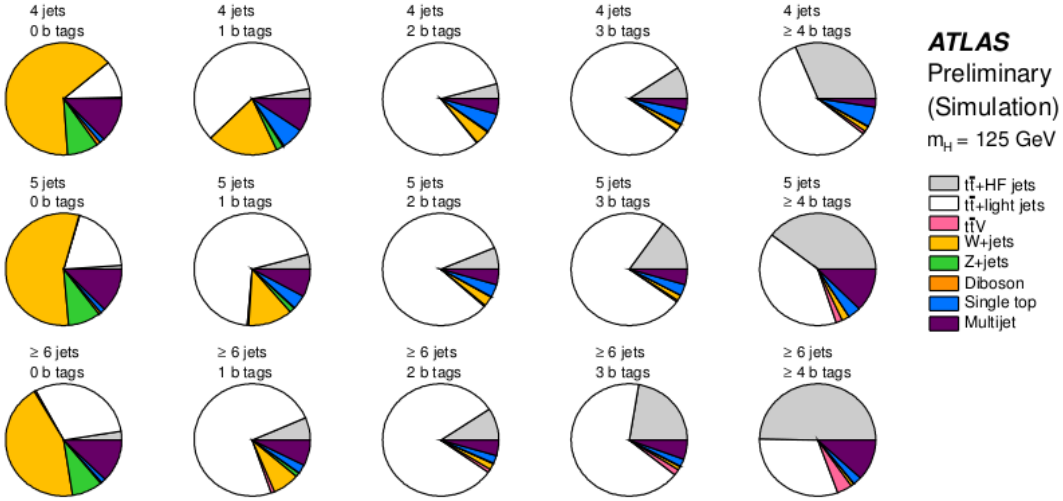

Fig. 4.1.: A series of pie charts showing the fractional contributions of the various backgrounds to the total background prediction in the ℓ+jets channel at 7 TeV. Each row shows the plots for a specific jet multiplicity (4, 5, $\geq$6), and the columns show the b-tagged jet multiplicity (0, 1, 2, 3, $\geq$4) [160].

CHAPTER

FIVE

SIGNAL MODELLING AND CORRESPONDING UNCERTAINTY STUDIES

The modelling of the Higgs production in association with a top-quark pair is of particular importance when analysing the full LHC data set using MVA techniques to gain sensitivity to a Higgs boson signal. Hence, the usage of a persuasive signal model and the evaluation of the corresponding systematic uncertainties is important. The first step in this direction is to study different MC generators and their predictions at different orders in QCD perturbation theory with regard to the $t\bar{t}H$ signal. The influence of the choice of different generation parameters, such as the choice of the factorisation and renormalisation scale, the PDFs, matching schemes, showering models and differing supply of physical features, needs to be evaluated. This chapter is organised as follows: an overview of the MC generators that currently model the $t\bar{t}H$ process at LO and NLO QCD accuracy is given. Furthermore, the used $t\bar{t}H$ production chain is described starting with the ME calculations, followed by the description of the matching to the PS programs. The latter are described with regard to the different MC status of the investigated particles. In addition to the description of the $t\bar{t}H$ signal model and its validation, the evaluation of the associated uncertainties of the model is discussed.

5.1. $t\bar{t}H$ Monte Carlo generators – State of the art

A significant effort was dedicated to increase the accuracy of theoretical predictions in pp collisions in order to match those to the experimental capabilities of the LHC experiments. Therefore, theorists aimed both for providing automatic computations of fixed-order total and differential cross-sections for various processes leading to predictions of the final products of hard ME calculations at parton level, and to match these calculations to PS algorithms that are capable of describing the evolution of the final state particles (parton level) to fragment and to form hadrons (hadron level). MC generators recently reached a point where they serve as fully automated NLO event generators [135, 165, 166] that open the window for the simulation of a new class of processes in the hadron collider phenomenology at NLO QCD accuracy. In principle,

these MC generators provide the opportunity to generate processes without restrictions on the complexity and particle multiplicities of the processes. However, the generation undergoes a lot of challenges in terms of the CPU intensity that increases with increasing complexity and particle multiplicities. Thus, current tools deteriorate when simulating the full production and decay chain at NLO in a reasonable amount of time. According to this, only the generation of undecayed events at NLO accuracy is feasible [167]. The NLO calculations are interfaced to PS algorithms that decay the particles and handle those in their evolution to stable particles resulting in predictions at NLO + PS QCD accuracy. The enormous CPU time-consumption for NLO predictions justifies the usage of LO generators. Furthermore, the latter deliver different features such as the decay of the particles on parton level as well as the description of physical effects, e.g. spin correlations in the top-quark decay. As a result of this, the predictions of the various MC generators available on the market need to be evaluated taking a variety of aspects into consideration both on the modelling side and on the side that deals with the evaluation of the theoretical uncertainties associated with the model. Table 5.1 presents a list of MC generators that are capable of generating $t\bar{t}H$ signal processes which will be discussed and evaluated within the presented work. The next sections provide a brief overview

LO	**NLO**
PYTHIA 6 [168]	POWHEL [169]
PYTHIA 8 [170]	aMC@NLO [134–136]
ALPGEN ($q\bar{q} + N$ jets ($N \leq 4$)) [171]	SHERPA [64, 172, 173]
MADGRAPH [174–176]	

Tab. 5.1.: A list of MC generators that can generate the $t\bar{t}H$ process indicated at LO and NLO QCD accuracy.

about the MC generators including specifications for the prediction of the $t\bar{t}H$ process, starting with generators predicting the process at LO and continuing with those that predict it at NLO QCD accuracy.

5.1.1. LO generators

PYTHIA

The PYTHIA releases (version 6 [168] and 8 [170]) provide both processes $gg \to t\bar{t}H$ and $q\bar{q} \to t\bar{t}H$ at LO QCD accuracy. The latter process is known to have a smaller contribution to the overall cross-section (as is shown for NLO in Figure 2.10b in Section 2.2). The full ME calculation for $gg/q\bar{q} \to t\bar{t}H$ is provided within PYTHIA. However, the complicated multi-body phase-space causes generation times that are slower than the majority of other processes that can be generated with PYTHIA [168]. Beside the ME calculation, PYTHIA handles the PS, MPI, hadronisation and hadron decay as well (ME+PS). The $t\bar{t}H$ signal in Ref. [160] is modelled using PYTHIA 6 and the analysis corresponding to 8 TeV used the predictions of PYTHIA 8 as a starting baseline. The

default scale in those samples is a dynamic scale $\mu_0 = \mu_R = \mu_F = (m_T^t m_T^{\bar{t}} m_T^H)^{1/3}$ where $m_T^2 = m^2 + {p_T}^2$ is defined as the transverse mass.

ALPGEN

ALPGEN [171] provides ME calculations for the $t\bar{t}H$ process with up to four jets and the decay of the parton level top quarks at LO QCD accuracy taking all spin correlations among the decay products into consideration. Thus, it provides one of the most complete descriptions of the $t\bar{t}H$ process that is available at LO so far. The Higgs boson is produced only via its Yukawa coupling to top quarks and no other electroweak process is included. The default scale used in the ALPGEN event generation is $\mu_0 = \mu_R = \mu_F = m_H^2 + \sum m_T^2$ where the sum $\sum m_T^2$ refers to all final state partons including the top quarks. The output of ALPGEN can be interfaced to PS programs such as PYTHIA 6, HERWIG [177, 178] or HERWIG++ [179].

MADGRAPH

MADGRAPH calculates MEs at LO accuracy for the $t\bar{t}H$ process with up to two extra jets. However, the computation of this process is time consuming and first efforts to accelerate the calculations using graphics processing units are ascertained [180]. Only QCD interactions for the production of jets and top quarks are considered whereas the electroweak interactions are only considered for the Higgs production and in the decay of the particles at parton level. Using a generic framework called MADSPIN [181], the possibility to decay the undecayed particles of MADGRAPH at parton level by post-processing the LO event samples before they are passed to PS programs is provided. More information can be found in Refs. [174–176].

5.1.2. NLO generators

NLO accuracy calculations require, aside from the evaluation of LO contributions, the calculations of virtual- and real-emission corrections in perturbation theory as described in Section 2.2.1.

POWHEL

The POWHEL package is based on computed NLO ME calculations provided by HELAC-NLO [182]. POWHEL adopts the FKS substraction scheme [59] to factor out the infrared singularities in the phase-space integration (see Section 2.2.1). The HELAC-1LOOP [182] package is used to numerically evaluate virtual QCD corrections to the scattering amplitudes. Different matching schemes are proposed depending on the QCD accuracy of the calculations [183]. For NLO calculations two methods namely MC@NLO [184] and POWHEG [185, 186], are used to match the hard ME calculations to PSs in the last decade [169]. `POWHEG-BOX` [165] serves as the interface between the NLO calculations and the PS programs such as PYTHIA 6/8 and HERWIG by making use of the matching method POWHEG. POWHEL provides the computation of cross-sections

and the generation of event samples at the NLO + PS QCD accuracy for $t\bar{t}$ pair hadroproduction in association with a third particle or hadronic jet. The total cross-sections are expected to have NLO accuracy, whereas the corresponding differential cross-sections show generally NLO accuracy up to higher-order corrections [169]. The samples that are of particular interest for the scope of this work are the $t\bar{t}H$ predictions at the first radiation emission level, e.g. $t\bar{t}H\ g$.

aMC@NLO

aMC@NLO [134–136] implements a fully automated approach to complete event generation at NLO QCD accuracy and is based on the MADGRAPH 5 package. Automation refers to the ability of aMC@NLO to calculate MEs, to match those to PS programs (PYTHIA 6, HERWIG and HERWIG++) including all ingredients such as one-loop contributions and phase-space substraction in an exclusive software package. The aMC@NLO package is based on the MADFKS framework [187] that uses the FKS substraction method. The virtual corrections are handled by the MADLOOP code [134]. To match the results with PS programs, the MC@NLO method is used. Spin correlation effects for both the decay and the production of generated particles in aMC@NLO can be included using MADSPIN. Thus, NLO predictions for the $t\bar{t}H$ process including spin correlations are available.

SHERPA

SHERPA [64, 172, 173] provides the prediction of the $t\bar{t}H$ process at both LO and NLO QCD accuracy including the shower, MPI, hadronisation and hadron decay of the produced events at parton level [173]. The GOSAM package [188] is used to generate the virtual corrections and is linked to SHERPA that uses AMEGIC [189] as ME generator. The latter implements the Catani-Seymour dipole subtraction method [190] to match the ME calculations with the PS part of SHERPA. Furthermore, all spin correlations in the decay of the top quarks are modelled at tree-level [191].

5.2. Matching

Matching schemes are used to match the ME calculations to the PSs to avoid the double counting of configurations that can be obtained from both the MEs and the PSs. The description by fixed-order MEs of well separated hard partons is excellent compared to their ability in modelling collinear and soft parton emissions due to the appearance of large logarithmic contributions. Moreover, the description of MEs for high parton multiplicities is arduous. The opposite is the case for PSs where soft, low-angle emissions and high particle multiplicities are modelled in a more accurate way. Thus, the combination of both is desirable due to the fact that those predictions are more realistic and closer related to the experiment. In addition, for hadronisation models a good description of soft- and collinear multi-parton states is needed to make adequate predictions. Matching prescriptions separate the phase-space into two distinct regions. As described in Section 2.2, the short distance region is described by the hard scattering

partonic cross-section (see Section 2.2.1) that depends on the calculations of the MEs and the long distance region that is described by showers ensuring the evolution of the high energy particles to rather low energy hadrons as described in Section 2.2.2. In the long distance region, real-emission and virtual corrections are both generated by the shower and in the short distance region, the real corrections are generated by the MEs while the virtual corrections are still generated by the shower. To avoid double counting effects, the phase-space separation needs to be as smooth as possible between the two regions which is ensured by applying matching procedures [192]. Simply speaking, events are erased if ME partons are too soft or if the PS generates radiation that is too hard. For the matching at tree-level, that involves the simultaneous treatment of final states with different multiplicities, several solutions are available such as CKKW [193, 194] and MLM [195]. At NLO, matching techniques apply such as MC@NLO or POWHEG as described above. A systematic uncertainty arising from the used matching scheme needs to be exclusively applied to multi-parton generators, such as MADGRAPH and ALPGEN if extra jets are generated. A detailed overview and a dedicated description of different matching schemes at LO and NLO can be found in Ref. [196].

5.3. Showering tools

In this work, ME calculations are showered either with PYTHIA 6 at 7 TeV or with PYTHIA 8 at 8 TeV. To evaluate and to compare the showered predictions across and within certain PYTHIA releases, the output information given by the PSs is necessary to be well understood. For the scope of this work it is of particular interest to understand, compare and evaluate the information on the parton or truth level. Since the POWHEL predictions represent the central part of this work, a description of post-processing these ME calculations is stressed in the following.

Showering POWHEL

The output format of the POWHEL package is a LES HOUCHES (LHE) event file which includes events at the first radiation emission level, e.g. $t\bar{t}H\ g$, as well as a list of parameters that are used to generate the samples, such as generation cuts, the cross-section, PDFs etc. LHE files provide a common format to store event and process information. They primarily include the output from parton level generators that is used further in PS tools or general-purpose MC generators. The files are organised in a minimal XML-like structure to minimise the parsing efforts [197]. However, the LHE files can be interfaced to PS programs such as PYTHIA [168, 170] or HERWIG [177, 178] for automated simulations of additional radiation emissions (showering), fragmentation, hadronisation and the hadron decay since all essential information is already stored in the LHE files. After running the PS chain, the samples are transformed into Ntuples (`NTUP_TRUTH`) containing all information of the particles on truth level. Both production stages are performed within the ATLAS software framework ATHENA. A list of the provided POWHEL samples as well as a brief summary of parameters being used to compute these is presented in Table F.1 in Appendix F.2.

5.3.1. The MC truth status for PYTHIA 6 and PYTHIA 8

In PYTHIA 6 and PYTHIA 8 every particle in the event record has a specific `mc_status` that explains the current state of the particle, e.g. if it is a beam particle, a parton in preparation of the hadronisation process, a particle produced in the decay process etc. The studies that are presented here are based on particles that are assigned to the hardest subprocess after radiation unless stated otherwise. PYTHIA 6 provides particles with different MC status [168]. However, ATHENA keeps only the particles with `mc_status == 3` for PYTHIA 6. Thus, the performed studies are based on these particles on truth level. The software to perform the studies presented in this work is adjusted to analyse particles both in PYTHIA 6 and PYTHIA 8 at the parton level depending on their individual MC status.

Studies of particles with different MC status

Since the MC status for the particles on parton level changed between PYTHIA 6 and PYTHIA 8, it is necessary to study the particles with different MC status in PYTHIA 8 having the signal model evaluation for the $t\bar{t}H$ analysis at 8 TeV in mind. It is a common consensus in the ATLAS collaboration to switch the versions of PYTHIA from version 6 at 7 TeV to version 8 at 8 TeV. The following three different classifications of particles are investigated:

- `mc_status == 21-29`: particles of the hardest subprocess
- `mc_status == 41-49 || 51-59` : particles produced by ISR or FSR
- `mc_status == 61-69`: particles produced by beam-remnant treatment (copy of the particles after ISR/FSR)

The particles with a `mc_status == 21-29` for the studies at 8 TeV (PYTHIA 8) are chosen. One of the advantages of investigating particles directly from the hard ME calculation is that these are as close to the NLO prediction as possible. But from an experimental point of view, the interest lies on particles that are as closely related to the ones observed in the experiment as possible. Thus, particles after the full treatment of the PS generator (after ISR and FSR) are of particular interest. Figure 5.1 shows the anti-top p_{T}, $t\bar{t}$ η, p_{T} and $t\bar{t}H$ p_{T} distribution with the particle MC status that are listed above. A good agreement is seen between the yellow and the red distributions for all kinematic variables. These are the distributions of particles after the full PS generator treatment. Discrepancies between the latter distributions and the distributions in blue emerge. This is due to the fact that the blue curves are the result of particles of the hard ME before any PS generator treatment. Hence, a softer spectrum for the blue distributions is observed whereas the other histograms (red and yellow) are harder due to ISR and FSR. In particular, this effect is seen in the p_{T} distributions of the $t\bar{t}H$-system. The p_{T} spectrum of the four-vector sum of the top, the antitop and the Higgs distribution is zero for all events (blue curve) as expected for the $t\bar{t}H$-system. The studies with PYTHIA 8 that are performed in this thesis are based on particles with `mc_status == 61-69`, since the particles with this MC status are as closely related to the particles that are observed in

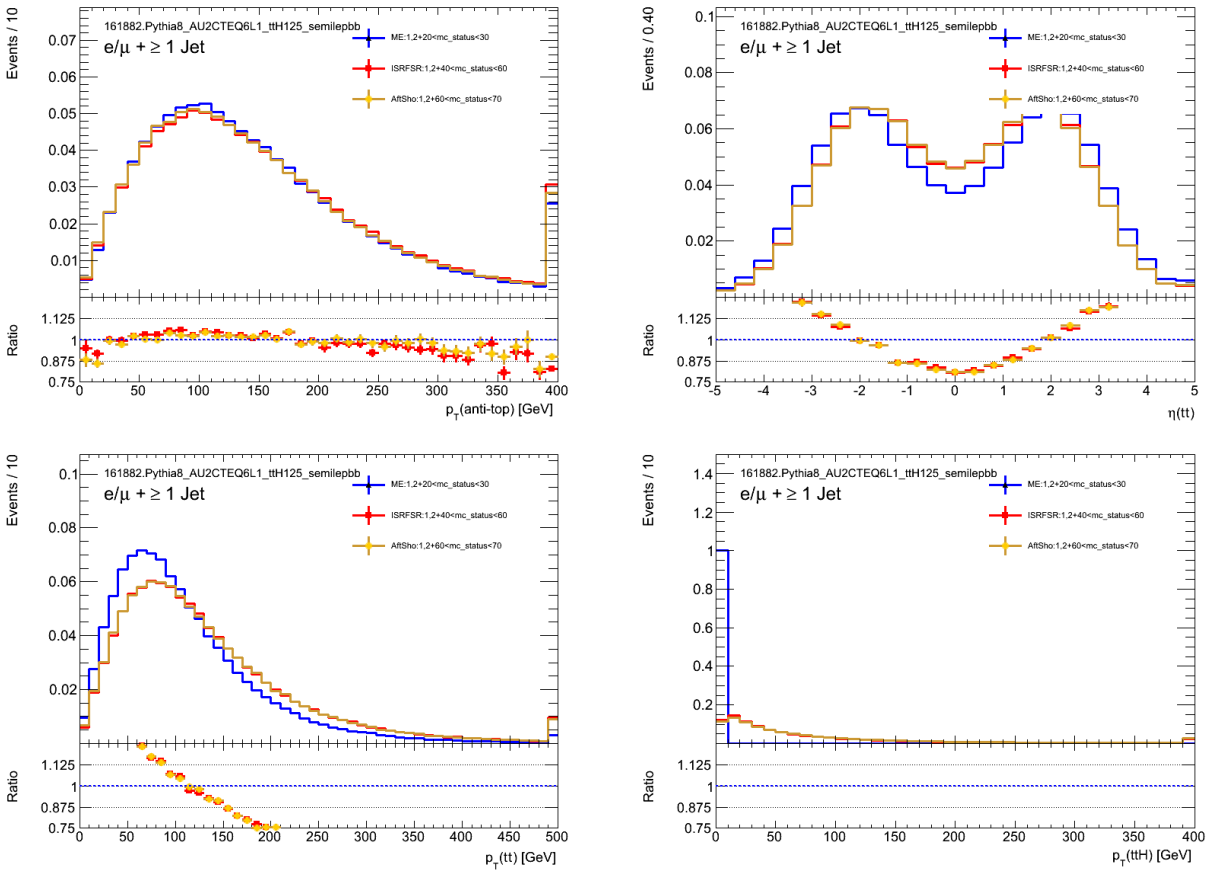

Fig. 5.1.: The anti-top p_{T}, $t\bar{t}$ η, p_{T} and $t\bar{t}H$ p_{T} distribution for particles with a MC status of 21-29 (blue), 41-49 or 51-59 (red) and 61-69 (yellow) in the 1 jet inclusive channel for PYTHIA 8.

the detector.
As described above, the top, anti-top and Higgs have MC status of 3 in the studies with PYTHIA 6 due to the use of the ATHENA framework. Following the studies for PYTHIA 8, it is concluded that the particles in PYTHIA 6 with a MC status of 3 correspond to particles of the hard process after radiation. This is manifested in the $t\bar{t}H$-system p_{T} distribution of Figure 5.2a in Section 5.4.1. The p_{T} spectrum of the $t\bar{t}H$-system is not vanishing.

5.4. The $t\bar{t}H$ signal model: LO and NLO studies

LO predictions show large dependencies on the factorisation and renormalisation scale resulting in large theoretical uncertainties. NLO calculations [11, 66, 135, 198] predict an inclusive SM rate of 0.137 pb for a center-of-mass energy of 8 TeV and 0.632 pb for 14 TeV with a theoretical uncertainty of $\mathcal{O}(10\%)$ at the LHC [199]. In addition, fully automated NLO calculations are available for the $t\bar{t}H$ production as described in Section 5.1.2, resulting in reduced theoretical uncertainties both for the differential cross-section and the shape (see Section 2.2.3). Hence, it is reasonable to use a NLO signal model

as baseline for the analysis. Before changing the signal model from LO to NLO, the NLO model needs to be understood. This is done by comparing both predictions. As described in Section 5.1.1, the $t\bar{t}H$ signal process in the ATLAS analysis [160] is modelled using PYTHIA 6 at 7 TeV and PYTHIA 8 at 8 TeV. This corresponds to the LO QCD accuracy of the model. The signal sample at 7 TeV[1] that is used to perform the following studies uses the MRST LO** set of PDFs [200] that are rather old and have been superseded by the MSTW PDF sets [201], a Higgs mass of 125 GeV, a top-quark mass of 172.5 GeV and includes the Higgs decay into two bottom quarks ($H \to b\bar{b}$) for the ℓ+jets decay channel of the $t\bar{t}$-system. The comparisons are performed also for 8 TeV. Therefore, the 8 TeV PYTHIA signal sample[2] that is generated using the CTEQ6L1 PDF set [202], a Higgs mass of 125 GeV and includes the ℓ+jets decay channel as well as the Higgs decay into two bottom quarks is used. Both PYTHIA samples (at 7 TeV and 8 TeV) are produced using a dynamic scale $\mu_0 = \mu_R = \mu_F = (m_T^t m_T^{\bar{t}} m_T^H)^{1/3}$. The mentioned PYTHIA samples are compared to the POWHEL [198] NLO predictions. The inclusive POWHEL samples (listed in Table F.1) at 7 TeV (8 TeV) are interfaced to PYTHIA 6 (PYTHIA 8) for showering and hadronisation to match the LO $t\bar{t}H$ samples. The POWHEL samples are generated with the CTEQ6.6M PDF set, $m_H = 125$ GeV, $m_t = 172.5$ GeV and a static scale $\mu_0 = \mu_R = \mu_F = m_t + m_H/2$ at 7 TeV and 8 TeV. The decay of the Higgs boson is inclusive. An ℓ+jets event selection on truth level excluding the W boson decay into τ leptons with a jet p_{T} cut of $p_{\mathrm{T}} > 25$ GeV and $|\eta| < 2.5$ was applied to both the PYTHIA and the POWHEL samples. Particle jets are reconstructed using the ANTIKT algorithm [203] with the recombination radius parameter $\Delta R = 0.4$. Kinematic differences are observed between the LO predictions by PYTHIA and the NLO predictions by POWHEL. At 7 TeV and 8 TeV, the most significant discrepancies arise in the kinematic distributions for $t\bar{t}H$ p_{T}, $t\bar{t}$ η and top p_{T}. These discrepancies lead to the reweighting procedure that is described in the following and are represented in the distributions referred to as "before reweighting" at 7 TeV in Figure A.1 and A.2 in Appendix A.1 and at 8 TeV in Figure A.3 and A.4 in Appendix A.2.

5.4.1. LO to NLO reweighting

Due to the fact that the production of the NLO $t\bar{t}H$ signal samples within the full ATLAS simulation chain is very time-consuming, the first step is to compare the $t\bar{t}H$ kinematic distributions at truth level between PYTHIA and POWHEL. The occurrence of kinematic differences resulted in attempting to reproduce the POWHEL model by reweighting the PYTHIA signal model.

LO to NLO reweighting at 7 TeV

For 7 TeV, significant differences between PYTHIA and POWHEL occurred in the $t\bar{t}H$ p_{T}, $t\bar{t}$ η and top p_{T} distributions. PYTHIA 6 predicts a harder p_{T} spectrum of the $t\bar{t}H$

[1] mc11_7TeV.116301.Pythia_ttH125_poslepnu_jj_bb.evgen.EVNT.e997 -ATHENA v.17.0.6.4 and mc11_7TeV.116301.Pythia_ttH125_neglepnu_jj_bb.evgen.EVNT.e997 - ATHENA v.17.0.6.4.6.

[2] mc12_8TeV.161882.Pythia8_AU2CTEQ6L1_ttH125_semilepbb.merge.NTUP_TOP.e1441 - ATHENA v.17.2.5.2.4

and top p_{T} and a more central distribution in $t\bar{t}$ η distributions as shown in Figure 5.2. This is due to the $t\bar{t}H$ production in POWHEL with one extra QCD radiation, e.g. $t\bar{t}H$ g

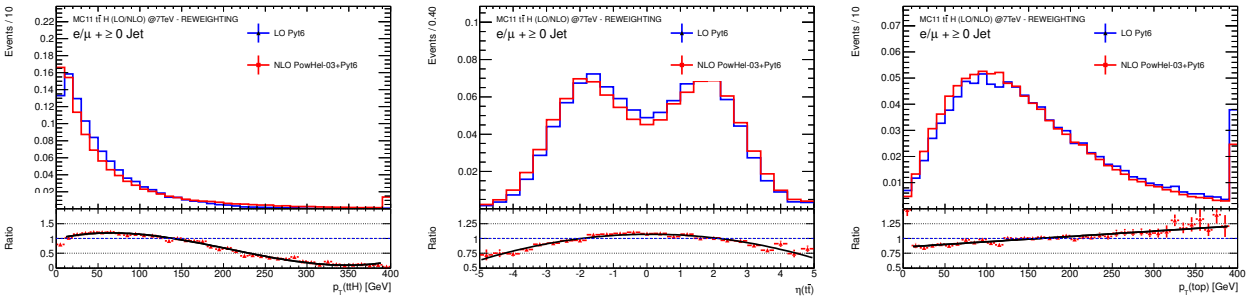

(a) $t\bar{t}H$ p_{T} ***(b)*** $t\bar{t}$ η ***(c)*** top p_{T}

Fig. 5.2.: The $t\bar{t}H$ p_{T} (a), $t\bar{t}$ η (b) and top p_{T} (c) distributions in PYTHIA 6 and POWHEL showered with PYTHIA 6. The black line shows the third-order ($t\bar{t}H$ p_{T}), second-order ($t\bar{t}$ η) and first-order polynomial fit (top p_{T}) to the ratio of the LO and NLO histograms. The first- and third-order polynomial fits do not contain the first and the overflow bin. These are handled as a bin-by-bin ratio of the histograms. The latter are normalised to unity.

that changes the boost of the $t\bar{t}H$-system. The latter reflects the four-vector sum of the top, the anti-top quark and the Higgs boson from the hard process. The inclusion of the extra parton emission in the NLO ME calculation results in a more accurate description of the p_{T} spectrum in high-p_{T} regions ($p_{\mathrm{T}} \gtrsim 160$ GeV) and a divergent behaviour in low p_{T} regions. The latter is due to the fact that the NLO MEs are not that accurate in describing collinear emissions that decrease the p_{T} of the $t\bar{t}H$-system. However, the opposite is the case for LO ME calculations that are more affected by extra parton emissions which are added by the PS. Thus, collinear emissions are well described resulting in a good description for low p_{T} regions but a bad modelling in high-p_{T} regions for the LO calculations. The LO prediction undershoots the NLO predictions in that region since hard radiations are modelled more accurately in the NLO ME calculations. Three functions (see Appendix A.1.1) are derived from the ratios of the corresponding distributions to reweight the PYTHIA 6 signal sample to match the kinematics of the POWHEL sample. First, the ratio of the $t\bar{t}H$ p_{T} distributions in PYTHIA 6 and POWHEL is fitted using a third-order polynomial function excluding the first and the overflow bin because they did not fulfill the fit requirements. The first and the overflow bin are taken into account as a bin-by-bin ratio which is the ratio of the two histograms (LO/NLO). The resulting function is applied to the PYTHIA 6 signal sample as an event weight. As a next step, a second-order polynomial function is fitted to the ratio of the $t\bar{t}$ η distribution and applied to the LO sample. Finally, the top p_{T} ratio is fitted using a first-order polynomial function excluding the first and the overflow bins. The product of the three reweighting functions is applied to the PYTHIA 6 sample assuming that the kinematic variables used to derive the functions are uncorrelated. Figure A.1 and A.2 in Appendix A.1 shows a comparison of the distributions between PYTHIA 6 and POWHEL before and after reweighting. The procedure improves the agreement between the two generators also in the variables that are not used for reweighting, e.g. Higgs η,

as illustrated in Figure 5.3.

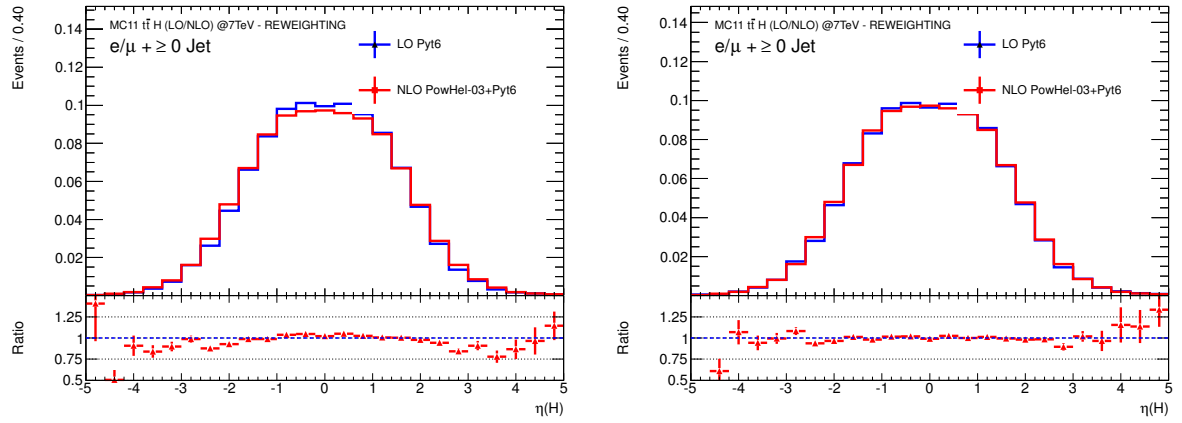

(a) before reweighting ***(b)*** after reweighting

Fig. 5.3.: The Higgs η distribution before (a) and after (b) reweighting the variables $t\bar{t}H$ p_{T}, $t\bar{t}$ η and top p_{T} at 7 TeV. The distributions are normalised to unity.

LO to NLO reweighting at 8 TeV

For 8 TeV, differences between the $t\bar{t}H$ kinematics in PYTHIA 8 and in POWHEL are less significant and come mainly from the difference in the $t\bar{t}H$ p_{T} distributions. As in 7 TeV, PYTHIA 8 predicts a harder $t\bar{t}H$ p_{T} distribution than POWHEL as described in the former section. Thus, a first order polynomial function (see Appendix A.2.1) is derived from a fit to the ratio of the $t\bar{t}H$ p_{T} distributions in PYTHIA 8 and POWHEL excluding

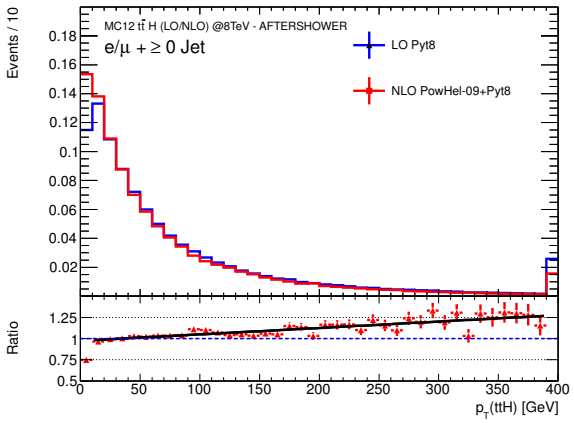

Fig. 5.4.: The $t\bar{t}H$ p_{T} distribution in PYTHIA 8 and POWHEL showered with PYTHIA 8 (normalised to unity). The black line shows a linear fit to the ratio of the different p_{T} distributions. The first and the overflow bin are treated as the ratio of the two histograms.

the first and the overflow bin as shown in Figure 5.4. The latter are taken into account as a bin-by-bin ratio. The resulting reweighting function is applied as a multiplicative

factor to each event (event weight) of the PYTHIA 8 signal sample. Figure A.3 and A.4 in Appendix A.2 shows the kinematic distributions for PYTHIA 8 and POWHEL showered with PYTHIA 8 before and after applying the reweighting function to the LO sample. A good agreement between the kinematic distributions is observed after reweighting the $t\bar{t}H$ p_{T} distribution.

5.4.2. Signal reweighting impact on the $t\bar{t}H$ analysis

The $t\bar{t}H$ signal reweighting is applied to the 8 TeV analysis for the ℓ+jets and the dileptonic decay of the $t\bar{t}$-system. Figure 5.5 shows the kinematic variable H_T^{had} for the

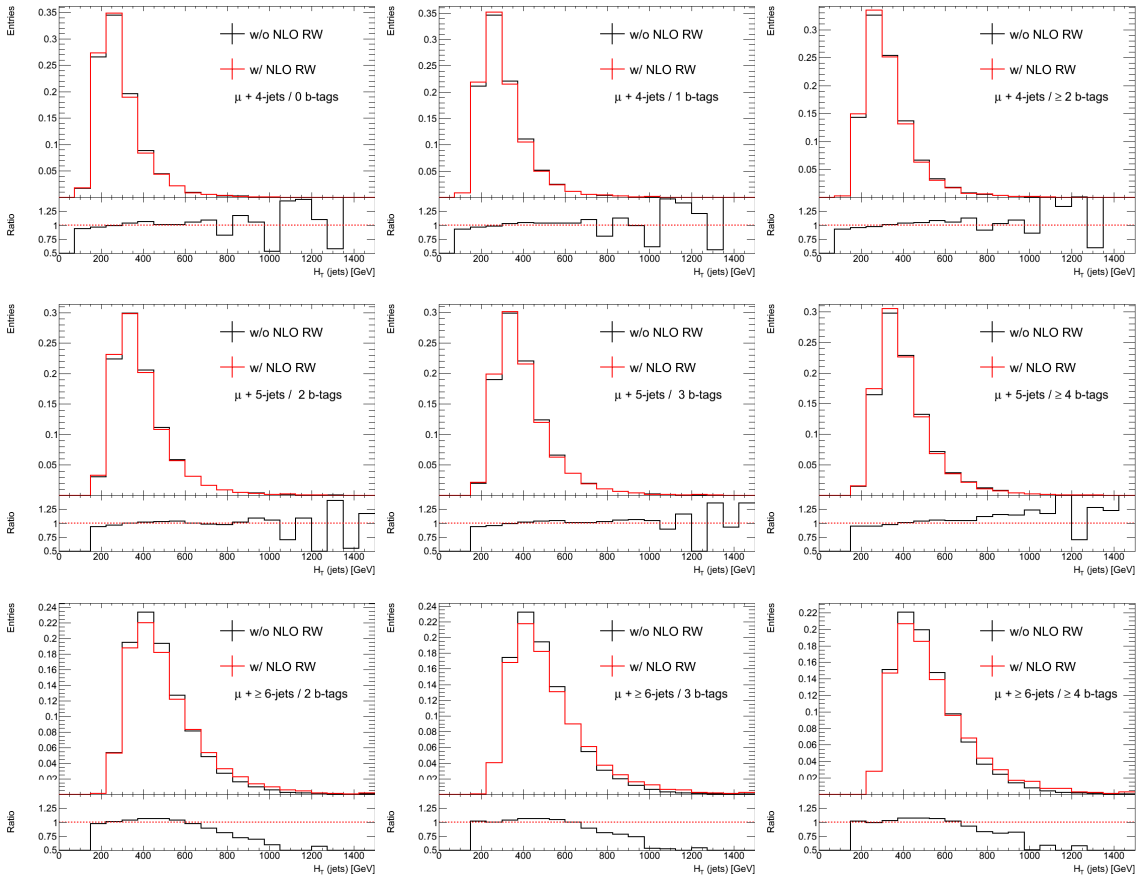

Fig. 5.5.: H_T^{had} at 8 TeV for nine event topologies organised according to the number of jets and the number of jets that are b-tagged. The distributions are normalised to unity for shape comparisons.

nine event topologies that are used in the search for a $t\bar{t}H$ signal according to the number of jets and the number of jets that are reconstructed as b-jets as described in Chapter 4. The distributions are normalised to unity. The ℓ+jets channel is presented with the leptonic W boson decay to muons after the $t\bar{t}H$ event selection and reconstruction of the particles. The presented plots refer to the signal model after the full ATLAS simulation including the detector simulation before (black) and after (red) reweighting the PYTHIA

sample to the POWHEL sample at 8 TeV. The reweighting at 8 TeV used a reweighting function extracted by the $t\bar{t}H$ p_{T} distribution at truth level. H_T^{had} is directly related to the $t\bar{t}H$-system since it is defined as the scalar sum of all transverse momenta of the jets per event. The same trend in every event topology for H_T^{had} is seen at detector level compared to the $t\bar{t}H$ p_{T} distribution at truth level. Before reweighting the LO sample to NLO, the signal model is harder than after applying the reweighting. This has an impact on the expected signal yield. Since the $t\bar{t}H$ p_{T} is softer at NLO, less events are passing the event selection. According to this, the event selection efficiency is decreased which results in a loss of the overall sensitivity.

5.5. Higher-order corrections estimation: scale variation studies

To estimate higher-order corrections of the NLO signal model, a systematic uncertainty is applied to the POWHEL samples with factorisation and renormalisation scales varied by a factor of two in both directions with respect to the nominal scale for 7 TeV and 8 TeV as described in Section 2.2.3. The systematic uncertainty for the LO signal model in Ref. [160] was assessed by varying the relevant parameters responsible for the amount of ISR and FSR in PYTHIA 6. The ISR/FSR variation is chosen to be consistent with the experimental data in Ref. [164].

5.5.1. Scale variation studies at 7 TeV

To assess a systematic uncertainty on the signal model – both on the normalisation and the shape of the distributions – POWHEL samples with up (red) and down scale (blue) variations are investigated. Hence, the static scale of the nominal sample at 7 TeV (sample number 3 in Table F.1) with a Higgs mass of 125 GeV is varied by a factor of two in both directions (sample number 8 and 9 in Table F.1) as explained in Section 2.2.3. According to the 7 TeV analysis, all three samples are showered using PYTHIA 6 and the used PDF set is CTEQ6.6M. All jets are required to pass the cuts of $p_{\mathrm{T}} > 25$ GeV and $|\eta| < 2.5$. The left column in Figure B.1 and B.2 in Appendix B.1 shows that significant discrepancies occur in different kinematic distributions such as in $t\bar{t}H$ p_{T} and η, top p_{T} and $t\bar{t}$ p_{T} with respect to the shape of the distribution. The $t\bar{t}H$-system is reconstructed using the four-vector sum of the top, anti-top and the Higgs each originating from the hard process. To visualise the impact of the shape of the distributions they are either normalised to unity or to see the effect on the rate the samples are normalised to the corresponding sample cross-section (as listed in Table F.1). The latter kinematic distributions such as top p_{T} and $t\bar{t}H$ η are depicted in Figure 5.6. The differences in the cross-section are as expected. As shown in Section 2.2.3, it is predicted that the sample with the downwards scale variation has a larger cross-section with respect to the nominal sample whereas for the upwards varied sample the opposite is the case.
Since signal samples with scale variations that are simulated by the full ATLAS simulation are not provided, the nominal signal sample is reweighted to match the kinematics of the samples with varied scales. Hence, two reweighting functions for top and $t\bar{t}H$ p_{T}

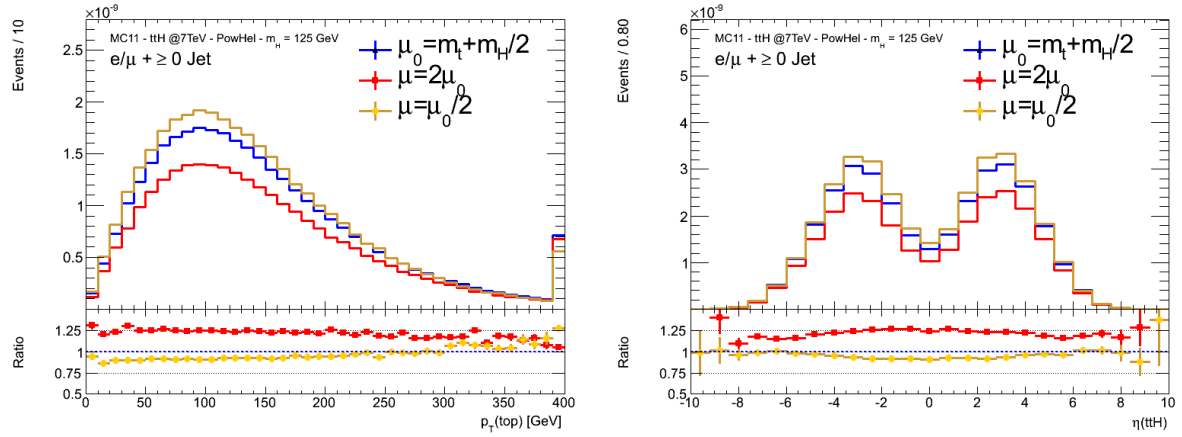

(a) *(b)*

Fig. 5.6.: The top p_{T} (a) and $t\bar{t}H$ η (b) distributions normalised to the sample cross-section in the zero jet inclusive channel. Clear differences between the up/down scaled samples are manifested with respect to the nominal sample at 7 TeV.

are derived and checked by the occurrence of the closure between the nominal and the up and down scaled samples, respectively. Therefore, the ratio of the $t\bar{t}H$ p_{T} histograms for the up and the down scaled POWHEL samples with respect to the nominal sample are stored for each bin. In a second step, the resulting numbers are applied to the up and down scaled samples as a multiplicative factor for each event (event weight). In addition, the same procedure is done for the top p_{T} distribution. The two resulting event weights are applied to the corresponding up or down scaled sample. The result is shown in Figure B.1 and B.2. The reweighting procedure ensures a closure in the top and $t\bar{t}H$ p_{T} distributions after reweighting. Also other variables such as $t\bar{t}H$ η and $t\bar{t}$ p_{T} are influenced by the reweighting procedure. As expected, the up/down scaled samples show a better agreement with the nominal sample in these variables. The total closure in $t\bar{t}H$ p_{T} after reweighting $t\bar{t}H$ p_{T} starts to deviate after the reweighting of top p_{T}. This indicates that small correlations between the variables used for reweighting exist. However, the deviations appear only in high-p_{T} regions ($p_{\mathrm{T}} > 250$), do not exceed 5% and are covered by statistical fluctuations. It is important to note that the inverse of the event weight is applied to the reweighted signal sample to assess a systematic uncertainty on the modelling.

5.5.2. Scale variation studies at 8 TeV

The procedure is also applied to the 8 TeV POWHEL sample that is showered with PYTHIA 8. The nominal sample number 10 and the samples with up scale (sample number 11) and down scale variation (sample number 12) in Table F.1 is ascertained. The same kinematic cuts are applied to the jets as for 7 TeV. Figure B.3 and B.4 in Appendix B.2 depicts the effect of the reweighting procedure that used the same variables as for 7 TeV. The same effects at 7 TeV and 8 TeV are observed. Thus, the procedure to assess systematic uncertainties to the signal model originating from varying the

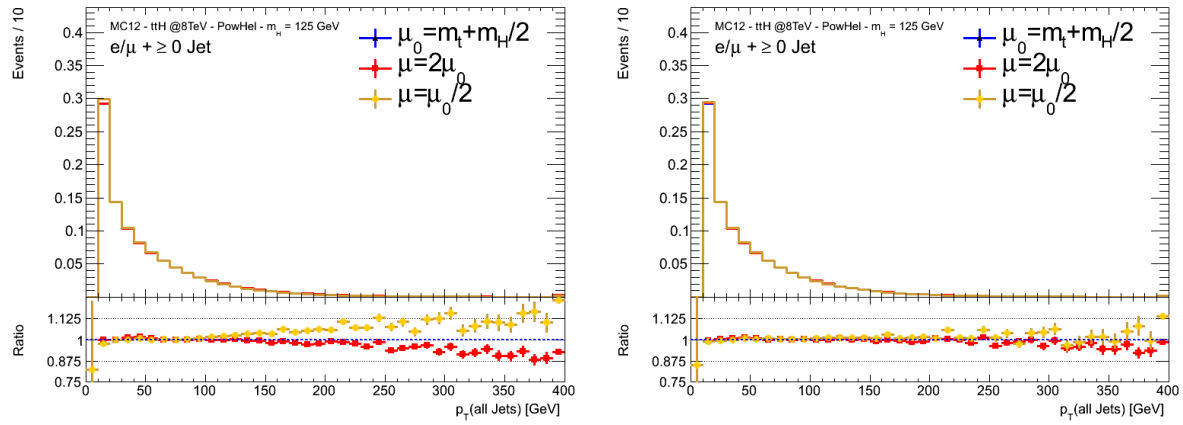

(a) before reweighting

(b) after reweighting

Fig. 5.7.: The p_{T} distributions of all jets before (a) and after (b) reweighting the variables $t\bar{t}H$ p_{T} and top p_{T} at 8 TeV.

factorisation and renormalisation scale by a factor of 2 is validated. The systematic uncertainty reweighting procedure in the two variables $t\bar{t}H$ p_{T} and top p_{T} is valid within the statistical uncertainties. It is worth mentioning that the high-p_{T} regions in the kinematic distributions are more affected by the reweighting procedure than those of moderate and low p_{T}. This can be seen in the p_{T} distribution for all jets as depicted in Figure 5.7.

5.6. Evaluation of the choice of the scale

As described in Section 2.2.3, the choice of the renormalisation and factorisation scale when generating processes is rather subjective. However, the choice of the scale is based on prior considerations that need to be taken into account. The chosen scale should hinder the occurrence of logarithmic divergencies for higher-order contributions in perturbation theory. This can be ensured when the hard probing scale Q is of the order of the renormalisation/factorisation scale μ. In general, two types of scales are distinguished. Static scales depend on fixed parameters such as the mass of a particle and are event independent. Dynamic scales depend on kinematic variables that are event dependent such as the transverse momenta of particles. The choice of a static scale is reasonable for the description of a process at its production threshold and is less vulnerable with regard to theoretical divergencies. Dynamic scales are more sensitive to the latter but provide a good description not only at the production threshold but also in regions above and below it.

5.6.1. Choice of the scale in POWHEL

The POWHEL samples with a dynamic scale $\mu_0 = (m_T^t m_T^{\bar{t}} m_T^H)^{1/3}$ and a static scale $\mu_0 = m_t + m_H/2$ both with $m_H = 125$ GeV are used (see Table F.1). The samples

are normalised to an integrated luminosity of 4.7 fb^{-1} for 7 TeV (14.3 fb^{-1} for 8 TeV) and the cross-section $\sigma(t\bar{t}H \to \ell + \text{jets}, \text{H} \to \text{b}\bar{\text{b}})$ excluding the W boson decay into τ leptons after a selection of the hard process particles on truth level to see the effect of the normalisation. However, to investigate the shapes of the predictions, the samples are normalised to unity. The dynamic scale is the same one that is used for the PYTHIA 6 (PYTHIA 8) signal sample at 7 TeV (8 TeV).

Studies on the choice of the scale at 7 TeV and 8 TeV

For the evaluation of the scale choice at 7 TeV (8 TeV) sample number 3 and 13 (sample number 10 and 14) in Table F.1 are compared. The samples are generated with $m_t = 172.5$ GeV and $m_H = 125$ GeV. Beside the difference in the used scale, the samples with the static scale use the CTEQ6.6M PDF set and the samples with the dynamic scale use the CT10nlo PDF set [49]. The latter have a slightly higher cross-section than the former.

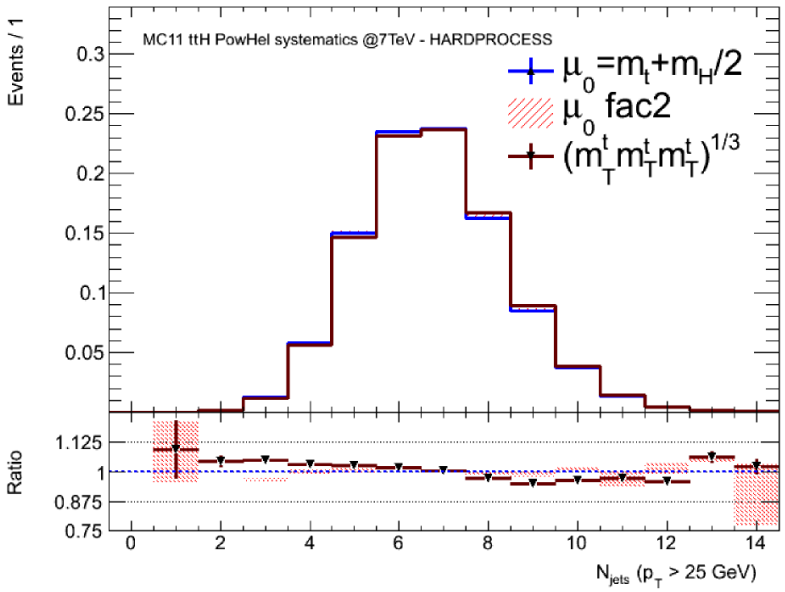

Fig. 5.8.: The jet multiplicity distributions normalised to unity after applying a cut of $p_\text{T} > 25$ GeV and $|\eta| < 2.5$ on the truth jets at 7 TeV.

However, no appreciable differences between the samples with varying PDF sets are observed as described in Section 5.8. Figure 5.8 shows the jet multiplicity distributions for all jets after a minimum p_T cut of 25 GeV and $|\eta| < 2.5$ including the sample with the static scale (blue), its systematic uncertainty arising from the scale variations (red shaded area) as described in Section 5.5.1 and the sample with the dynamic scale (brown) at 7 TeV. The dynamic scale predicts slightly more jets in higher jet multiplicity bins and slightly less in low jet bins. The jet prediction of the dynamic scale is not covered by the applied systematic uncertainty of the static scale. For 7 TeV, more kinematic distributions inclusive in the jet multiplicity such as the p_T and η distribution for the Higgs boson, the top quark and the $t\bar{t}H$-system are depicted in Figure 5.9. The p_T distributions for the Higgs and the top quark show the same trends in the regions of

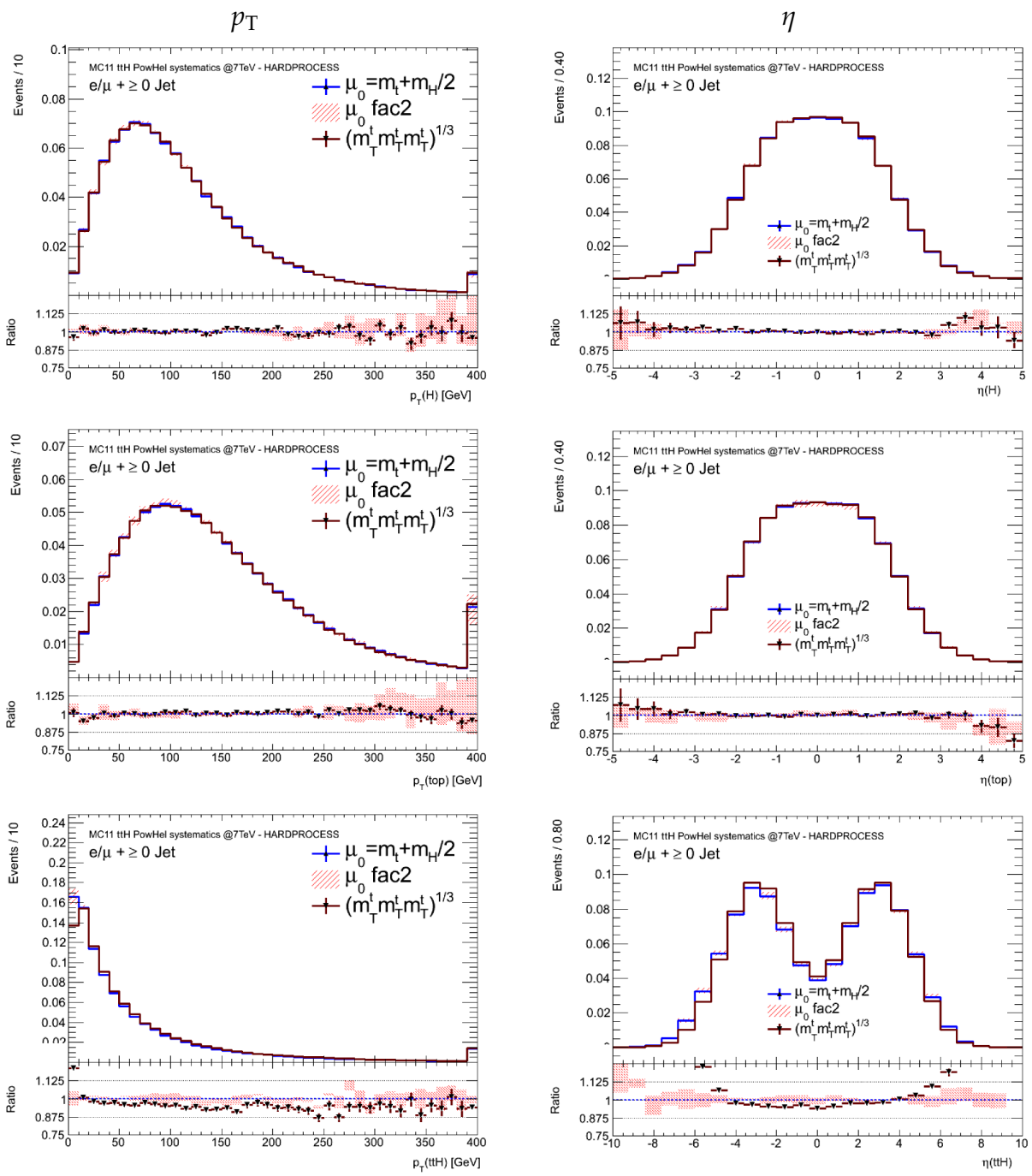

Fig. 5.9.: The p_T and $|\eta|$ distribution for the Higgs, the top quark and the $t\bar{t}H$-system in the zero jet inclusive channel normalised to unity at 7 TeV.

sufficient statistics. The POWHEL authors expected no difference for the p_T distribution up to $\sim$ 200 GeV which is confirmed. Moreover, a discrepancy is expected for the threshold of the static scale at 232.5 GeV which is neither reflected in the presented nor in other kinematic distributions that are ascertained. However, the predictions of the dynamic scale are covered by the systematic uncertainty of the static scale over the

whole spectrum in p_T and η for the Higgs and the top quark (first two rows in Figure 5.9). The $t\bar{t}H$-system p_T and η shows discrepancies (third row in Figure 5.9). The $t\bar{t}H$ p_T is harder and η is more central for the dynamic scale. Since the $t\bar{t}H$-system kinematics are sensitive to extra QCD radiation and the dynamic scale predicts more jets than the static scale in high jet multiplicity bins, the $t\bar{t}H$-system is slightly boosted for the dynamic scale. Furthermore, a dynamic scale describes high-p_T regions more accurately than a static scale. Thus, adding an additional systematic uncertainty to the POWHEL signal sample arising from kinematic differences is required since the $t\bar{t}H$ p_T variable is used for the LO to NLO reweighting procedures as described in Section 5.4.1. The same conclusions are also valid for the studies that are performed for 8 TeV. A selection of kinematic distributions at 8 TeV is illustrated in Figure C.1 in Appendix C.1.

5.6.2. Choice of the scale in ALPGEN

As stated in Section 5.1.1, ALPGEN is a LO multi-leg MC generator that handles the decay of the hard process particles. Furthermore, the spin correlations in the top-quark decay are modelled (see Section 5.7.1). ALPGEN provides additional features compared to POWHEL and is thus investigated.
The LO predictions suffer from large theoretical scale uncertainties as described in Section 5.4. Thus, a dedicated study of the choice of the scale for the $t\bar{t}H$ process provided by ALPGEN is necessary. Two different choices of scales are investigated and compared to the predictions of POWHEL. The ALPGEN samples are generated with

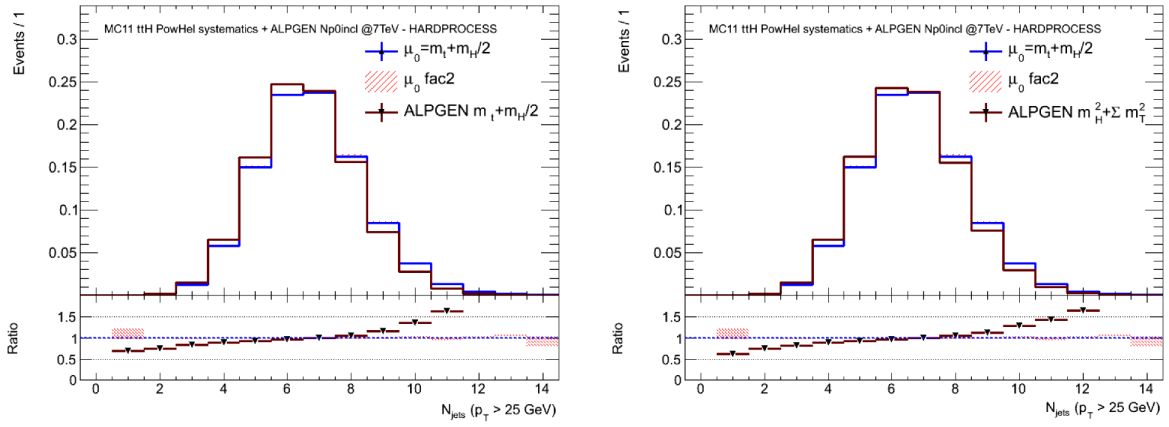

(a) *(b)*

Fig. 5.10.: The jet multiplicity distributions normalised to unity after applying a cut of $p_T > 25$ GeV and $|\eta| < 2.5$ on the truth jets. Figure a (b) shows the distribution for the static (dynamic) scale.

kinematic configurations defined by cuts that are applied to the following variables at parton level:

- ${p_T}^{\text{jet}} > 15$ GeV, $\eta^{\text{jet}} < 6, \Delta R_{jj} > 0.7$,
- ${p_T}^{b} > 0$ GeV, $\eta_b < 6$ and $\Delta R_{b\bar{b}} > 0$.

The CTEQ6.1L PDF set, $m_H = 125$ GeV and $m_t = 172.5$ GeV are used to generate the $t\bar{t}H$ sample. In contrast to the POWHEL predictions, ALPGEN simulates the decay of the

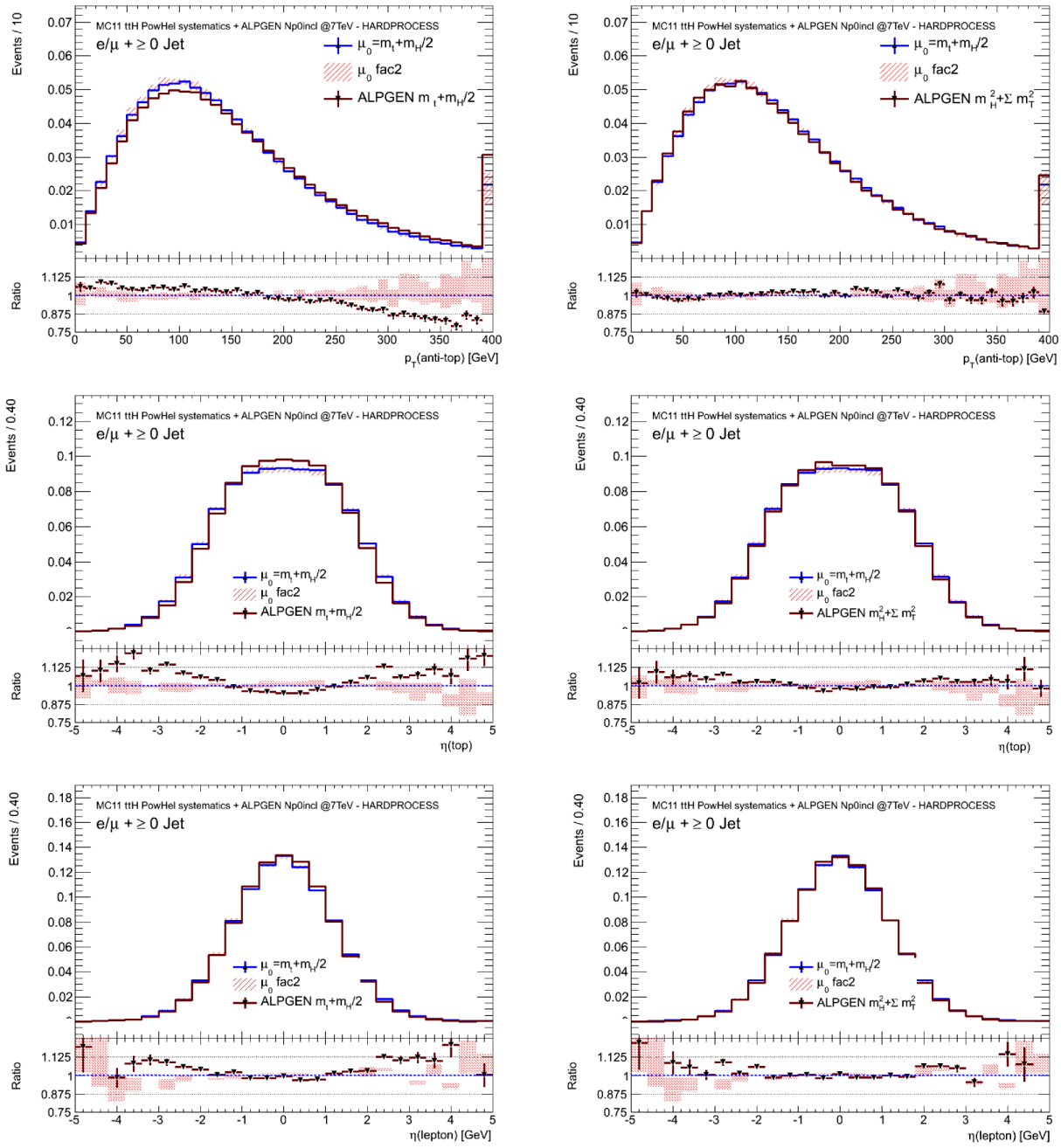

Fig. 5.11.: ALPGEN with the static scale (left) and the dynamic scale (right) compared to POWHEL and its associated systematic uncertainty originating from the scale variations in the 0 jet inclusive. The first row shows the anti-top p_{T}, the second the top η and the third row depicts the lepton η distributions. The distributions are normalised to unity.

generated top quarks into three fermions. The top-quark decay is selected to be fully inclusive. ALPGEN provides $t\bar{t}H$ predictions with up to four extra partons. However,

the sample to investigate the choice of the scale is generated with zero extra partons inclusive (Np0incl), for the purpose of faster production times. An ALPGEN sample with the same static scale as used for the generation of the POWHEL samples is produced ($\mu_0 = \mu_R = \mu_F = m_t + m_H/2$). In addition, an ALPGEN sample with the dynamic scale $\mu_0 = \mu_R = \mu_F = m_H^2 + \sum m_T^2$, which is the default for the $t\bar{t}H$ process in ALPGEN, is generated. Both samples are interfaced to PYTHIA 6 at 7 TeV. Interfacing the ALPGEN output to PYTHIA 8 is not available so far and thus the studies rely on 7 TeV. A selection of the hard process particles at truth level and two cuts on particle jets ($p_T > 25$ GeV and $|\eta| < 2.5$) are applied. Afterwards, the samples are normalised to their sample cross-section. The cross-section for the sample with the dynamic scale is 60.194 ± 0.047 fb and the cross-section for the static scale is 71.553 ± 0.055 fb. Both cross-sections are in agreement with the suggested cross-sections in Ref. [130]. Figure 5.10 depicts the jet multiplicity distribution for the POWHEL predictions (blue) that uses the static scale, its associated systematic uncertainty originating from the scale variations (red shaded area) and the ALPGEN predictions with the static scale (left plots) and the dynamic scale (right plots) after applying the two jet cuts as described above. It shows that for both scales, the predicted number of jets is higher at lower jet multiplicity bins and lower for high jet bins compared to the POWHEL predictions. This reflects what is expected for a LO sample with no extra QCD radiation at the parton level. However, having a look at other kinematic distributions at truth level, differences between the two scales used in ALPGEN arise. Figure 5.11 shows a selection of kinematic distributions, namely the

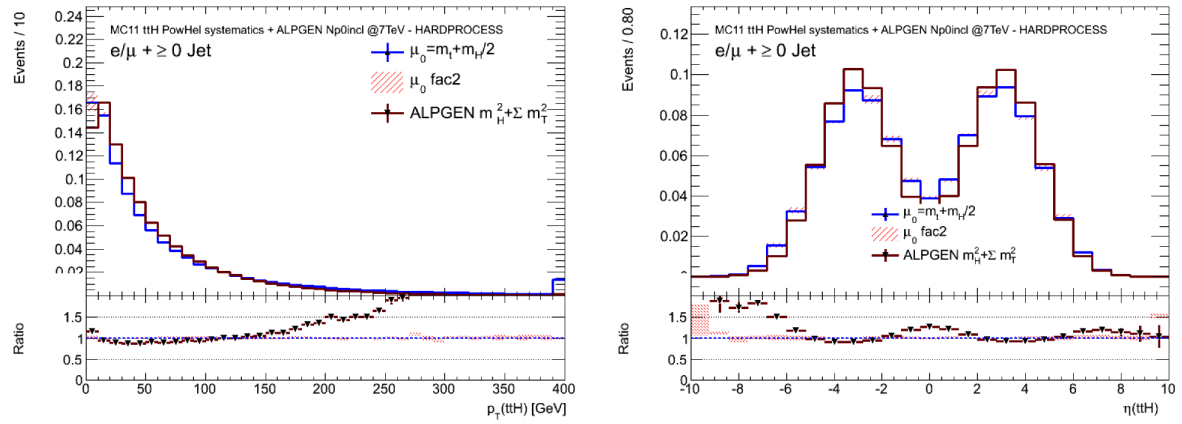

(a) ***(b)***

Fig. 5.12.: The $t\bar{t}H$ p_T (a) and η (b) distributions for the zero jet inclusive channel after normalisation to unity.

anti-top p_T, top η and lepton η distribution. The latter contains all leptons originating from the W boson decay excluding the τ leptons. Whereas the uncertainty band of the POWHEL prediction covers the predictions of the ALPGEN sample with the dynamic scale (right plots in Figure 5.11), the ALPGEN sample with the static scale (plots on the left in Figure 5.11) shows larger deviations. Due to the fact that this argument also holds for other kinematic distributions at truth level, the ALPGEN sample with the dynamic scale shows better agreement to the NLO prediction of POWHEL. However, differences

between the former and the latter are observed in the $t\bar{t}H$ system distributions in Figure 5.12. In the $t\bar{t}H$ distributions, the same differences between ALPGEN and POWHEL are observed as for the PYTHIA and POWHEL comparison in Section 5.4. ALPGEN predicts a harder $t\bar{t}H$ p_{T} distribution and a more central η distribution. Since the same trends between ALPGEN and POWHEL remain in the $t\bar{t}H$-system kinematics independent of the scale choice in the ALPGEN sample, the differences are effects driven by the change in the models from LO to NLO QCD accuracy as explained in Section 5.4.

5.7. Spin correlation studies

The inclusion of spin correlation effects in the model of the production and decay of the $t\bar{t}H$ process is investigated since it reflects the underlying physics. As described in Section 2.3.3, the ATLAS experiment provided the observation of non-vanishing spin correlation effects in the top-quark pair production [97]. Different MC generators, such as ALPGEN and MADGRAPH at LO and aMC@NLO and SHERPA at NLO QCD accuracy, respectively, include spin correlation effects either internally in the ME calculations or via post-processing the ME partons with external programs. For the latter case MADSPIN is used as described in Section 5.1.

5.7.1. Spin correlation effects in ALPGEN

To study the impact of the inclusion of spin correlations for the $t\bar{t}H$ process, the predictions of ALPGEN are ascertained. Both ALPGEN samples at 7 TeV and the settings that are described in Section 5.6.2 are used. For variables that are sensitive to spin correlations such as $\Delta\phi$ and $\cos\phi$ an ℓ+jets event selection on truth level excluding the W boson decay into τ leptons is applied to the ALPGEN samples. Both the ALPGEN sample with the static and with the dynamic scale is investigated. No significant differences between the former and the latter are observed with regard to the inclusion of spin correlation effects. The ALPGEN sample with the dynamic scale is presented since it shows better agreement with the NLO predictions of POWHEL as observed in Section 5.6.2. The comparison of kinematic distributions between PYTHIA 6, ALPGEN and POWHEL shows that ALPGEN shows better agreement to POWHEL than PYTHIA 6 to POWHEL (see Figure D.1 in Appendix D.1). For the p_{T} and η distribution of the $t\bar{t}H$-system appreciable differences occur between the LO predictions and POWHEL as explained in Section 5.4.1. However, ALPGEN shows no appreciable differences in variables that are not sensitive to spin correlation effects.
This picture changes when investigating variables that are sensitive to spin correlations. Figure 5.13 shows two different variables that are sensitive to spin correlation effects. Both are defined in Section 2.3.3. The first two rows of Figure 5.13 depict the $\Delta\phi$ distributions. The ATLAS analysis in Ref. [97] used the difference in ϕ between the two charged leptons of the $t\bar{t}$ decay to measure the spin correlation degree in the dileptonic channel (see also Section 2.3.3). However, the presented $\Delta\phi$ is defined as the difference of the angle between the down-type quark originating from the top quark that decays hadronically and the charged lepton of the leptonically decaying top quark

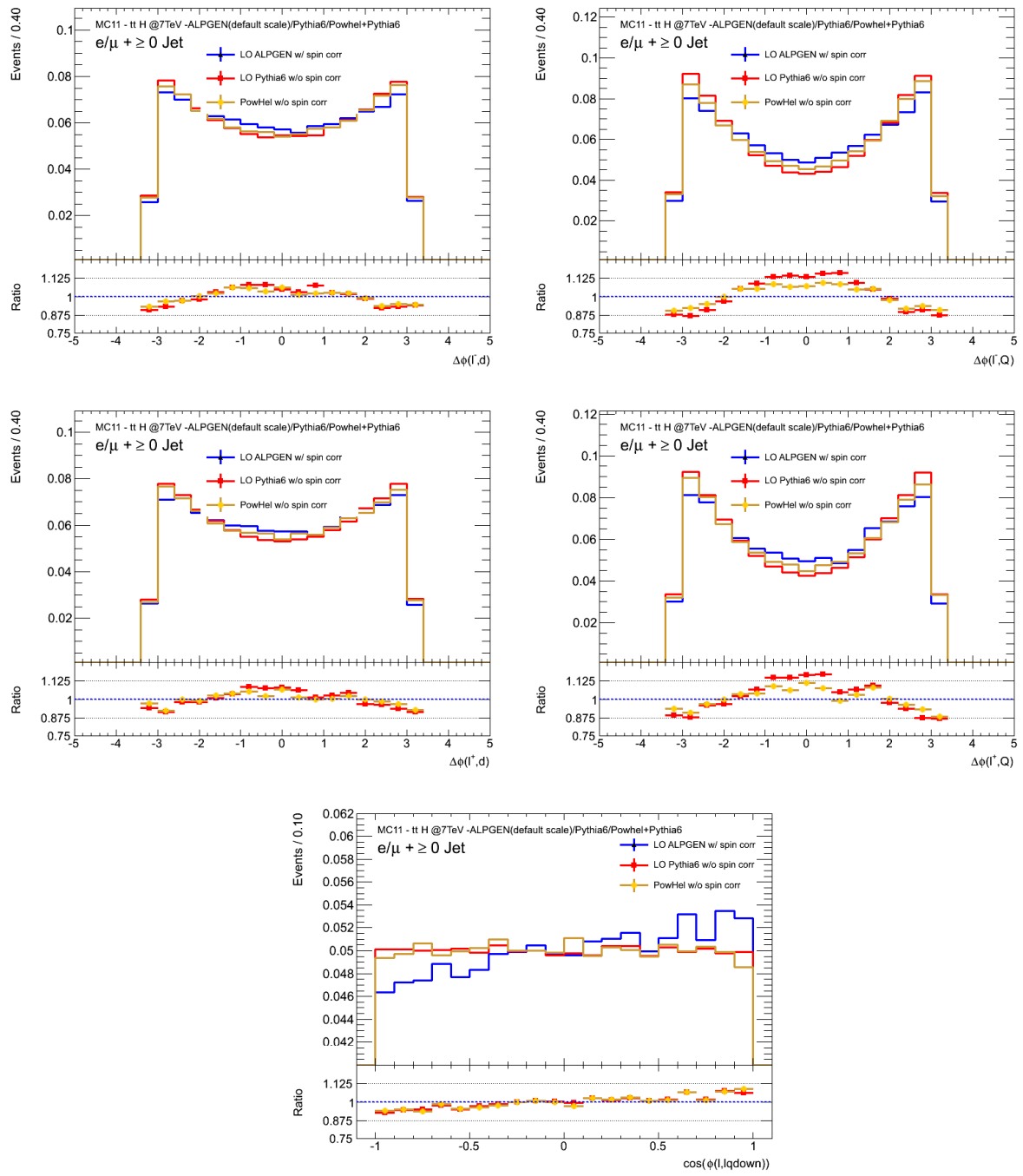

Fig. 5.13.: ALPGEN including spin correlation effects (blue) compared to PYTHIA 6 (red) and POWHEL (yellow) both not modelling spin correlations for the $\Delta\phi$ and $\cos\phi$ distributions that are normalised to unity.

in the ℓ+jets channel. The first (second) row in Figure 5.13 shows the $\Delta\phi$ distribution between the negatively (positively) charged lepton and either the $\bar{d}$-quark (d-quark) or the down-type quark including both the $\bar{d}$- and the $\bar{s}$-quark (d-quark and the s-quark). The distribution on the third row shows the $\cos\phi$ distribution where ϕ is defined as the

angle between the direction of flight of the positively charged lepton or down-type jet in the top-quark rest frame and the direction of flight of the negatively charged lepton or down-type jet in the anti-top-quark rest frame. The red and the yellow histograms reflect the LO and NLO order predictions for PYTHIA and POWHEL without spin correlations, respectively. The blue distribution shows the LO predictions of ALPGEN including spin correlation effects. For both variables, $\Delta\phi$ and $\cos\phi$, differences with respect to the inclusion of spin correlations are observed. The ALPGEN sample shows more entries for values around $\Delta\phi \approx 0$ and less towards $\pm\pi$. Whereas the predictions at LO and NLO without spin correlation shows a flat $\cos\phi$ distribution, the distribution relying on the ALPGEN predictions is distorted and shows a slope. However, the kinematic distributions, other than $\Delta\phi$ and $\cos\phi$ are not affected by spin correlation effects. Since kinematic differences in variables that are sensitive to spin correlations are minor at truth level and are not used as discriminating variables in the $t\bar{t}H$ analysis, the effect of spin correlations is negligible in the analysis.

5.7.2. Spin correlation effects in aMC@NLO

In Ref. [181] for the $t\bar{t}H$ process it is concluded that the effect of spin correlations is more important than the description of the process at NLO QCD accuracy. Nevertheless, according to the authors a modelling scheme including both spin correlation effects and QCD corrections is preferred. The studies are based on the NLO prediction by aMC@NLO at 8 TeV using the MSTW2008(n)lo68cl PDF set [201], $m_H = 125$ GeV, $\mu_0 = \mu_R = \mu_F = (m_T^t m_T^{\bar{t}} m_T^H)^{1/3}$ and no cuts. For the inclusion of spin correlation effects,

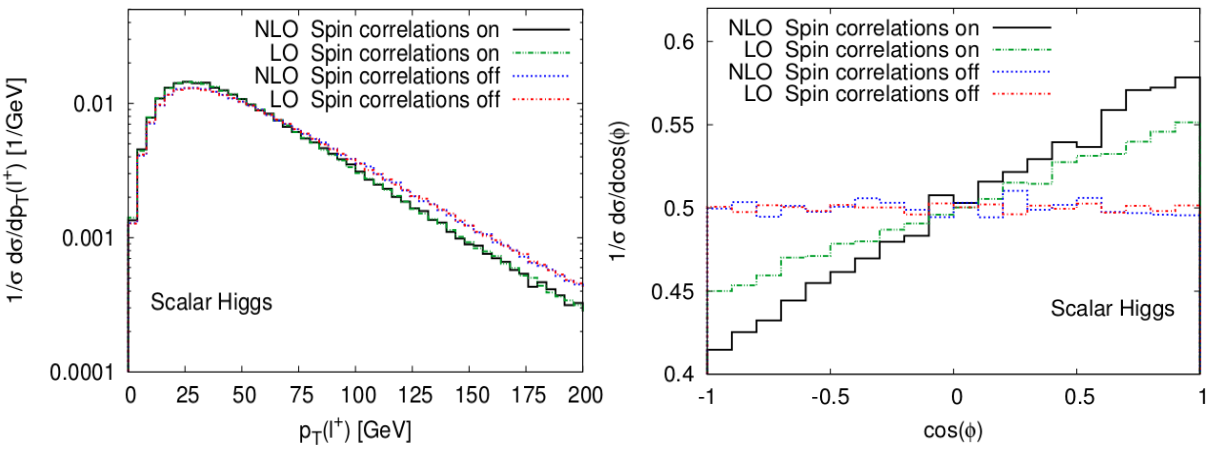

Fig. 5.14.: The LO and NLO predictions of aMC@NLO for the $t\bar{t}H$ process with and without taking spin correlation effects into account. The left plot shows the charged lepton p_T and the right plot the $\cos\phi$ distribution [181].

the aMC@NLO events are post-processed by MADSPIN before they are interfaced to HERWIG for the shower treatment. In the case of absence of the spin correlation effects, the aMC@NLO events are directly interfaced to HERWIG. Figure 5.14 shows the p_T

distribution of the hardest charged lepton and the $\cos\phi$ distribution for the $t\bar{t}H$ process at LO and NLO with and without the inclusion of spin correlation effects. The latter distribution is flat for the case of no spin correlations and is distorted when taking spin correlations into account for both the LO (dashed green) and the NLO prediction (solid black). The same effect is observed for the inclusion of spin correlations at LO in ALPGEN (see Section 5.7.1). Figure 5.14b illustrates the impact on the charged lepton p_{T} distribution when including spin correlation effects. The impact is milder except for the high momentum region ($p_{\mathrm{T}} \gtrsim 100$ GeV). This implies that the shape of the charged lepton p_{T} is more affected by the inclusion of spin correlations than NLO corrections. In the case of the $\cos\phi$ distribution, both the inclusion of NLO QCD accuracy calculations and spin correlation effects is necessary [181].

5.7.3. Charged lepton p_{T} in ALPGEN and aMC@NLO

In Section 5.7.1, the spin correlation effects predicted at LO by ALPGEN in sensitive variables are demonstrated and compared to NLO predictions by POWHEL without spin correlations. A distortion similar to the one by aMC@NLO in Section 5.7.2 is observed in the $\cos\phi$ distribution with respect to the cases of including (ALPGEN) or excluding (POWHEL) the effect of spin correlations. However, comparing the predictions for the positively charged lepton p_{T} distribution as illustrated in Figure 5.15, differences between the predictions of ALPGEN and aMC@NLO with respect to the effect of spin correlations are observed. The lepton p_{T} distribution in Figure 5.15b shows no appreciable differences between the ALPGEN LO prediction with spin correlations (blue distributions) and the NLO predictions without spin correlations (red distribution) by POWHEL. In Figure 5.15a clear differences are observed between the case of including

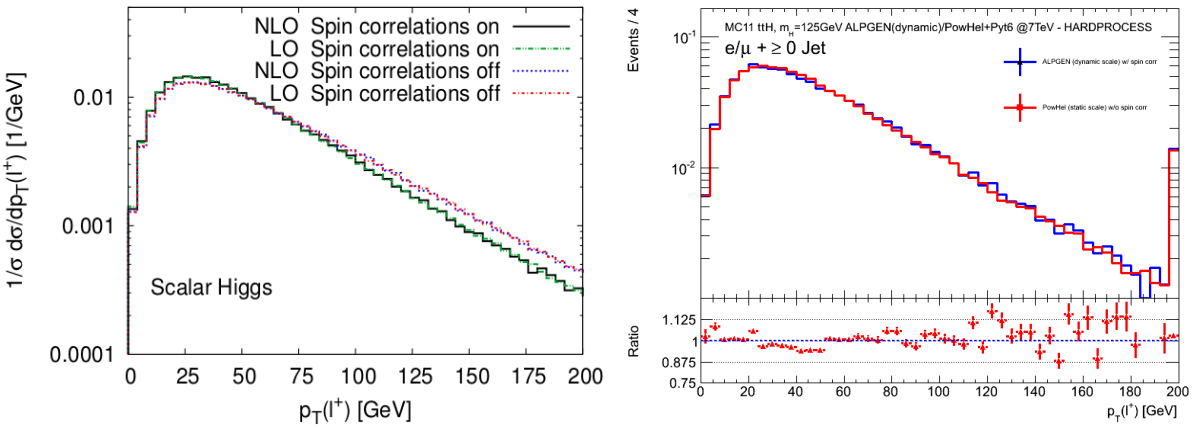

(a) *(b)*

Fig. 5.15.: The charged lepton p_{T} distribution. The LO and NLO predictions of aMC@NLO for the $t\bar{t}H$ process with and without taking spin correlation effects into account (a). The LO prediction of ALPGEN with spin correlations and the NLO prediction of POWHEL without spin correlations (b).

and excluding spin correlations in the p_{T} spectrum almost independent of the LO or NLO prediction in aMC@NLO. The differences between the two plots do not arise from the different PDF sets, scales and center-of-mass energies that are used to generate the samples. Differences with respect to spin correlations are only expected in distributions of variables including two particles. Hence, no difference is expected for the lepton p_{T} distribution. In consultation with the theorists that provided the aMC@NLO comparisons in Ref. [181], it is found that the legend in the plot shown in Figure 5.15a is misleading. It should refer to turning on/off the spin transmission from the top quarks to their decay products. This means, instead of including or excluding spin correlations, the subsequent W decay does or does not contain implicit W helicity information from the parent top quarks (see Section 2.3.3). The latter is known to have an impact on the charged lepton p_{T} distribution as shown in Section 2.3.3. The CDF experiment used this specific distribution to measure the W polarisation in the top-quark decay [85]. The distribution in Figure 5.15b shows the expected dependence on spin correlation effects. It is concluded that no difference is expected when spin correlations are turned on (ALPGEN) or turned off (POWHEL) whenever PYTHIA, that is used to shower the POWHEL sample, handles the top-quark decay correctly.

5.8. POWHEL dependence on the choice of the PDF set

Based on the reweighting studies, POWHEL samples with $m_H = 125$ GeV are produced to run through the full ATLAS production chain. Whereas these samples are generated

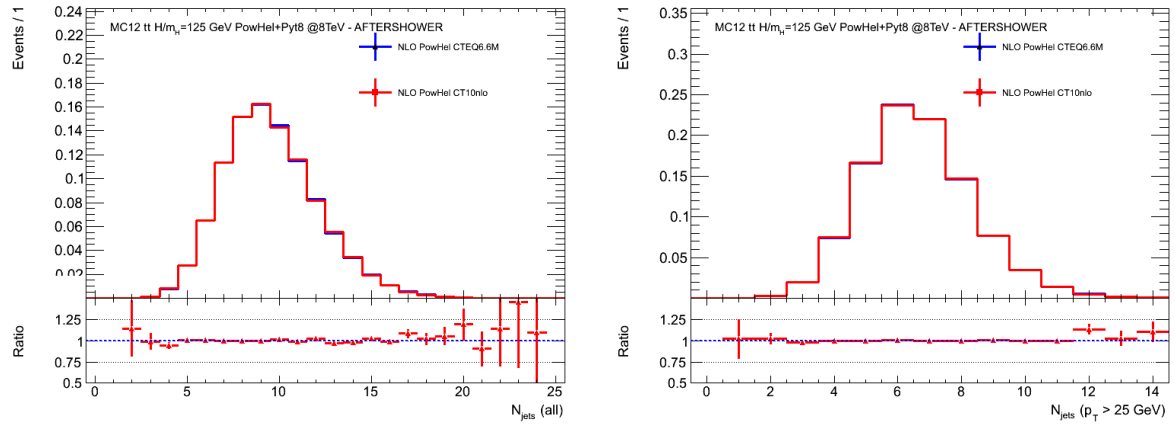

(a) ***(b)***

Fig. 5.16.: The number of jets before (a) and after (b) applying jet cuts ($p_{\mathrm{T}} > 25$ GeV and $|\eta| < 2.5$) at 8 TeV.

using the CT10nlo PDF set [49] which is the ATLAS default NLO PDF set, the POWHEL samples used for the reweighting procedure are generated with the CTEQ6.6M PDF set. Hence, two sets of POWHEL samples using the static scale are compared. The validation of the new samples after showering with PYTHIA is relevant to investigate the differences that arise by changing to a newer PDF set. At 7 TeV and 8 TeV, no

appreciable differences that exceed differences which can be explained by statistical fluctuations occur in basic kinematic distributions such as top, anti-top, Higgs and $t\bar{t}H$ p_{T} and η. A selection of the hard process particles on truth level with a jet p_{T} cut of $p_{\mathrm{T}} > 25$ GeV and $|\eta| < 2.5$ was performed. Figure 5.16 shows the jet multiplicity distributions at 8 TeV before and after applying a cut on all the jet cuts. A good agreement is observed in the jet multiplicity distribution after applying the jet cuts. The same holds for 7 TeV. For 7 TeV (8 TeV), a selection of kinematic distributions is depicted in Figure E.1 in Appendix E (Figure E.2 in Appendix E). It is concluded that the change between the two nominal PDF sets does not impact the $t\bar{t}H$ model.

5.9. POWHEL samples with different Higgs mass points

Five signal samples with different Higgs boson masses in the range $115 \leq m_H \leq 135$ GeV are produced with the same configurations as for the POWHEL sample discussed above at 7 TeV and 8 TeV. The same event selection as in Section 5.8 is applied to the different signal samples. The plot in Figure 5.17a shows the invariant mass of the Higgs in the different samples. It is worth mentioning that the higher the Higgs

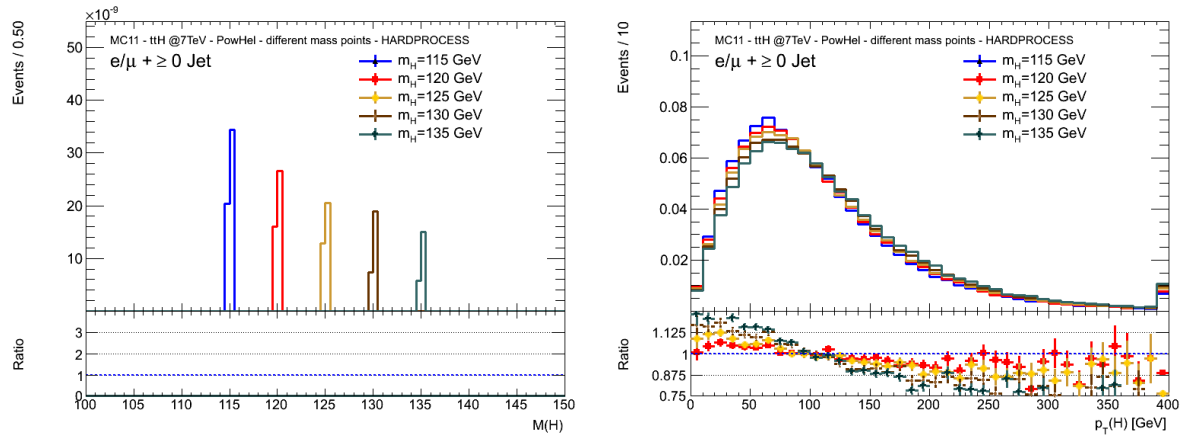

(a) *(b)*

Fig. 5.17.: The Higgs mass in the different POWHEL samples (a) that is normalised to the sample cross-section and the Higgs p_{T} spectrum (b) that is normalised to unity. The plots correspond to $\sqrt{s} = 7$ TeV.

mass, the lower the cross-section. This is due to the fact that by increasing the Higgs mass the momentum fraction x that is carried by the partons to produce a $t\bar{t}H$ event increases as well. For higher values of x, the probability of finding partons with this specific x decreases. Hence, a higher center-of-mass energy $\sqrt{s}$ is needed to produce the $t\bar{t}H$-system with a higher Higgs mass which results in a decreased cross-section. Figure 5.17b illustrates the Higgs p_{T} spectrum for the different Higgs masses. The higher the Higgs mass, the harder the Higgs p_{T} spectrum and thus the overall energy of the Higgs. The validation of the newly provided POWHEL samples in this and the former section resulted in the full ATLAS simulation of the POWHEL NLO model.

CHAPTER

SIX

SUMMARY, CONCLUSIONS AND OUTLOOK

Summary

In this thesis, $t\bar{t}H$ signal modelling and corresponding systematic uncertainty studies were performed. An overview of all MC generators that are available to generate the $t\bar{t}H$ process was outlined and thus the embedding of the presented studies in the context of the most recent MC generator developments was guaranteed. A description of matching procedures used to interface the ME calculations to PS programs was given. Those of the latter that were used in the context of this thesis were introduced and studies of the MC output to ensure the validity of the $t\bar{t}H$ signal model on parton level was ascertained. Moreover, studies on changes between different PYTHIA versions were performed forming the basis for $t\bar{t}H$ modelling studies at different orders in QCD perturbation theory at 7 TeV and 8 TeV. Reweighting procedures between LO and NLO signal predictions were developed. Higher-order corrections were estimated using renormalisation and factorisation scale variations which were applied as a systematic uncertainty to the $t\bar{t}H$ signal model. Furthermore, the scale choice in MC generators at different orders in QCD perturbation theory was investigated. Beside the evaluation of the impact of the inclusion of spin correlation effects at LO and NLO, the dependence of the NLO predictions on the choice of the PDF set was studied. In addition, the validation of additional NLO samples was performed, as a requirement towards the submission to the full ATLAS simulation.

Conclusions

NLO predictions show a weaker dependence on the factorisation and renormalisation scale than LO predictions. Hence, the theoretical uncertainty arising from the scale choice is reduced. Moreover, NLO predictions represent the theory more accurately. Significant differences occurred in the comparison of kinematic distributions between LO and NLO predictions of PYTHIA and POWHEL, respectively. As a preliminary step, the LO signal sample was reweighted to the NLO predictions using reweighting

functions. The applied reweighting procedure resulted in a more accurate $t\bar{t}H$ signal model that is henceforth used in the $t\bar{t}H$ analysis of the ATLAS experiment using the full data set at 7 TeV and 8 TeV.
The scale variations in the POWHEL model were proven to be an important source of the total theoretical uncertainty of the $t\bar{t}H$ model. The scale variations showed an effect on both the signal shape and normalisation in a variety of kinematic distributions. The residual scale dependence on the shape of the NLO signal sample is found to be at a level of up to 20%. It was shown that it is possible to reproduce the kinematics of the scale varied samples by reweighting of the default sample in certain kinematic variables both at 7 TeV and 8 TeV. Thus, a method to apply a systematic uncertainty originating from scale variations was developed and successfully applied to the $t\bar{t}H$ signal model. Kinematic distributions such as the $t\bar{t}H$-system kinematics and the number of jets that are sensitive to additional QCD radiation show a fairly stable behaviour under the scale variations. This might indicate that a simultaneous shift of the applied renormalisation and factorisation scale results in an underestimation of the actual scale uncertainty. Thus, an independent shift of the renormalisation and the factorisation scale is recommended. As a conclusion, the reweighted signal model serves as an accurate description with a relatively small theoretical uncertainty (shape uncertainty of up to 20%) originating from scale variations that are being used in the MVA techniques of the ATLAS $t\bar{t}H$ analysis.
To investigate the impact of the reweighted signal model, the kinematic variable H_T^{had} was ascertained. The study showed that in the SR topologies of the analysis at reconstruction level, the same trends are observed between the LO and NLO predictions in H_T^{had} as for $t\bar{t}H$ p_{T} at truth level. The NLO predictions result in softer p_{T} spectra in different kinematic variables that lead to the fact that less signal events pass the event selection. Hence, the event selection efficiency is decreased resulting in an overall loss of sensitivity.
Beside the scale uncertainty of the NLO signal model, possible additional sources of systematic uncertainties were investigated. The choice of the renormalisation and factorisation scale was studied first for the NLO $t\bar{t}H$ model by POWHEL and second for a LO $t\bar{t}H$ model by ALPGEN.
A good agreement between the POWHEL sample with the static and with the dynamic scale is observed for a variety of kinematic distributions at truth level. The predictions of the sample that was generated with the dynamic scale were covered by the systematic uncertainty originating from the scale variations of the sample with the static scale. However, significant differences were observed for the p_{T} and η distribution of the $t\bar{t}H$-system. This effect is explained by the structure of the chosen scale. An additional systematic uncertainty originating from the choice of the scale is thus recommended to be applied to the $t\bar{t}H$ signal model.
For the LO predictions of ALPGEN more significant differences between the samples with the static and the dynamic scale were observed. This is understood in terms of the high dependence of LO predictions on the choice of the scale. The ALPGEN sample with the dynamic scale is in a better agreement to the POWHEL model than the ALPGEN sample with the static scale. This conclusion holds for all investigated kinematic distributions but the $t\bar{t}H$-system kinematics p_{T} and η which are known to be sensitive to the

differences of predictions at LO and NLO.
Generating signal predictions with more than one additional QCD radiation (as implemented in POWHEL) is of interest with regard to a possible additional systematic uncertainty for the signal model. ALPGEN can provide $t\bar{t}H$ predictions with up to four additional partons. However, the matching procedure for the $t\bar{t}H$ process within ALPGEN is not provided. Thus, the study of the impact of the inclusion of more than one extra parton radiation is prepared but needs to be postponed and relies on new ALPGEN releases.
The inclusion of spin correlations in the $t\bar{t}H$ model was investigated in ALPGEN. Variables that are sensitive to spin correlations such as $\Delta\phi$ and $\cos\phi$ show differences with respect to the LO prediction of PYTHIA and the NLO prediction of POWHEL. However, the ALPGEN predictions are covered by the systematic scale uncertainty applied to the predictions of POWHEL in all other kinematic distributions that were studied. It is concluded that although differences in sensitive variables are observed at truth level, the effects of spin correlations are negligible for the $t\bar{t}H$ analysis. Hence, no additional systematic uncertainty needs to be applied due to spin correlation effects. It was additionally shown that the latter have no effect on the charged lepton p_{T} distribution.
As pointed out, the reweighted signal sample was only the short-term plan. Based on the presented studies, the POWHEL samples were validated with newer PDF sets that are the default ATLAS PDF sets at NLO and ran through the full ATLAS simulation. It was confirmed that no significant changes between the samples with different PDF sets occurred. Furthermore, samples with varying Higgs masses were generated and the resulting impact on different kinematic distributions on truth level was studied. The changes in the kinematic distributions were explained and are well understood.
The presented studies formed the basis for a $t\bar{t}H$ signal model at NLO QCD accuracy and the full production and processing of the POWHEL signal samples within the full ATLAS simulation. POWHEL was tested with a variety of different parameters and generation settings. Moreover, its predictions are proven to be stable with regard to the predictions and additional features of investigated LO generators. POWHEL appears to model the $t\bar{t}H$ process with high theoretical accuracy. Thus, the applied MVA methods of the $t\bar{t}H$ analysis can rely on a persuasive $t\bar{t}H$ signal model resulting in a better separation between background and signal events.

Outlook

The automation of NLO predictions and their matching to PS programs is a rather modern development and opens the window to highly accurate theoretical predictions. Beside the investigation of the predictions provided by POWHEL, first efforts were started to investigate the theoretical predictions of aMC@NLO and SHERPA for the $t\bar{t}H$ process at truth level. It became obvious that the generation of events for both of the latter is time consuming and an optimisation with regard to the use of multicore processors or computer clusters is necessary. The investigation of other NLO predictions than those of POWHEL is important to additionally validate its predictions and to compare different NLO matching schemes. However, in Ref. [204] the theoretical

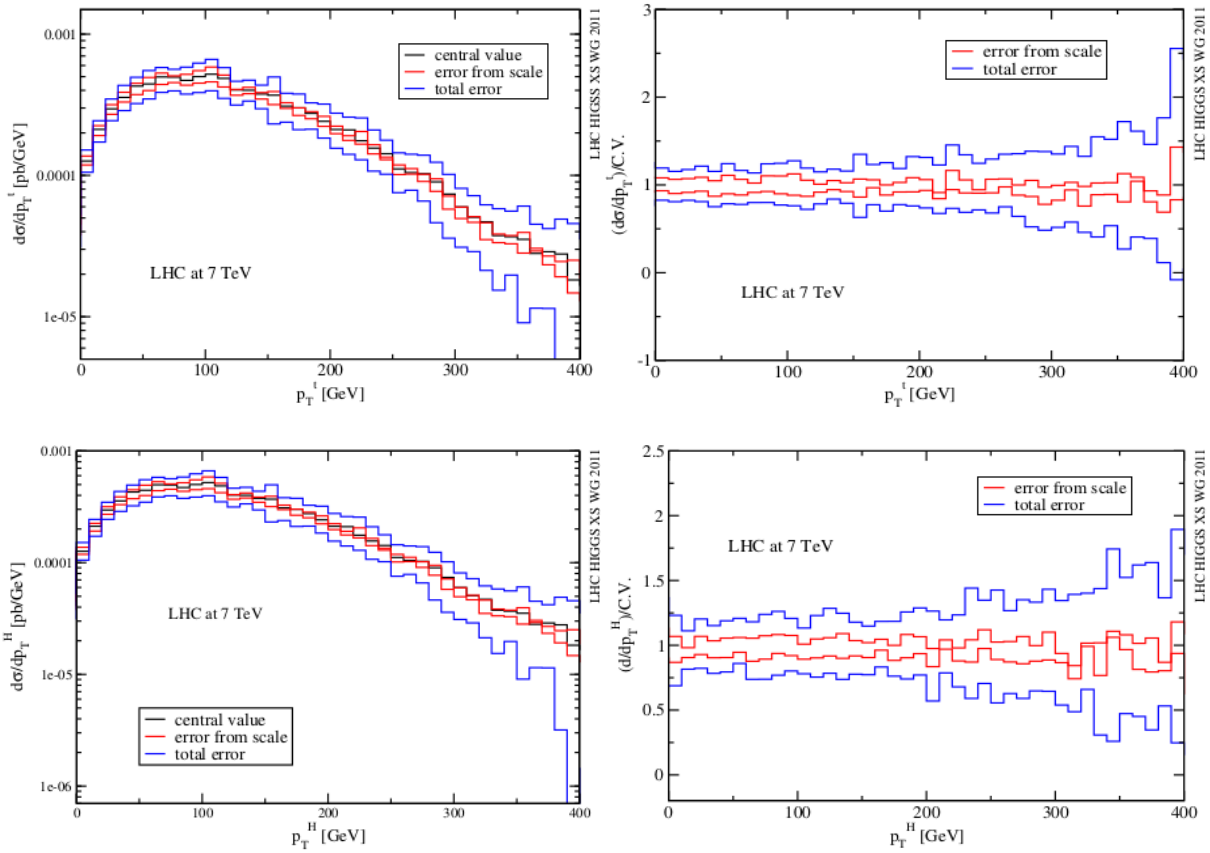

Fig. 6.1.: The top and Higgs p_{T} distributions at NLO QCD accuracy including the theoretical uncertainties originating from both the scale dependence and the α_S+PDF uncertainty. The left plots show the actual distributions whereas the right plots show the spread with respect to the nominal distribution in per cent [204].

error on NLO QCD distributions for the $t\bar{t}H$ process at 7 TeV was investigated before passing the NLO calculations to any PS program. To assess a systematic uncertainty on the prediction originating from the choice of the renormalisation and factoristion scale, the nominal scale was varied by a factor of 2. The nominal scale was the same static scale as used for the presented studies in this thesis. In addition to the scale uncertainty, the impact of the α_S and PDF uncertainty was studied. The latter uncertainty was obtained by different PDF choices within the CTEQ6.6 PDF set. The plots on the left hand side in Figure 6.1 show the Higgs and top p_{T} distributions and the plots on the right hand side depict the spread around the nominal value in per cent, respectively. The black histograms represent the distribution with the nominal scale $\mu_0 = \mu_F = \mu_R$. The red histograms illustrate the distributions with up- and down-varied scales (factor 2) and the upper and lower blue histograms reflect the total errorband including the uncertainties from the choice of α_S and PDFs as well. The latter uncertainties were obtained consistently within the CTEQ6.6 PDF set and combined in quadrature before adding the result linearly to the theoretical uncertainty from the scale dependence bin by bin. It is found that in regions that are not dominated by statistical fluctuations that

the systematic error of the scale ranges between 10% and 20%. The total error ranges between 20% and 50%.
However, it is suggested to perform such studies including the interface of the NLO calculations to PS programs as it was done in this thesis. A comparison when interfacing

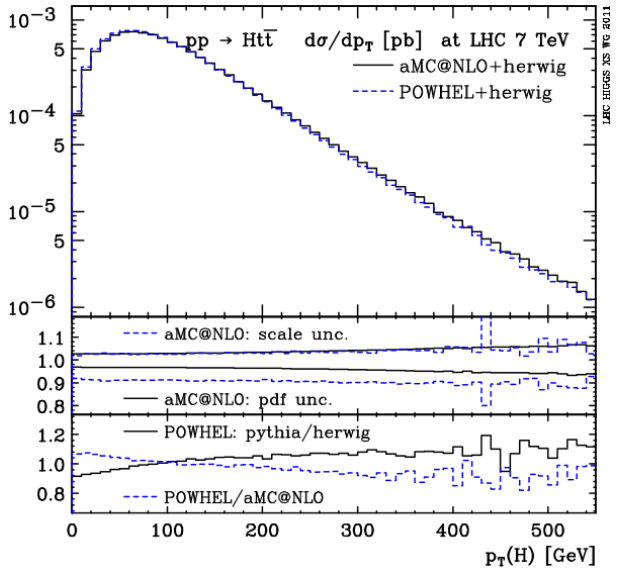

Fig. 6.2.: The Higgs p_{T} distribution without applying any cuts. The upper ratio plot reflects both the uncertainty originating from the choice of PDFs (solid) and scales (dashed) computed by aMC@NLO which was interfaced to HERWIG. The lower ratio depicts POWHEL over aMC@NLO (dashed) and the results computed by interfacing POWHEL to PYTHIA and HERWIG [204].

the NLO predictions of aMC@NLO and POWHEL to PYTHIA and HERWIG using the different NLO matching schemes was ascertained. It was shown that the differences between POWHEL and aMC@NLO interfaced to HERWIG and POWHEL interfaced to PYTHIA are in general below 10% in regions that are not dominated by PSs in different kinematic distributions. Figure 6.2 illustrates that POWHEL plus HERWIG (blue dashed) shows a slightly softer Higgs p_{T} distribution than aMC@NLO interfaced to HERWIG (solid black). This argument holds also for other kinematic distributions with respect to the other two setups. The results were obtained in an accord between the theorists of the NLO MC generators to guarantee a global and common setup of event generation enabling a reliable comparison. Hence, it can be concluded that the different NLO predictions show a good agreement and that interfacing the ME calculations to different PS programs using different NLO matching schemes does not result in appreciable distortions.
However, the studies in Ref. [204] suggest that different systematic uncertainties need to be added to the present $t\bar{t}H$ signal model that was investigated in this thesis. First, the α_S+PDF uncertainty needs to be added. The information that is needed to assess the latter is provided within the $t\bar{t}H$ signal samples that ran through the full ATLAS simulation. Moreover, the difference between interfacing POWHEL to PYTHIA or to HERWIG needs to be studied as a possible additional systematic uncertainty, although it

appears to have a minor effect on the overall systematic uncertainty of the $t\bar{t}H$ model. The usage of different PS programs such as PYTHIA and HERWIG reflects an estimate for the two different hadronisation models that are implemented in PYTHIA which uses the Lund string model and HERWIG which uses a cluster model. In addition, a possible systematic uncertainty arising from the UEs including MPIs, the hadronisation of the beam-remnants and the hadron decays needs to be investigated. This can be done by switching between different PS tunes. Also the impact of color reconnection and Pile-Up effects on the $t\bar{t}H$ signal model need to be studied and possibly applied as an additional source of systematic uncertainty in the future.

APPENDIX

A

LO TO NLO SIGNAL REWEIGHTING

A.1. Signal reweighting at 7 TeV

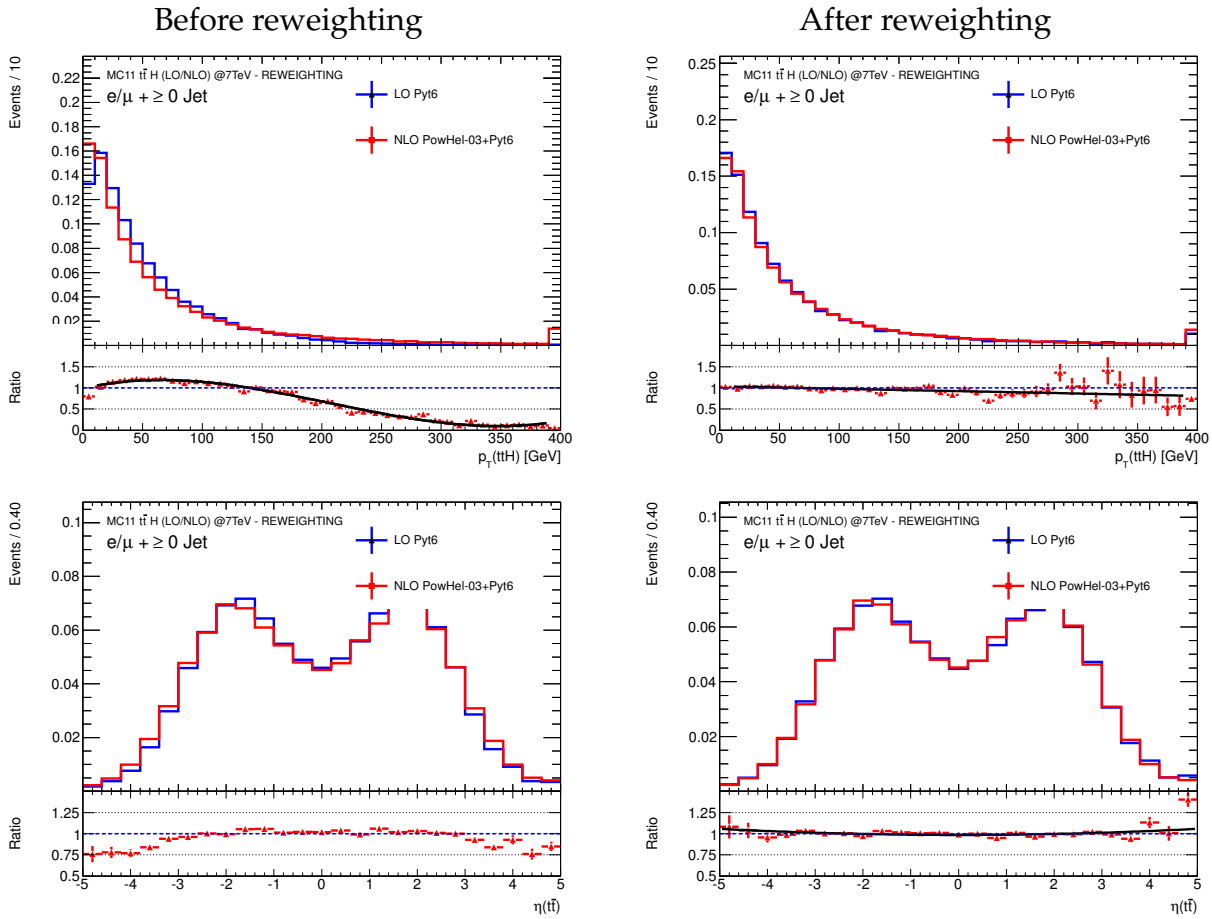

Fig. A.1.: The effect of applying the reweighting procedure on different kinematic distributions at 7 TeV: $t\bar{t}H$ p_{T} and $t\bar{t}$ η. The samples are normalised to unity.

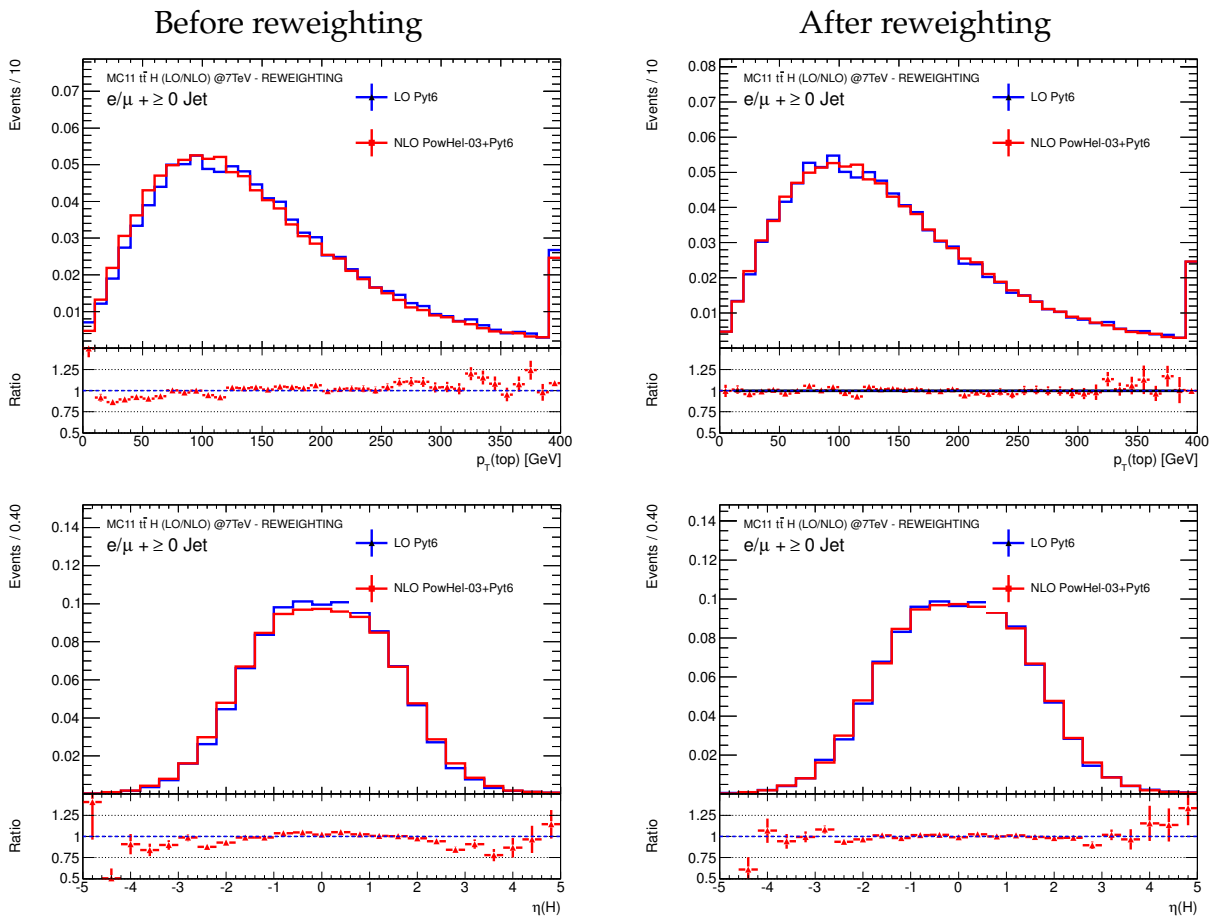

Fig. A.2.: The effect of applying the reweighting procedure on different kinematic distributions at 7 TeV: top p_{T} and Higgs η. The samples are normalised to unity.

A.1.1. Reweighting functions for 7 TeV

The functions and ratios do not contain statistical uncertainties. They are assumed to be small negligible.
The reweighting function for the $t\bar{t}H$ p_{T} distribution:

```
// ttH pT reweighting using normalised histo
double Select::getWeightTTH_PT(double pt) const {

  //polynomial fit p0+p1*x+p2*x*x+p3*x*x*x

  double p0 = 9.83814e-01;
  double p1 = 6.60200e-03;
  double p2 = -5.98909e-05;
  double p3 = 9.65732e-08;
```

```
  double weight = 1;
  //1st bin
  if ( pt > 0 && pt <= 10 ) weight =  0.800689;
  //overflow bin
  else  if ( pt > 390 ) weight = 0.0489442;
  else{
    weight = p0+p1*pt+p2*pt*pt+p3*pow(pt,3);
  }

  return weight;

}
```

The reweighting function for $t\bar{t}$ η:

```
// ttbar eta reweighting using normalised histo
double Select::getWeightTTBAR_ETA(double eta) const {


 //polynomial fit p0+p1*x+p2*x*x

  double p0 = 1.07064e+00;
  double p1 = 3.51869e-03;
  double p2 = -1.68147e-02;

  double weight =1;
  weight = p0+p1*eta+p2*eta*eta;

  return weight;

}
```

The reweighting function for top p_{T}:

```
// top pT reweighting using normalised histo
double Select::getWeightTOP_PT(double pt) const {

  //linear fit p0+p1*x

  double p0 = 8.54176e-01;
  double p1 = 8.99025e-04;


  double weight =1;
  if ( pt > 0 && pt <= 10 ) weight =  1.48238;
```

```
  else if ( pt > 390 ) weight = 1.53501;
  else{
    weight = p0+p1*pt;
  }

 return weight;

}
```

A.2. Signal reweighting at 8 TeV

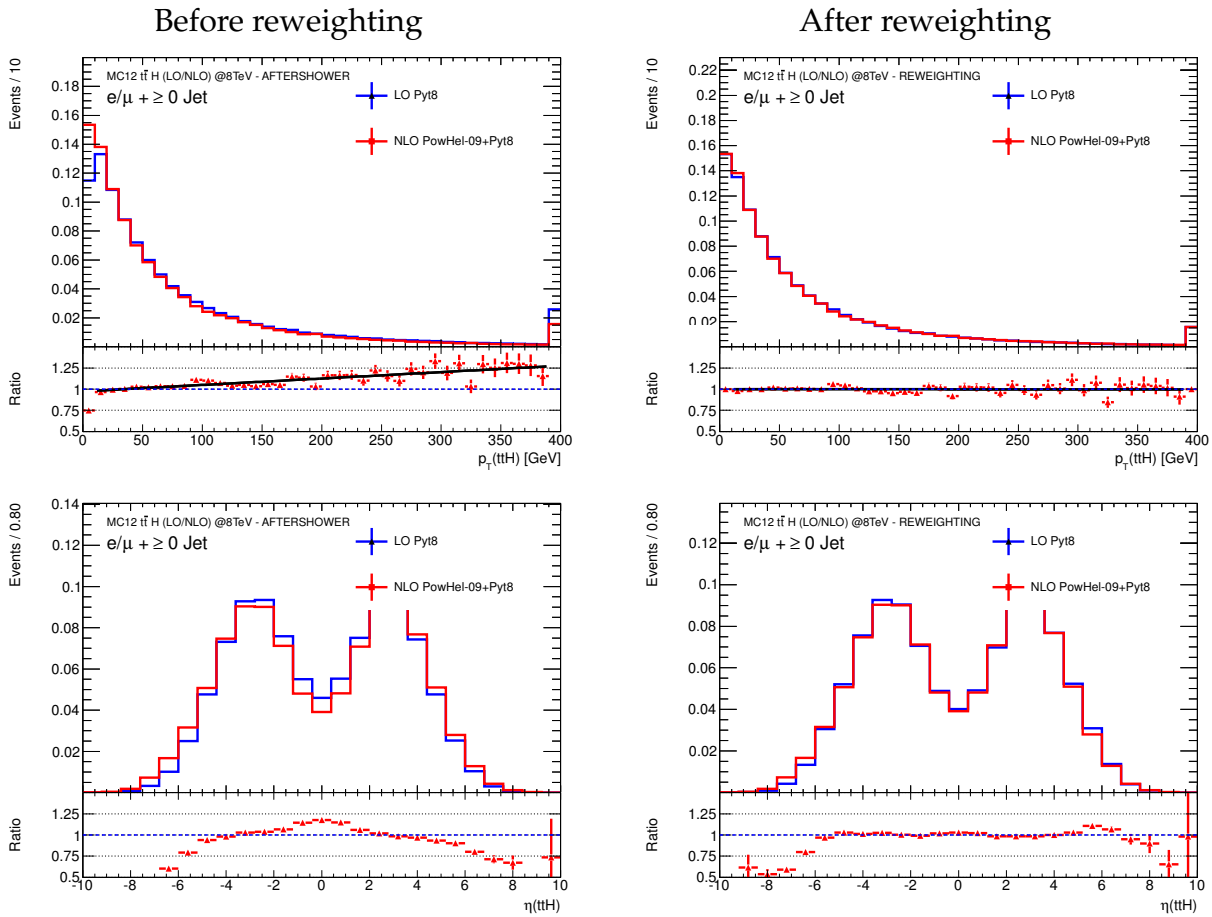

Fig. A.3.: The effect of applying the reweighting procedure on different kinematic distributions at 8 TeV: $t\bar{t}H$ p_{T} and $t\bar{t}H$ η. The samples are normalised to unity.

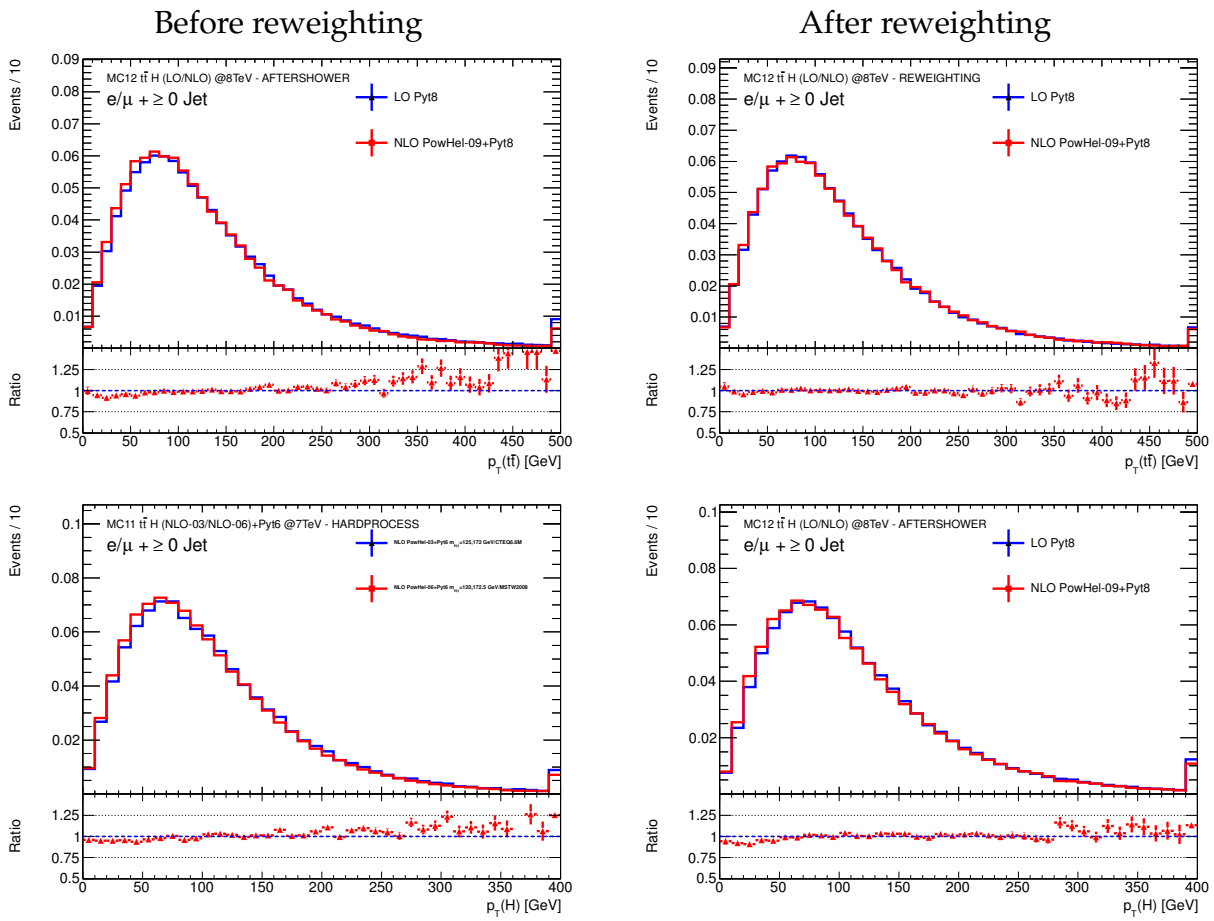

Fig. A.4.: The effect of applying the reweighting procedure on different kinematic distributions at 8 TeV: $t\bar{t}$ p_{T} and Higgs p_{T}. The samples are normalised to unity.

A.2.1. Reweighting function for 8 TeV

The statistical errors of the fit are assumed to be negligable.
The reweighting function for $t\bar{t}H$ p_{T}:

```
// ttH pT reweighting using normalised histo
double Select::getWeightTTH_PT(double pt) const {

  //linear ratio fit m*pt+b
  double m = 0.000756909;
  double b = 0.973904;

  double weight =1;
  //1st bin
  if ( pt > 0 && pt <= 10 ) weight = 0.748969;
  //overflow bin
  else if ( pt > 390 ) weight = 1.63696;
  //linear fit
```

```
  else{
    weight = m*pt+b;
  }

  return weight;

}
```

APPENDIX

B

SCALE VARIATION STUDIES

B.1. Scale variation studies at 7 TeV – reweighting

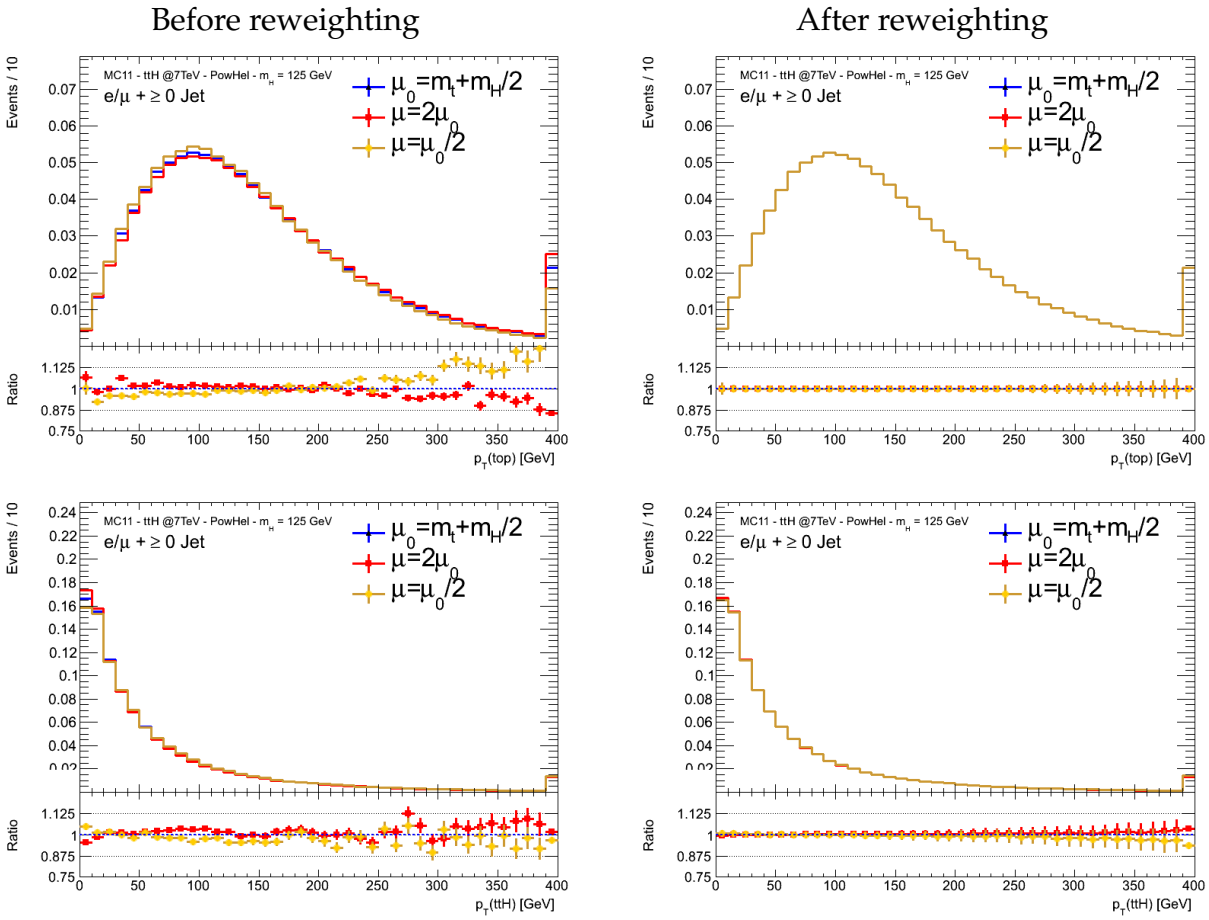

Fig. B.1.: The effect of applying the reweighting procedure for top and $t\bar{t}H$ p_{T} on different kinematic distributions at 7 TeV in the zero jet inclusive channel: top p_{T} and $t\bar{t}H$ p_{T}. The samples are normalised to unity.

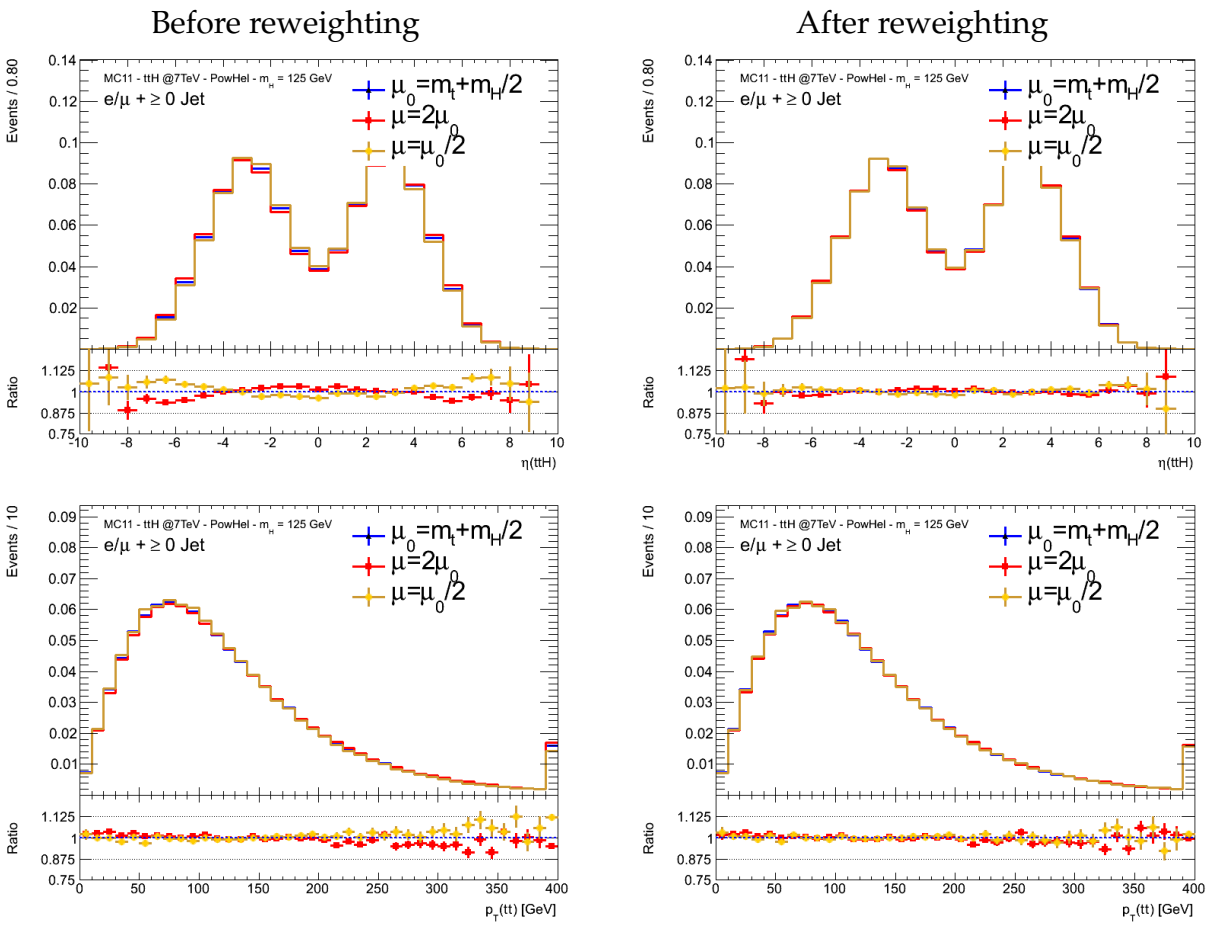

Fig. B.2.: The effect of applying the reweighting procedure for top and $t\bar{t}H$ p_{T} on different kinematic distributions at 7 TeV in the zero jet inclusive channel: $t\bar{t}H$ η and $t\bar{t}$ p_{T}. The samples are normalised to unity.

B.2. Scale variation studies at 8 TeV – reweighting

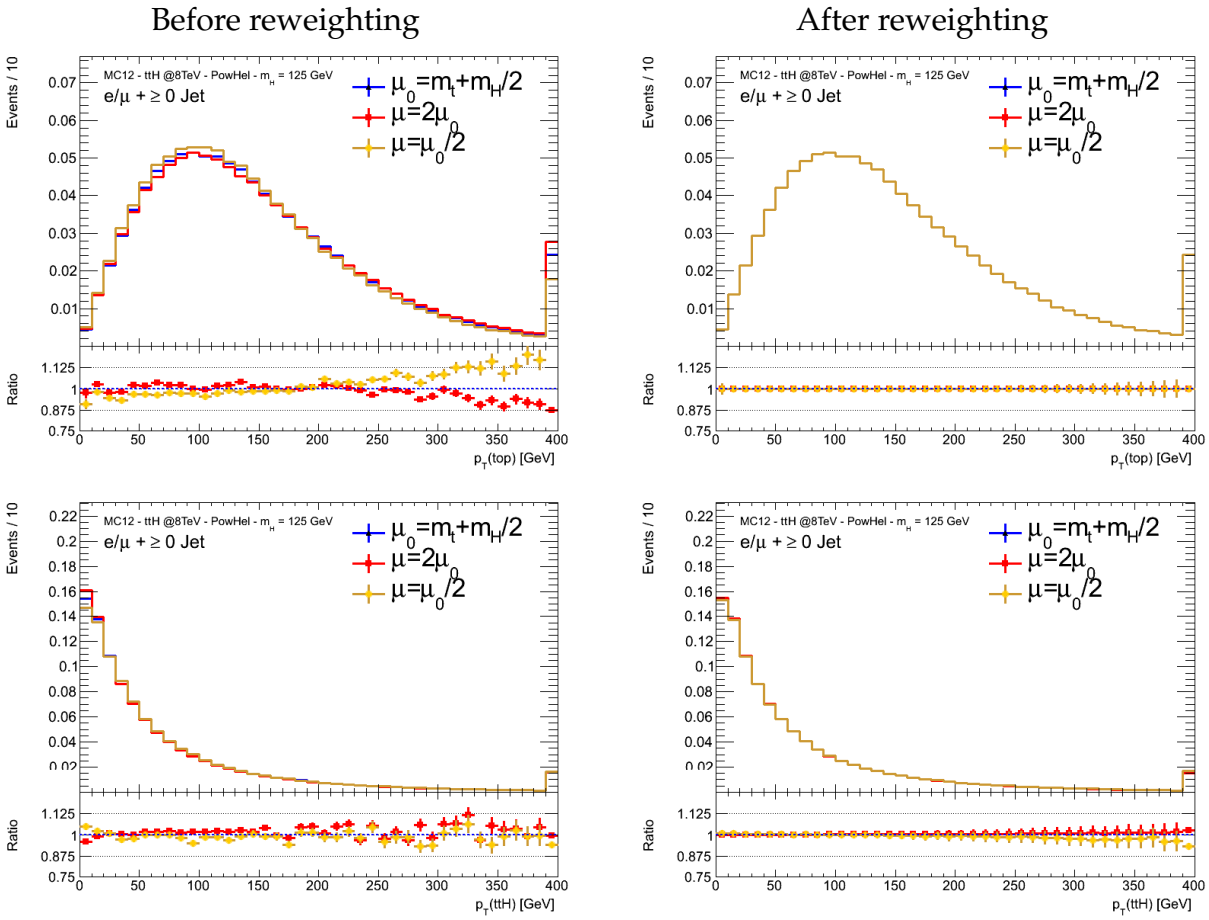

Fig. B.3.: The effect of applying the reweighting procedure for top and $t\bar{t}H$ p_{T} on different kinematic distributions at 8 TeV in the zero jet inclusive channel: top p_{T} and $t\bar{t}H$ p_{T}. The samples are normalised to unity.

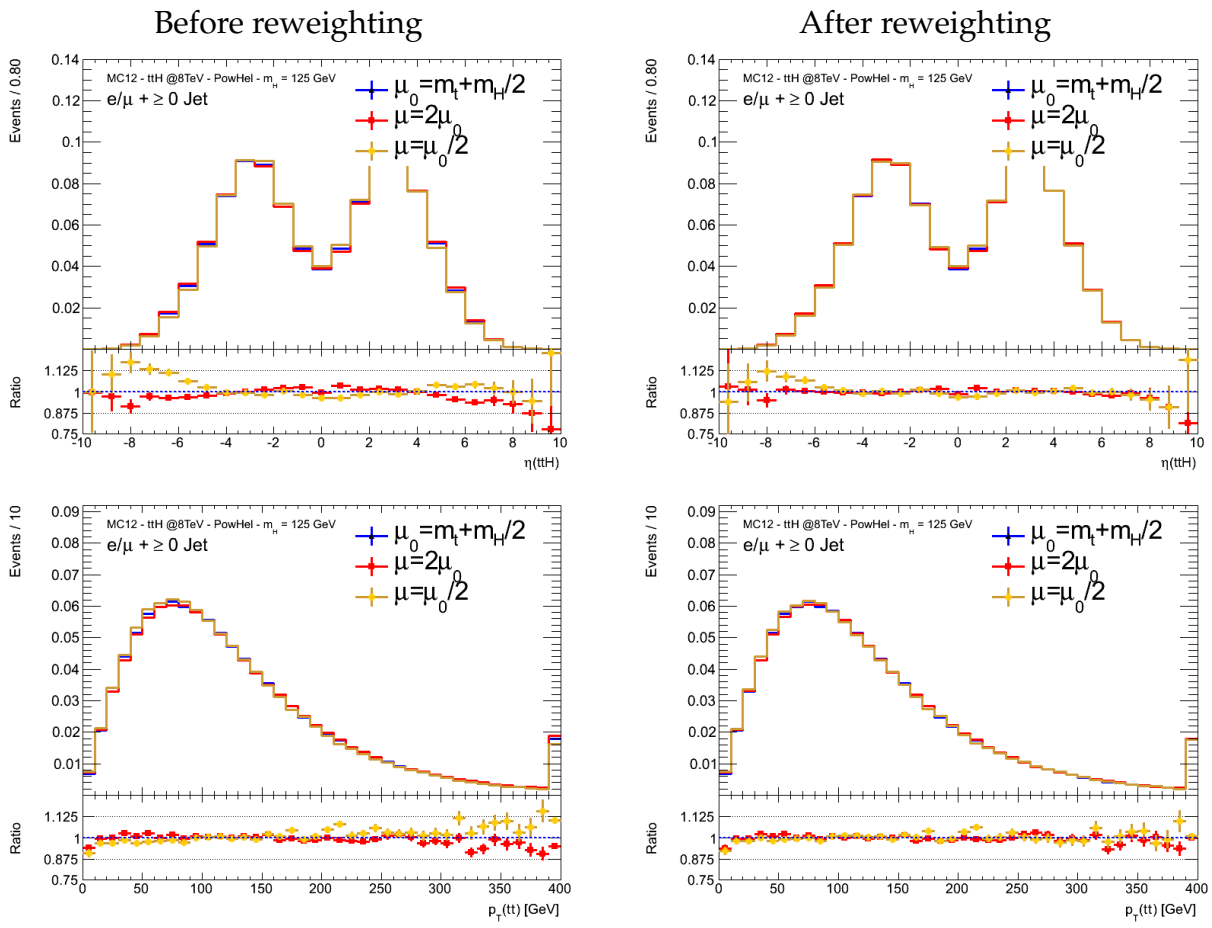

Fig. B.4.: The effect of applying the reweighting procedure for top and $t\bar{t}H$ p_{T} on different kinematic distributions at 8 TeV in the zero jet inclusive channel: $t\bar{t}H$ η and $t\bar{t}$ p_{T}. The samples are normalised to unity.

APPENDIX

C

CHOICE OF THE SCALE IN POWHEL

C.1. Studies on the choice of the scale in POWHEL at 8 TeV

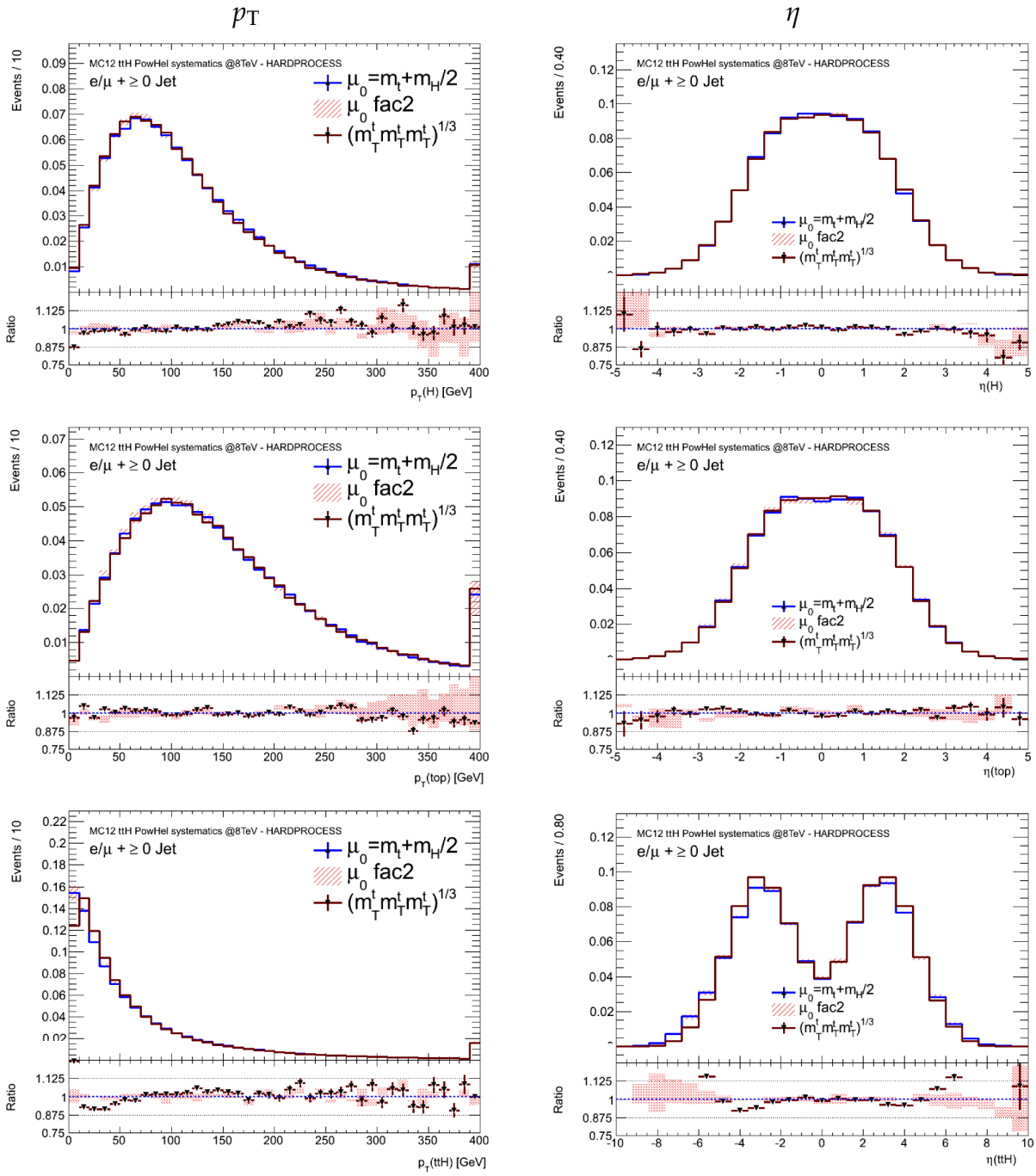

Fig. C.1.: The p_T and η distribution for the Higgs, the top quark and the $t\bar{t}H$-system in the zero jet inclusive channel normalised to unity at 8 TeV.

APPENDIX

D

LO AND NLO SPIN CORRELATION PREDICTIONS

D.1. Comparison of PYTHIA 6, ALPGEN and POWHEL

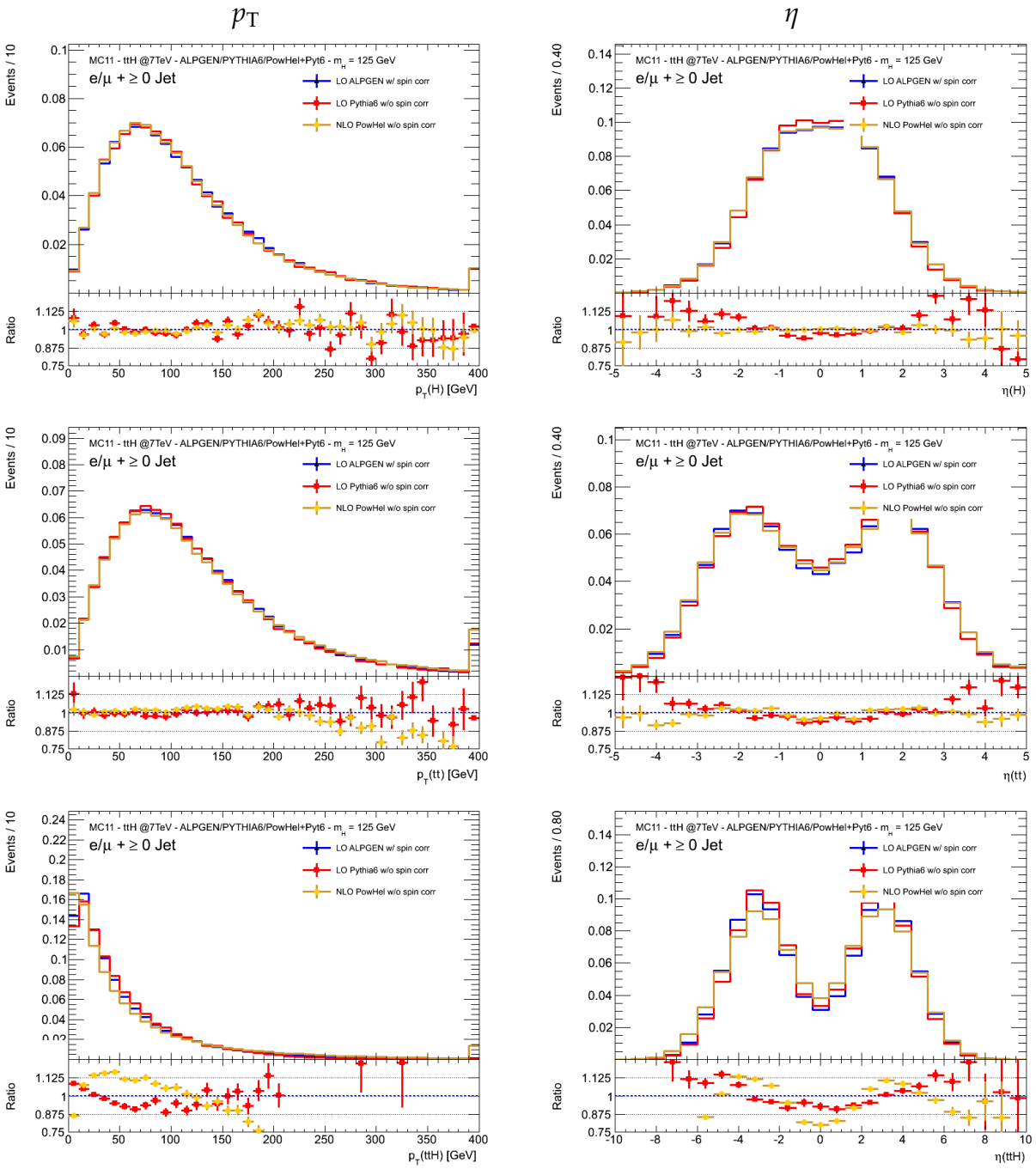

Fig. D.1.: The p_T and $|\eta|$ distribution for the Higgs, $t\bar{t}$- and the $t\bar{t}H$-system in the zero jet inclusive channel normalised to unity at 7 TeV.

APPENDIX

E

THE PDF SET DEPENDENCE OF THE POWHEL SAMPLES

E.1. The POWHEL sample at 7 TeV

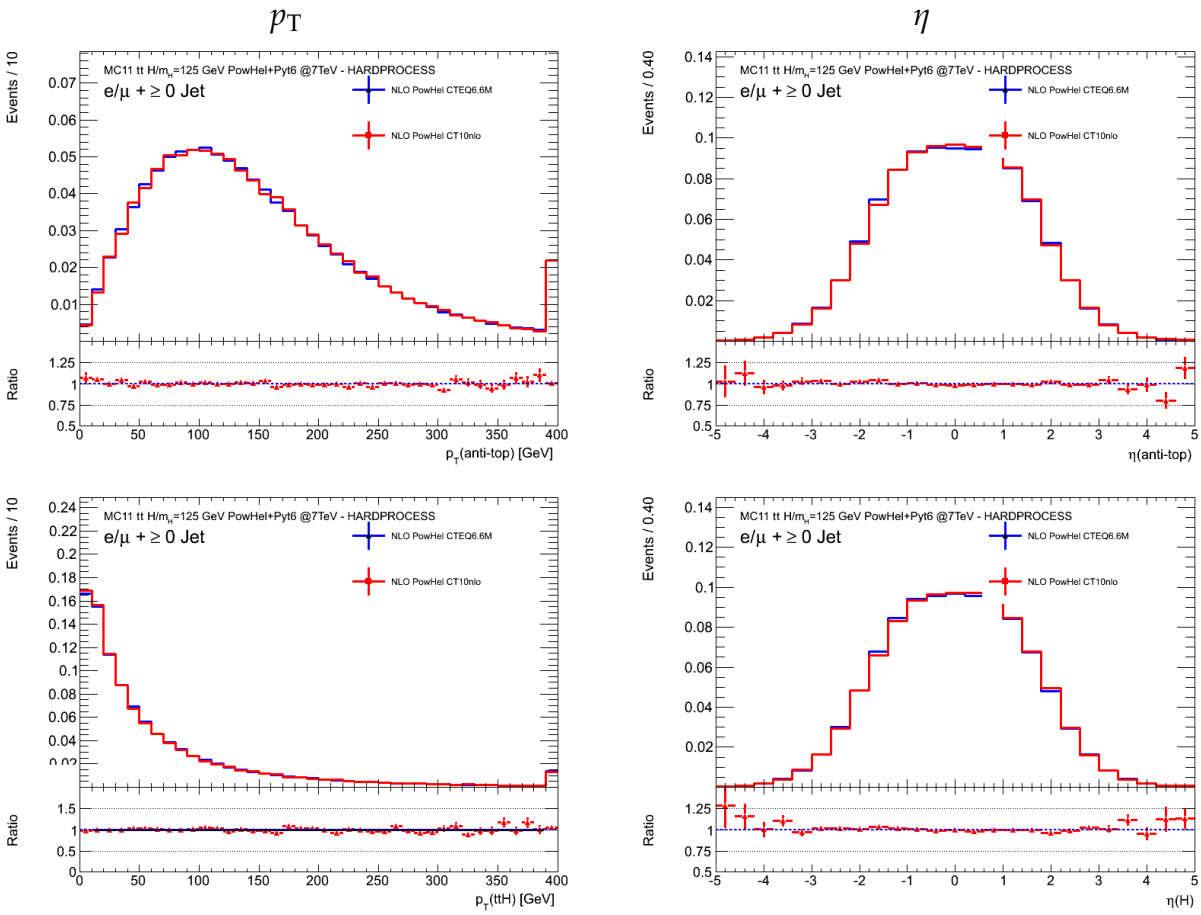

Fig. E.1.: The anti-top p_T and η, $t\bar{t}H$ p_T and Higgs p_T distribuions for POWHEL with CTEQ6.6M (blue) and CT10nlo (red) at 7 TeV. The distributions are normalised to unity.

E.2. The POWHEL sample at 8 TeV

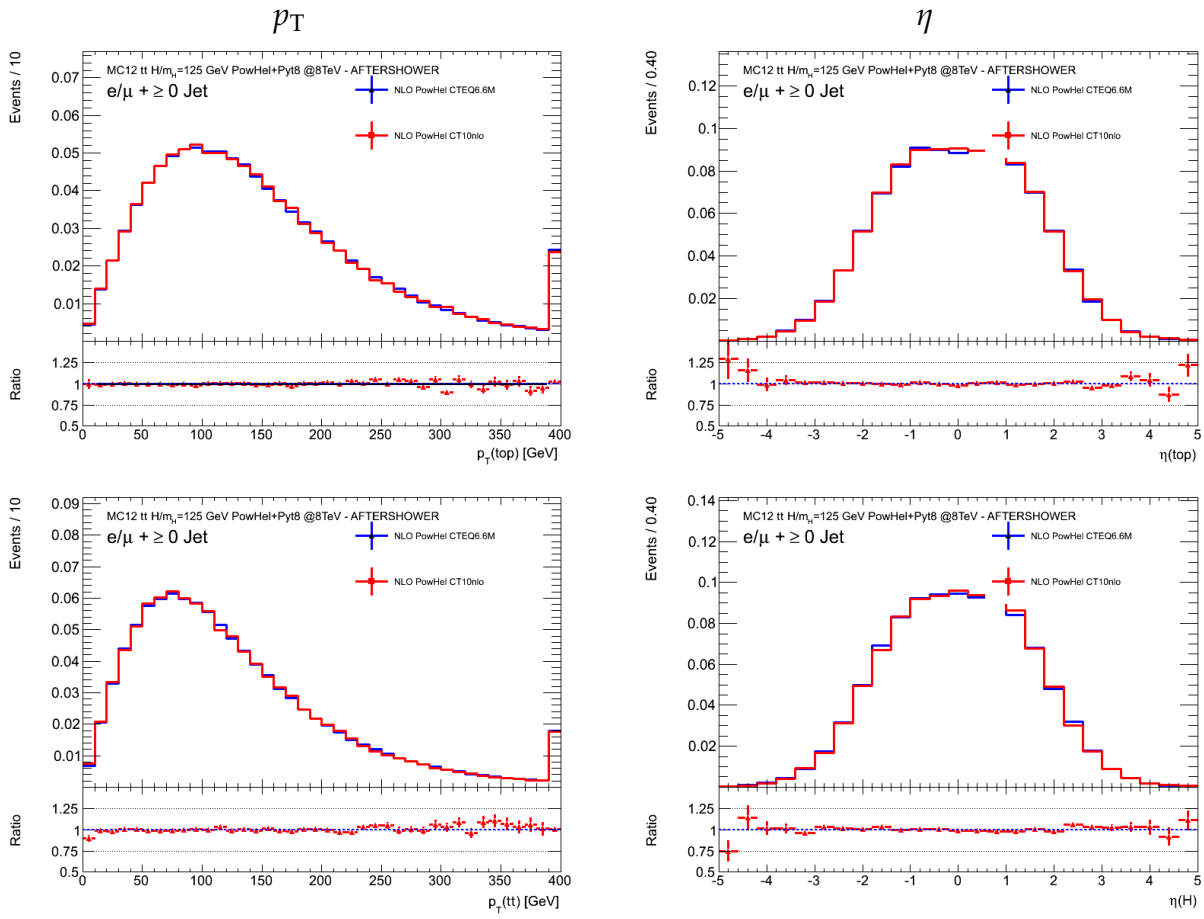

Fig. E.2.: The top p_T and η, $t\bar{t}H$ p_T and Higgs p_T distribuions for POWHEL with CTEQ6.6M (blue) and CT10nlo (red) at 8 TeV. The distributions are normalised to unity.

APPENDIX

F

ADDITIONAL MATERIAL

F.1. PDF structure functions for the $t\bar{t}H$ process

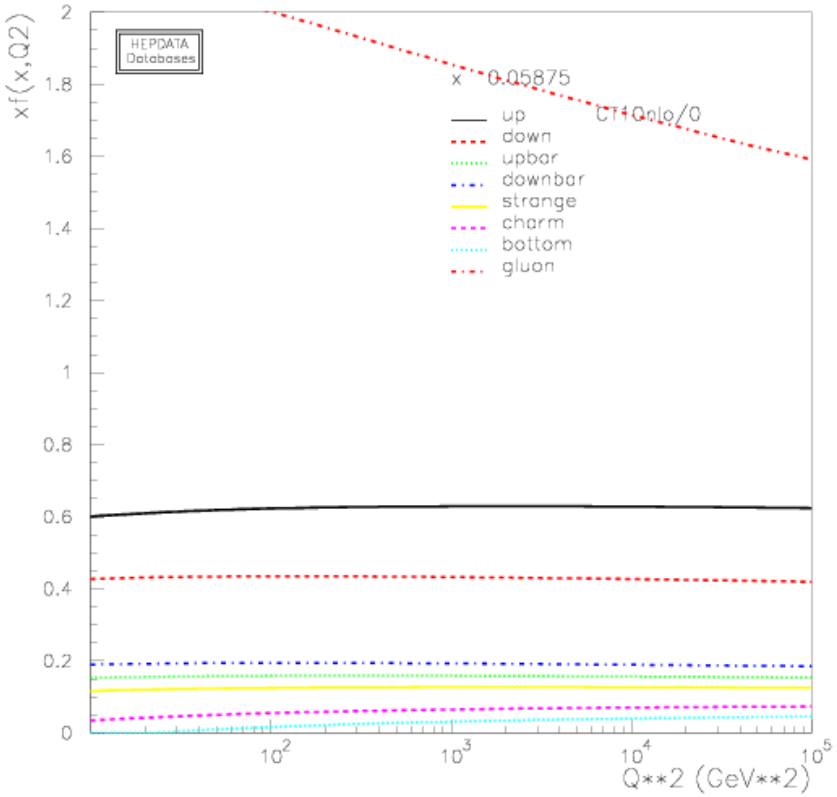

Fig. F.1.: The CT10nlo PDFs with respect to Q^2 for $x \sim (2m_t + m_H)/\sqrt{s} = 0.05875$ [49]. The sum of the quark PDFs and the gluon PDFs converges equally the higher the probed scale Q^2. Assuming a static scale $Q = m_t + m_H/2$, a probing scale of $Q^2 \approx 5.5 \cdot 10^4$ is obtained.

F.2. The set of POWHEL samples and corresponding parameters

sample no.	sample name	m_H [GeV]	m_t [GeV]	PDF set	scale μ_0 [GeV]	$\sqrt{s}$ [TeV]	$\sigma \pm$ stat. err. [fb]
The POWHEL *samples can be found here:* `http://grid.kfki.hu/twiki/bin/view/DbTheory/TthProd`							
3	tth-lhc-03-1M	125	172	CTEQ6.6M	$m_t + m_H/2$	7	84.274 ± 0.289
4	lhc-05-1M	120	172.5	MSTW2008	$(m_T^t m_T^{\bar{t}} m_T^H)^{1/3}$	7	104.467 ± 0.343
5	lhc-06-1M	120	172.5	MSTW2008	$m_t + m_H/2$	7	104.274 ± 1.892
6	lhc-07-1M	120	172.5	MSTW2008	$2 \times (m_t + m_H/2)$	7	91.983 ± 0.286
7	lhc-08-1M	120	172.5	MSTW2008	$(m_t + m_H/2)/2$	7	106.862 ± 0.682
unofficial samples provided by POWHEL *authors*							
8	tth-lhc-03-halfmu0-1M	125	172.5	CTEQ6.6M	$(m_t + m_H/2)/2$	7	86.963 ± 0.108
9	tth-lhc-03-twomu0-1M	125	172.5	CTEQ6.6M	$2 \times (m_t + m_H/2)$	7	76.258 ± 5.163
10	tth-lhc-09-1M	125	172.5	CTEQ6.6M	$m_t + m_H/2$	8	125.614 ± 0.007
11	tth-lhc-09-halfmu0-1M	125	172.5	CTEQ6.6M	$(m_t + m_H/2)/2$	8	130.782 ± 0.124
12	tth-lhc-09-twomu0-1M	125	172.5	CTEQ6.6M	$2 \times (m_t + m_H/2)$	8	114.124 ± 0.006
13	tth-lhc-10-1M	125	172.5	CT10nlo	$(m_T^t m_T^{\bar{t}} m_T^H)^{1/3}$	7	86.532 ± 0.533
14	tth-lhc-11-1M	125	172.5	CT10nlo	$(m_T^t m_T^{\bar{t}} m_T^H)^{1/3}$	8	129.528 ± 0.847

Tab. F.1.: The table contains the set of POWHEL samples that are either to find at `http://grid.kfki.hu/twiki/bin/view/DbTheory/TthProd` and published in Ref. [198] or that were provided by the POWHEL authors. The table includes a list of parameters that where used to generate the samples such as the scale μ_0 that is equal to the factorisation and renormalisation scale. The resulting cross-sections including the corresponding statistical error can be found in the last column.

BIBLIOGRAPHY

[1] ATLAS Collaboration, *Observation of a new particle in the search for the Standard Model Higgs boson with the ATLAS detector at the LHC*, Phys. Lett. **B716** (2012) 1–29. Cited on p. 1, 28 und 32.

[2] CMS Collaboration, *Observation of a new boson at a mass of 125 GeV with the CMS experiment at the LHC*, Phys. Lett. **B716** (2012) 30–61. Cited on p. 1 und 32.

[3] J. Cammin and M. Schumacher, *The ATLAS discovery potential for the channel $t\bar{t}H$, H to $b\bar{b}$*, ATL-PHYS-2003-024, ATL-COM-PHYS-2003-027, CERN-ATL-PHYS-2003-024 (2003). Cited on p. 1.

[4] CDF Collaboration, *Combined search for the standard model Higgs boson decaying to a $b\bar{b}$ pair using the full CDF data set*, Phys. Rev. Lett. **109** (2012) 111802. Cited on p. 1.

[5] DØ Collaboration, *Combined search for the standard model Higgs boson decaying to $b\bar{b}$ using the DØ Run II data set*, Phys. Rev. Lett. **109** (2012) 121802. Cited on p. 1.

[6] CMS Collaboration, *Search for the standard model Higgs boson decaying to bottom quarks in pp collisions at $\sqrt{s}$ = 7 TeV*, Phys. Lett. B **710** (2012) 284–306. Cited on p. 1.

[7] CDF and DØ Collaboration, *Evidence for a particle produced in association with weak bosons and decaying to a bottom-antibottom quark pair in Higgs boson searches at the TEVATRON*, Phys. Rev. Lett. **109** (2012) 071804. Cited on p. 1.

[8] CDF Collaboration, *Search for the standard model Higgs boson produced in association with top quarks using the full CDF data set*, Phys. Rev. Lett. **109** (2012) 181802. Cited on p. 1.

[9] ATLAS Collaboration, *Search for the Standard Model Higgs boson produced in association with top quarks in proton-proton collisions at $\sqrt{s}$ = 7 TeV using the ATLAS detector*, ATLAS-CONF-2012-135 (2012). Cited on p. 1 und 2.

[10] CMS Collaboration, *Search for the standard model Higgs boson produced in association with a top-quark pair in pp collisions at the LHC*, CMS-HIG-12-035 (2013). Cited on p. 1 und 34.

[11] W. Beenakker et al., *Higgs Radiation off Top Quarks at the TEVATRON and the LHC*, Phys. Rev. Lett. **87** (2001) 201805. Cited on p. 2, 33 und 53.

[12] O. Brein et al., *Top-Quark Mediated Effects in Hadronic Higgs-Strahlung*, Eur. Phys. J. C **72** (2011) 1868. Cited on p. 2 und 33.

[13] S. Dawson, L. H. Orr, L. Reina, et al., *NLO QCD Predictions for associated $t\bar{t}H$ production in Hadronic Collisions*, Nucl. Phys. B, Proc. Suppl. **116** (2002) 207. Cited on p. 2 und 33.

[14] C. Degrande et al., *Probing top-Higgs non-standard interactions at the LHC*, J. High Energy Phys. **07** (2012) 036. Cited on p. 2.

[15] S. L. Glashow, *Partial Symmetries of Weak Interactions*, Nucl. Phys. **22** (1961) 579–588. Cited on p. 3 und 5.

[16] S. Weinberg, *A Model of Leptons*, Phys. Rev. Lett. **19** (1967) 1264–1266. Cited on p. 3 und 5.

[17] A. Salam, *Weak and Electromagnetic Interactions*, ed. Nobel Symposium No. 8 Almqvist & Wiksell, Stockholm (2008). Cited on p. 3 und 5.

[18] D. Griffiths, *Introduction to Elementary Particles*, Wiley-VCH, Weinheim (2008). Cited on p. 3 und 5.

[19] C. Berger, *Elementarteilchenphysik*, Springer, Berlin (2006). Cited on p. 3 und 5.

[20] Particle Data Group, *Review of Particle Physics*, Phys. Rev. D **86** (2012) 010001. Cited on p. 3, 5, 9, 21 und 23.

[21] L. V. P. R. de Broglie, *Recherches sur la théorie des quanta*, PhD thesis, Paris U., Paris (1924) . Cited on p. 4.

[22] D. J. Gross and F. Wilczek, *Ultraviolet behavior of non-Abelian gauge theories*, Phys. Rev. Lett. **30** (1973) 1343–1346. Cited on p. 4.

[23] H. D. Politzer, *Reliable Perturbative Results for Strong Interactions?*, Phys. Rev. Lett. **30** (1973) 1346–1349. Cited on p. 4.

[24] G. Altarelli, *Collider Physics within the Standard Model: a Primer*, RM3-TH-13-1, CERN-PH-TH-2013-020 (2013). Cited on p. 5.

[25] R. K. Ellis, W. J. Stirling, and B. R. Webber, *QCD and Collider Physics*, Camb. Monogr. Part. Phys. Nucl. Phys. Cosmol. **8** (1996) 1–435. Cited on p. 5.

[26] P. W. Higgs, *Broken Symmetries, Massless Particles and Gauge Fields*, Phys. Lett. **12** (1964) 132–133. Cited on p. 6.

[27] F. Englert and R. Brout, *Broken Symmetry and the Mass of Gauge Vector Mesons*, Phys. Rev. Lett. **13** (1964) 321–322. Cited on p. 6.

[28] G. S. Guralnik, C. R. Hagen, and T. W. B. Kibble, *Global Conservation Laws and Massless Particles*, Phys. Rev. Lett. **13** (1964) 585–587. Cited on p. 6.

[29] MuLan Collaboration, *Improved measurement of the positive muon lifetime and determination of the Fermi constant*, Phys. Rev. Lett. **99** (2007) 032001. Cited on p. 7.

[30] A. Quadt, *Top quark physics at hadron colliders*, Eur. Phys. J. **C48** (2006) 835–1000. Cited on p. 8, 16, 20 und 26.

[31] N. Cabbibo, *Unitary Symmetry and Leptonic Decays*, Phys. Rev. Lett. **10** (1963) 531–532. Cited on p. 9.

[32] M. Kobayashi and T. Maskawa, *CP Violation in the Renormalizable Theory of Weak Interaction*, Prog. Theor. Phys. **49** (1973) 652–657. Cited on p. 9 und 18.

[33] Z. Maki, M. Nakagawa, and S. Sakata, *Remarks on the unified model of elementary particles*, Prog. Theor. Phys. **28** (1962) 870–880. Cited on p. 9.

[34] M. Kobayashi and T. Maskawa, *CP Violation in the Renormalizable Theory of Weak Interaction*, Prog. Theor. Phys. **49** (1973) 652–657. Cited on p. 9.

[35] J. Carvalho, N. Castro, A. Onofre, et al., *Study of ATLAS sensitivity to FCNC top decays*, ATL-PHYS-PUB-2005-009 (2005). Cited on p. 9.

[36] B. Pontecorvo, *Mesonium and anti-mesonium*, Sov. Phys. JETP **6** (1957) 429. Cited on p. 9.

[37] B. Pontecorvo, *Neutrino Experiments and the Problem of Conservation of Leptonic Charge*, Sov. Phys. JETP **26** (1968) 984–988. Cited on p. 9.

[38] S. Martin, *A Supersymmetry Primer*, `arXiv:9709356 [hep-ph]` (1997). Cited on p. 9 und 10.

[39] E. R. Hudson and D. Saltzberg, *Antiprotons Reflect a Magnetic Symmetry*, Physics **6** (2013) 36. Cited on p. 9.

[40] AMS Collaboration, *First Result from the Alpha Magnetic Spectrometer on the International Space Station: Precision Measurement of the Positron Fraction in Primary Cosmic Rays of 0.5-350 GeV*, Phys. Rev. Lett. **110** (2013) 141102. Cited on p. 9.

[41] H. Murayama, *Supersymmetry Phenomenology*, `arXiv:0002232v2 [hep-ph]` (2000). Cited on p. 10.

[42] H. E. Haber and G. L. Kane, *The search for supersymmetry: Probing physics beyond the standard model*, Phys. Rep. **117** (1985) 75. Cited on p. 10.

[43] H. P. Nilles, *Supersymmetry, supergravity and particle physics*, Phys. Rep. **110** (1984) 1. Cited on p. 10.

[44] R. P. Feynman, *Very High-Energy Collisions of Hadrons*, Phys. Rev. Lett. **23** (1969) 1415–1417. Cited on p. 10.

[45] A. D. Martin, *Proton structure, Partons, QCD, DGLAP and beyond*, IPPP-08-03, DCPT-08-06 (2008). Cited on p. 11.

[46] J. Bjørken and E. A. Paschos, *Inelastic Electron Proton and gamma Proton Scattering, and the Structure of the Nucleon*, Phys. Rev. **185** (1969) 1975–1982. Cited on p. 11.

[47] S. Drell and T.-M. Yan, *Partons and their Applications at High-Energies*, Ann. Phys. **66** (1971) 578. Cited on p. 11.

[48] J. C. Collins and D. E. Soper, *The Theorems of Perturbative QCD*, Ann. Rev. Nucl. Part. Sci. **37** (1987) 383. Cited on p. 11 und 16.

[49] H.-L. Lai, M. Guzzi, J. Huston, et al., *New parton distributions for collider physics*, Phys. Rev. **D82** (2010) 074024. Cited on p. 12, 61, 70 und 102.

[50] A. M. Cooper-Sarkar, R. C. E. Devenish, and A. De Roeck, *Structure Functions of the Nucleon and their Interpretation*, Int. J. Mod. Phys. A **13** (1998) 3385–3586. Cited on p. 12.

[51] J. Pumplin et al., *New Generation of Parton Distributions with Uncertainties from Global QCD Analysis*, J. High Energy Phys. **0207** (2002) 012. Cited on p. 12.

[52] A. Martin et al., *Physical Gluons and High E_T Jets*, Phys. Lett. B **604** (2004) 61. Cited on p. 12.

[53] A. Martin et al., *Uncertainties of predictions from parton distrbutions, I. Experimental errors*, Eur. Phys. J. C **28** (2003) 455. Cited on p. 12.

[54] F. Siegert, *Monte-Carlo event generation for the LHC*, PhD thesis, Durham U., Durham (2010) . Cited on p. 13 und 16.

[55] T. Kinoshita, *Mass singularities of Feynman amplitudes*, J. Math. Phys. **3** (1962) 650–677. Cited on p. 13.

[56] T. Lee and M. Nauenberg, *Degenerate Systems and Mass Singularities*, Phys. Rev. **133** (1964) B1549–B1562. Cited on p. 13.

[57] S. Bethke, *Experimental tests of asymptotic freedom*, Prog. Part. Nucl. Phys. **58** (2007) 351 – 386. Cited on p. 14.

[58] V. Chekelian, *Experimental review of unpolarised nucleon structure functions*, Nucl. Phys. A **755** (2005) 111–122. Cited on p. 14.

[59] S. Frixione, Z. Kunszt, and A. Signer, *Three jet cross-sections to next-to-leading order*, Nucl.Phys. **B467** (1996) 399–442. Cited on p. 14 und 49.

[60] J. M. Campbell, J. Huston, and W. Stirling, *Hard Interactions of Quarks and Gluons: A Primer for LHC Physics*, Rept. Prog. Phys. **70** (2007) 89. Cited on p. 16.

[61] O. Behnke, K. Kröninger, G. Schott, et al., *Data analysis in high energy physics: a practical guide to statistical methods*, Wiley-VCH, Weinheim (2013). Cited on p. 16.

[62] T. Gleisberg et al., *Monte Carlo Models at the LHC*, Proceedings of the DIS2004, Strbske Pleso, Slovakia,. arXiv:0407365 [hep-ph] (2004). Cited on p. 16.

[63] T. Gleisberg et al., *SHERPA 1.α, a proof-of-concept version*, J. High Energy Phys. **0402** (2004) 056. Cited on p. 16.

[64] A. Schälicke et al., *Event Generator for Particle Production in High-Energy Collisions*, Prog. Part. Nucl. Phys. **53** (2004) 329–338. Cited on p. 16, 48 und 50.

[65] J. Baglio and A. Djouadi, *Higgs production at the LHC*, J. High Energy Phys. **1103** (2011) 055. Cited on p. 16 und 17.

[66] S. Dawson, C. Jackson, L. Orr, et al., *Associated Higgs production with top quarks at the large hadron collider: NLO QCD corrections*, Phys. Rev. **D68** (2003) 034022. Cited on p. 17, 18 und 53.

[67] H. L. Lai, J. Huston, S. E. Kuhlmann, et al., *Global QCD Analysis of Parton Structure of the Nucleon: CTEQ5 Parton Distributions*, Eur. Phys. J. C **12** (2000) 375–392. Cited on p. 18.

[68] DØ Collaboration, *Observation of the Top Quark*, Phys. Rev. Lett. **74** (1995) 2632–2637. Cited on p. 18.

[69] CDF Collaboration, *Observation of Top Quark Production in $p\bar{p}$ Collisions with the Collider Detector at FERMILAB*, Phys. Rev. Lett. **74** (1995) 2626–2631. Cited on p. 18.

[70] CDF Collaboration, *Observation of Electroweak Single Top-Quark Production*, Phys. Rev. Lett. **103** (2009) 092002. Cited on p. 18.

[71] DØ Collaboration, *Observation of Single Top Quark Production*, Phys. Rev. Lett. **103** (2009) 092001. Cited on p. 18.

[72] L. Sonnenschein, *Top Quark Physics at the LHC*, Proceedings of the 14th International Spin Physics Symposium (SPIN2000), Osaka, Japan (2000). Cited on p. 20.

[73] G. Cortiana, *Measurement of Top Mass and Properties with the ATLAS Detector*, http://cds.cern.ch/record/1559255 (2013). Cited on p. 21.

[74] TEVATRON Electroweak Working Group, *Combination of CDF and DØ results on the mass of the top quark using up to 8.7 fb^{-1} at the TEVATRON*, arXiv:1305.3929 [hep-ex] (2013). Cited on p. 22.

[75] ATLAS and CMS Collaboration, *Combination of ATLAS and CMS results on the mass of the top-quark using up to 4.9 fb^{-1} of $\sqrt{s} = 7$ TeV LHC data*, ATLAS-CONF-2013-102 (2013). Cited on p. 22.

[76] E. Yazgan, *Measurements of Top Quark Properties at the LHC*, arXiv:1304.3324 [hep-ex] (2013). Cited on p. 22.

[77] ATLAS Collaboration, *Measurement of the top quark charge in pp collisions at $\sqrt{s} = 7$ TeV with the ATLAS detector*, CERN-PH-EP-2013-056 (2013). Cited on p. 23.

[78] CDF Collaboration, *Direct Top-Quark Width Measurement at CDF*, Phys. Rev. Lett. **105** (2010) 232003. Cited on p. 23.

[79] ATLAS Collaboration, *Measurement of t-Channel Single Top-Quark Production in pp Collisions at $\sqrt{s}$ = 8 TeV with the ATLAS detector*, ATLAS-CONF-2012-132 (2012). Cited on p. 23.

[80] M. Czakon, P. Fiedler, and A. Mitov, *The total top quark pair production cross-section at hadron colliders through $\mathcal{O}(\alpha_S^4)$*, Phys. Rev. Lett. **110** (2013) 252004. Cited on p. 23.

[81] ATLAS Collaboration, *Statistical combination of top quark pair production cross-section measurements using dilepton, single-lepton, and all-hadronic final states at $\sqrt{s} = 7$ TeV with the ATLAS detector*, ATLAS-CONF-2012-024 (2012). Cited on p. 23.

[82] ATLAS Collaboration, *Measurement of the top quark pair production cross section in the single-lepton channel with ATLAS in proton-proton collisions at 8 TeV using kinematic fits with b-tagging*, ATLAS-CONF-2012-149 (2012). Cited on p. 23.

[83] A. Brandenburg, Z. G. Si, and P. Uwer, *QCD-corrected spin analysing power of jets in decays of polarized top quarks*, Phys. Lett. B **539** (2002) 235–241. Cited on p. 24.

[84] ATLAS Collaboration, *Measurement of top quark polarisation in $t\bar{t}$ events with the ATLAS detector in proton-proton collisions at $\sqrt{s} = 7$ TeV*, ATLAS-CONF-2012-133 (2012). Cited on p. 24.

[85] ATLAS and CMS Collaboration, *Combination of the ATLAS and CMS measurements of the W-boson polarization in top-quark decays*, ATLAS-CONF-2013-033 (2013). Cited on p. 25 und 70.

[86] G. L. Kane, G. A. Ladinsky, and C. P. Yuan, *Using the top quark for testing standard-model polarization and* CP *predictions*, Phys. Rev. D **45** (1992) 124–141. Cited on p. 25.

[87] ATLAS Collaboration, *Measurement of the W-boson polarisation in top quark decays in pp collision data at $\sqrt{s}$ = 7 TeV using the ATLAS detector*, ATLAS-CONF-2011-037 (2011). Cited on p. 25.

[88] CMS Collaboration, *W-helicity in top pair events*, CMS-PAS-TOP-11-020 (2012). Cited on p. 25.

[89] CMS Collaboration, *Measurement of W-Polarization in Di-Leptonic ttbar Events in pp Collisions with $\sqrt{s}$ = 7 TeV*, CMS-PAS-TOP-12-015 (2013). Cited on p. 25.

[90] A. Czarnecki, J. G. Körner, and J. H. Piclum, *Helicity fractions of W bosons from top quark decays at next-to-next-to-leading order in QCD*, Phys. Rev. D **81** (2010) 111503. Cited on p. 25.

[91] CDF Collaboration, *Measurement of the Helicity of W Bosons in Top-Quark Decays*, CDF note 7804 (2005). Cited on p. 26.

[92] W. Bernreuther and Z.-G. Si, *Distributions and correlations for top quark pair production and decay at the TEVATRON and LHC*, Nucl. Phys. B **837** (2010) 90 –121. Cited on p. 26.

[93] G. Mahlon and S. Parke, *Angular correlations in top quark pair production and decay at hadron colliders*, Phys. Rev. D **53** (1996) 4886–4896. Cited on p. 26.

[94] T. Stelzer and S. Willenbrock, *Spin correlation in top-quark production at hadron colliders*, Physics Letters B **374** (1996) 169 – 172. Cited on p. 26.

[95] G. Mahlon and S. J. Parke, *Spin correlation effects in top quark pair production at the LHC*, Phys. Rev. D **81** (2010) 074024. Cited on p. 26.

[96] W. Bernreuther, A. Brandenburg, Z. G. Si, et al., *Top quark pair production and decay at hadron colliders*, Nucl. Phys. B **690** (2004) 81. Cited on p. 26.

[97] ATLAS Collaboration, *Observation of Spin Correlation in $t\bar{t}$ Events from pp Collisions at $\sqrt{s} = 7$ TeV Using the ATLAS Detector*, Phys. Rev. Lett. **108** (2012) 212001. Cited on p. 27 und 66.

[98] CDF Collaboration, *Measurement of $t\bar{t}$ spin correlation in $p\overline{p}$ collisions using the CDF II detector at the TEVATRON*, Phys. Rev. D **83** (2011) 031104. Cited on p. 27.

[99] DØ Collaboration, *Measurement of Spin Correlation in $t\bar{t}$ Production Using a Matrix Element Approach*, Phys. Rev. Lett. **107** (2011) 032001. Cited on p. 27.

[100] DØ Collaboration, *Measurement of spin correlation in $t\bar{t}$ production using dilepton final states*, Phys.Lett. **B702** (2011) 16–23. Cited on p. 27.

[101] DØ Collaboration, *Evidence for Spin Correlation in $t\bar{t}$ Production*, Phys. Rev. Lett. **108** (2012) 032004. Cited on p. 27.

[102] B. ZHOU, *Summary of Higgs Results from ATLAS*, `http://cds.cern.ch/record/1574188` (2013). Cited on p. 28.

[103] ATLAS Collaboration, *Measurements of Higgs boson production and couplings in diboson final states with the ATLAS detector at the LHC*, CERN-PH-EP-2013-103 (2013). Cited on p. 28.

[104] ATLAS Collaboration, *Search for the Standard Model Higgs boson in the $H \to Z\gamma$ decay mode with pp collisions at $\sqrt{s} = 7$ and 8 TeV*, ATLAS-CONF-2013-009 (2013). Cited on p. 28.

[105] ATLAS Collaboration, *Search for a Standard Model Higgs boson in $H \to \mu\mu$ decays with the ATLAS detector*, ATLAS-CONF-2013-010 (2013). Cited on p. 28.

[106] ATLAS Collaboration, *Measurements of the properties of the Higgs-like boson in the two photon decay channel with the ATLAS detector using 25 $fb^{-1}$of proton-proton collision data*, ATLAS-CONF-2013-012 (2013). Cited on p. 28.

[107] ATLAS Collaboration, *Measurements of the properties of the Higgs-like boson in the four lepton decay channel with the ATLAS detector using 25 $fb^{-1}$of proton-proton collision data*, ATLAS-CONF-2013-013 (2013). Cited on p. 28.

[108] ATLAS Collaboration, *Search for a high-mass Higgs boson in the $H \to WW \to \ell\nu\ell\nu$ decay channel with the ATLAS detector using 21 $fb^{-1}$of proton-proton collision data*, ATLAS-CONF-2013-067 (2013). Cited on p. 28.

[109] ATLAS Collaboration, *Search for associated production of the Higgs boson in the $WH \to WWW^{(\star)} \to \ell\nu\ell\nu\ell\nu$ and $ZH \to ZWW^{(\star)} \to \ell\ell\ell\nu\ell\nu$ channels with the ATLAS detector at the LHC*, ATLAS-CONF-2013-075 (2013). Cited on p. 28.

[110] ATLAS Collaboration, *Search for the bb decay of the Standard Model Higgs boson in associated W/ZH production with the ATLAS detector*, ATLAS-CONF-2013-079 (2013). Cited on p. 28.

[111] ATLAS Collaboration, *Search for $t\bar{t}H$ production in the $H \to \gamma\gamma$ channel at $\sqrt{s} = 8$ TeV with the ATLAS detector*, ATLAS-CONF-2013-080 (2013). Cited on p. 28 und 42.

[112] CMS Collaboration, *Combination of standard model Higgs boson searches and measurements of the properties of the new boson with a mass near 125 GeV*, CMS-PAS-HIG-13-005 (2013). Cited on p. 28.

[113] CMS Collaboration, *Evidence for a particle decaying to W^+W^- in the fully leptonic final state in a standard model Higgs boson search in pp collisions at the LHC*, CMS-PAS-HIG-13-003 (2013). Cited on p. 28.

[114] CMS Collaboration, *Search for the Standard-Model Higgs boson decaying to tau pairs in proton-proton collisions at $\sqrt{s}$ = 7 and 8 TeV*, CMS-PAS-HIG-13-004 (2013). Cited on p. 28.

[115] CMS Collaboration, *Search for a Higgs boson decaying into a Z and a photon in pp collisions at $\sqrt{s}$ = 7 and 8 TeV*, CMS-HIG-13-006, CERN-PH-EP-2013-113 (2013). Cited on p. 28.

[116] CMS Collaboration, *Search for a Standard Model-like Higgs boson decaying into $WW \to \ell\nu q\bar{q}$ in pp collisions at $\sqrt{s} = 8$ TeV*, CMS-PAS-HIG-13-008 (2013). Cited on p. 28.

[117] CMS Collaboration, *Search for SM Higgs in WH to $WWW \to 3\ell 3\nu$*, CMS-PAS-HIG-13-009 (2013). Cited on p. 28.

[118] CMS Collaboration, *Search for a non-standard-model Higgs boson decaying to a pair of new light bosons in four-muon final states*, CMS-PAS-HIG-13-010 (2013). Cited on p. 28.

[119] CMS Collaboration, *Higgs to bb in the VBF channel*, CMS-PAS-HIG-13-011 (2013). Cited on p. 28.

[120] CMS Collaboration, *Search for the standard model Higgs boson produced in association with W or Z bosons, and decaying to bottom quarks for LHCp 2013*, CMS-PAS-HIG-13-012 (2013). Cited on p. 28.

[121] CMS Collaboration, *Search for a heavy Higgs boson in the $H \to ZZ \to 2\ell 2\nu$ channel in pp collisions at $\sqrt{s} = 7$ and 8 TeV*, CMS-PAS-HIG-13-014 (2013). Cited on p. 28.

[122] CMS Collaboration, *Search for ttH production in events where H decays to photons at 8 TeV collisions*, CMS-PAS-HIG-13-015 (2013). Cited on p. 28 und 42.

[123] CMS Collaboration, *Properties of the observed Higgs-like resonance using the diphoton channel*, CMS-PAS-HIG-13-016 (2013). Cited on p. 28.

[124] CMS Collaboration, *VH with $H \to WW \to \ell\nu\ell\nu$ and $V \to jj$*, CMS-PAS-HIG-13-017 (2013). Cited on p. 28.

[125] CMS Collaboration, *Search for invisible Higgs produced in association with a Z boson*, CMS-PAS-HIG-13-018 (2013). Cited on p. 28.

[126] CMS Collaboration, *Update of the search for the Standard Model Higgs boson decaying into WW in the vector boson fusion production channel*, CMS-PAS-HIG-13-022 (2013). Cited on p. 28.

[127] CDF and DØ Collaboration, *Higgs Boson Studies at the TEVATRON*, Phys.Rev. **D88** (2013) 052014. Cited on p. 28.

[128] ATLAS Collaboration, *Combined coupling measurements of the Higgs-like boson with the ATLAS detector using up to 25 fb^{-1} of proton-proton collision data*, ATLAS-CONF-2013-034 (2013). Cited on p. 29.

[129] CMS Collaboration, *Combination of standard model Higgs boson searches and measurements of the properties of the new boson with a mass near 125 GeV*, CMS-PAS-HIG-13-005 (2013). Cited on p. 29.

[130] LHC Higgs Cross Section Working Group, *Handbook of LHC Higgs Cross Sections: 1. Inclusive Observables*, `arXiv:1101.0593 [hep-ph]` (2011). Cited on p. 30, 31, 32 und 65.

[131] E. Gross, G. Wolf, and B. A. Kniehl, *Production and decay of the Standard Model Higgs boson LEP-200*, Z. Phys. **C63** (1994) 417–426. Cited on p. 31.

[132] J. Cammin, *Study of a light Standard Model Higgs Boson in the $t\bar{t}H$ Channel with ATLAS and LHC Decay Mode Independent Searches for Neutral Higgs Bosons with OPAL at LEP*, PhD thesis, Bonn U., Bonn (2004) . Cited on p. 31.

[133] CMS Collaboration, *Search for a standard-model-like Higgs boson with a mass of up to 1 TeV at the LHC*, CMS-HIG-12-034, CERN-PH-EP-2013-050 (2013). Cited on p. 32.

[134] V. Hirschi et al., *Automation of one-loop QCD corrections*, J. High Energy Phys. **1105** (2011) 044. Cited on p. 33, 48 und 50.

[135] Frederix et al., *Scalar and pseudoscalar Higgs production in association with a top-antitop pair*, Phys.Lett. **B701** (2011) 427–433. Cited on p. 33, 47, 48, 50 und 53.

[136] R. Pittau, *Status of* MADLOOP/*a*MC@NLO, `arXiv:1202.5781 [hep-ph]` (2012). Cited on p. 33, 48 und 50.

[137] F. Maltoni, D. L. Rainwater, and S. S. D. Willenbrock, *Measuring the top-quark Yukawa coupling at hadron colliders via $t\bar{t}H$, $H \to WW$*, Phys. Rev. D **66** (2002) 034022. Cited on p. 34.

[138] A. S. Belyaev and L. Reina, $pp \to t\bar{t}H, H \to \tau^+\tau^-$, J. High Energy Phys. **08** (2002) 041. Cited on p. 34.

[139] O. S. Brüning et al., *LHC Design Report*, vol. 1. CERN, Geneva (2004). Cited on p. 35.

[140] O. S. Brüning et al., *LHC Design Report*, vol. 2. CERN, Geneva (2004). Cited on p. 35.

[141] LHCb Collaboration, *A Large Hadron Collider beauty experiment*, J. Instrum. **3** (2008) . Cited on p. 36.

[142] ALICE Collaboration, *The ALICE experiment at the CERN LHC*, J. Instrum. **3** (2008) . Cited on p. 36.

[143] R. Nicolaidou, *Overview of Higgs boson searches at LHC*, `http://cds.cern.ch/record/1565220` (2013). Cited on p. 37.

[144] ATLAS Collaboration, *The ATLAS Experiment at the CERN Large Hadron Collider*, J. Instrum. **3** (2008) S08003. Cited on p. 37 und 40.

[145] ATLAS Collaboration, *ATLAS detector and physics performance: Technical Design Report, 1*, Technical Design Report ATLAS. CERN, Geneva (1999). Cited on p. 37.

[146] ATLAS Collaboration, *ATLAS Detector and Physics Performance TDR, Volume I+II*, CERN/LHCC/99-14/15 (unpublished) (1999) . Cited on p. 37.

[147] N. Wermes and G. Hallewel, *ATLAS pixel detector: Technical Design Report*, Technical Design Report ATLAS. CERN, Geneva (1998). Cited on p. 39.

[148] ATLAS Collaboration, *ATLAS inner detector: Technical Design Report, 1*, Technical Design Report ATLAS. CERN, Geneva (1997). Cited on p. 39.

[149] ATLAS Collaboration, *The ATLAS Inner Detector commissioning and calibration*, Eur. Phys. J. **C70** (2010) 787–821. Cited on p. 39.

[150] ATLAS Collaboration, *ATLAS magnet system: Technical Design Report, 1*, Technical Design Report ATLAS. CERN, Geneva (1997). Cited on p. 39 und 40.

[151] ATLAS Collaboration, *ATLAS central solenoid: Technical Design Report*, Technical Design Report ATLAS. CERN, Geneva (1997). Cited on p. 39.

[152] ATLAS Collaboration, *ATLAS central solenoid: Technical Design Report*, Technical Design Report ATLAS. CERN, Geneva (1997). Cited on p. 39.

[153] ATLAS Collaboration, *ATLAS tile calorimeter: Technical Design Report*, Technical Design Report ATLAS. CERN, Geneva (1996). Cited on p. 39.

[154] ATLAS Collaboration, *ATLAS liquid-argon calorimeter: Technical Design Report*, Technical Design Report ATLAS. CERN, Geneva (1996). Cited on p. 39.

[155] ATLAS Collaboration, *The muon spectrometer of the ATLAS experiment*, Nucl. Phys. B - Proc. Suppl. **125** (2003) 337 – 345. Cited on p. 40.

[156] ATLAS Collaboration, *ATLAS barrel toroid: Technical Design Report*, Technical Design Report ATLAS. CERN, Geneva (1997). Cited on p. 40.

[157] ATLAS Collaboration, *ATLAS end-cap toroids: Technical Design Report*, Technical Design Report ATLAS. CERN, Geneva (1997). Cited on p. 40.

[158] ATLAS Collaboration, *Performance of the ATLAS Trigger System in 2010*, Eur. Phys. J. **C72** (2012) 1849. Cited on p. 40.

[159] CDF Collaboration, *Search for the standard model Higgs boson produced in association with top quarks using the full CDF data set*, Phys. Rev. Lett. **109** (2012) 181802. Cited on p. 42.

[160] ATLAS Collaboration, *Search for the Standard Model Higgs boson produced in association with top quarks in proton-proton collisions at $\sqrt{s}$ = 7 TeV using the ATLAS detector*, ATLAS-CONF-2012-135 (2012). Cited on p. 42, 43, 44, 45, 46, 48, 54 und 58.

[161] CMS Collaboration, *Search for the standard model Higgs boson produced in association with a top-quark pair in pp collisions at the LHC*, J. High Energy Phys. **05** (2013) 145. Cited on p. 42.

[162] CMS Collaboration, *Search for Higgs Boson Production in Association with a Top-Quark Pair and Decaying to Bottom Quarks or Tau Leptons*, CMS-PAS-HIG-13-019 (2013). Cited on p. 42.

[163] O. Nackenhorst, *Search for the Standard Model Higgs boson in association with top quarks and decaying to bb at $\sqrt{s}$ = 7 TeV using the ATLAS detector*, ATL-PHYS-PROC-2013-048 (2013). Cited on p. 43.

[164] ATLAS Collaboration, *Measurement of $t\bar{t}$ production with a veto on additional central jet activity in pp collisions at $\sqrt{s}$ = 7 TeV using the ATLAS detector*, Eur. Phys. J. **C72** (2012) 2043. Cited on p. 45 und 58.

[165] S. Alioli, P. Nason, C. Oleari, et al., *A general framework for implementing NLO calculations in shower Monte Carlo programs: the* POWHEG BOX, J. High Energy Phys. **1006** (2010) 043. Cited on p. 47 und 49.

[166] S. Höche, F. Krauss, M. Schönherr, et al., *A critical appraisal of NLO+PS matching methods*, J. High Energy Phys. **1209** (2012) 049. Cited on p. 47.

[167] LHC Higgs Cross Section Working Group, *Handbook of LHC Higgs Cross Sections: 3. Higgs Properties*, `arXiv:1307.1347 [hep-ex]` (2013). Cited on p. 48.

[168] T. Sjöstrand, S. Mrenna, and P. Skands, *PYTHIA 6.4 Physics and Manual*, J. High Energy Phys. **05** (2006) 026. Cited on p. 48, 51 und 52.

[169] M. V. Garzelli et al., *Top-antitop pair hadroproduction in association with a heavy boson at the NLO QCD accuracy + Parton Shower*, `arXiv:1302.5381 [hep-ph]` (2013). Cited on p. 48, 49 und 50.

[170] T. Sjöstrand, S. Mrenna, and P. Skands, *A Brief Introduction to PYTHIA 8.1*, `arXiv:0710.3820 [hep-ph]` (2007). Cited on p. 48 und 51.

[171] M. Mangano, M. Moretti, F. Piccinini, et al., ALPGEN, *a generator for hard multiparton processes in hadronic collisions*, J. High Energy Phys. **07** (2003) 001. Cited on p. 48 und 49.

[172] H. van Deurzen et al., *NLO QCD corrections to the production of Higgs plus two jets at the LHC*, `arXiv:1301.0493 [hep-ph]` (2013). Cited on p. 48 und 50.

[173] H. van Deurzen, G. Luisoni, P. Mastrolia, et al., *NLO QCD corrections to Higgs boson production in association with a top quark pair and a jet*, `arXiv:1307.8437 [hep-ph]` (2013). Cited on p. 48 und 50.

[174] F. Maltoni and T. Stelzer, *MADEVENT: Automatic Event Generation with* MADGRAPH, J. High Energy Phys. **02** (2003) 027. Cited on p. 48 und 49.

[175] J. Alwall, P. Demin, S. de Visscher, et al., *MADGRAPH/MADEVENT v4: The New Web Generation*, J. High Energy Phys. **0709** (2007) 028. Cited on p. 48 und 49.

[176] J. Alwall, M. Herquet, F. Maltoni, et al., *MADGRAPH 5: Going Beyond*, J. High Energy Phys. **1106** (2011) 128. Cited on p. 48 und 49.

[177] G. Marchesini et al., *HERWIG*, Comput. Phys. Commun. **67** (1992) 465. Cited on p. 49 und 51.

[178] G. Corcella et al., *HERWIG 6: an event generator for hadron emission reactions with interfering gluons (including supersymmetric processes)*, J. High Energy Phys. **0101** (2001) 010. Cited on p. 49 und 51.

[179] M. Bahr, S. Gieseke, M. Gigg, et al., *HERWIG ++ Physics and Manual*, Eur. Phys. J. **C58** (2008) 639–707. Cited on p. 49.

[180] K. Hagiwara, J. Kanzaki, Q. Li, et al., *Fast computation of* MADGRAPH *amplitudes on graphics processing unit (GPU)*, `arXiv:1305.0708 [hep-ph]` (2013). Cited on p. 49.

[181] P. Artoisenet, R. Frederix, O. Mattelaer, et al., *Automatic spin-entangled decays of heavy resonances in Monte Carlo simulations*, J. High Energy Phys. **1303** (2013) 015. Cited on p. 49, 68, 69 und 70.

[182] G. Bevilacqua et al., *Helac-NLO*, Comp. Phys. Commun. **184** (2013) 986. Cited on p. 49.

[183] S. Höche, F. Krauss, M. Schönherr, et al., *QCD matrix elements + parton showers: The NLO case*, `arXiv:1207.5030 [hep-ph]` (2012). Cited on p. 49.

[184] S. Frixione and B. R. Webber, *Matching NLO QCD computations and parton shower simulations*, J. High Energy Phys. **0206** (2002) 029. Cited on p. 49.

[185] P. Nason, *A new method for combining NLO QCD with shower Monte Carlo algorithms*, J. High Energy Phys. **11** (2004) 040. Cited on p. 49.

[186] S. Frixione, P. Nason, and C. Oleari, *Matching NLO QCD computations with Parton Shower simulations: the* POWHEG *method*, J. High Energy Phys. **0711** (2007) 070. Cited on p. 49.

[187] R. Frederix, S. Frixione, F. Maltoni, et al., *Automation of next-to-leading order computations in QCD: The FKS subtraction*, J. High Energy Phys. **0910** (2009) 003. Cited on p. 50.

[188] G. Cullen, N. Greiner, G. Heinrich, et al., *Automated One-Loop Calculations with GoSam*, `arXiv:1111.2034 [hep-ph]` (2011). Cited on p. 50.

[189] F. Krauss, R. Kuhn, and G. Soff, *A*MEGIC++ *1.0: A Matrix element generator in C++*, J. High Energy Phys. **0202** (2002) 044. Cited on p. 50.

[190] T. Gleisberg and F. Krauss, *Automating dipole subtraction for QCD NLO calculations*, Eur. Phys. J. **C53** (2008) 501–523. Cited on p. 50.

[191] S. Frixione, E. Laenen, P. Motylinski, et al., *Angular correlations of lepton pairs from vector boson and top quark decays in Monte Carlo simulations*, J. High Energy Phys. **0704** (2007) 081. Cited on p. 50.

[192] B. Cooper, J. Katzy, M. Mangano, et al., *Importance of a consistent choice of $\alpha(s)$ in the matching of* ALPGEN *and* PYTHIA, Eur. Phys. J. **C72** (2012) 2078. Cited on p. 51.

[193] S. Catani, F. Krauss, R. Kuhn, et al., *QCD Matrix Elements + Parton Showers*, J. High Energy Phys. **0111** (2001) 063. Cited on p. 51.

[194] F. Krauss, *Matrix Elements and Parton Showers in Hadronic Interactions*, J. High Energy Phys. **0208** (2002) 015. Cited on p. 51.

[195] M. L. Mangano, *A Review of MLM's Prescription for Removal of Double Counting*, `http://cepa.fnal.gov/patriot/mc4run2/MCTuning/061104/mlm.pdf` (2013). Cited on p. 51.

[196] A. Buckley, J. Butterworth, S. Gieseke, et al., *General-purpose event generators for LHC physics*, Phys. Rept. **504** (2011) 145–233. Cited on p. 51.

[197] J. Alwall et al., *A Standard format for Les Houches event files*, Comp. Phys. Commun. **176** (2007) 300–304. Cited on p. 51.

[198] M. Garzelli et al., *Standard Model Higgs boson production in association with a top anti-top pair at NLO with parton showering*, `arXiv:1108.0387 [hep-ph]` (2011). Cited on p. 53, 54 und 103.

[199] P. Artoisenet, P. de Aquino, F. Maltoni, et al., *Unravelling $t\bar{t}h$ via the matrix element method*, `arXiv:1304.6414 [hep-ph]` (2013). Cited on p. 53.

[200] A. Sherstnev and R. Thorne, *Parton Distributions for LO Generators*, Eur. Phys. J. **C55** (2008) 553–575. Cited on p. 54.

[201] A. Martin et al., *Parton distributions for the LHC*, Eur. Phys. J. **C63** (2009) 189–285. Cited on p. 54 und 68.

[202] J. Pumplin, D. R. Stump, H. L. Lai, et al., *New generation of parton distributions with uncertainties from global QCD analysis*, J. High Energy Phys. **0207** (2002) 012. Cited on p. 54.

[203] M. Cacciari, G. P. Salam, and G. Soyez, *The Anti-k(t) jet clustering algorithm*, J. High Energy Phys. **0804** (2008) 063. Cited on p. 54.

[204] S. Dittmaier, C. Mariotti, G. Passarino, et al., *Handbook of LHC Higgs Cross Sections: 2. Differential Distributions*, `arXiv:1201.3084 [hep-ph]` (2012). Cited on p. 75, 76 und 77.

ACKNOWLEDGEMENT

At first, I would like to express my gratitude to my mentor and first referee Prof. Dr. Arnulf Quadt for its long-standing and extraordinary support that allowed me to perform research within dedicated working groups, diverse stays at the world leading particle physics facilities and the participation at a variety of conferences and workshops. He exclusively formed my understanding in the field of particle physics with his great enthusiasm and knowledge and kept motivating me to pursue in this interesting field of research. Thanks for all the discussions and oustanding support. I also want to thank Prof. Dr. Ariane Frey for being the second referee of this thesis and additionally for her support of my participation in the CERN summer student programme.
I am really grateful to Dr. Elizaveta Shabalina for all her support and supervision within the last year. Additionally, for her sincerity in countless physics discussions, not only those that took place at late nights during the weekends, her willingness to patiently answer all my questions and her extraordinary knowledge in the field of particle physics. I am really thankful that I got the opportunity to work with her and to learn such a variety of things.
Many thanks goes to all the people that were willing to proof-read this thesis, especially to Dr. Elizaveta Shabalina, Dr. Kevin Kröninger, Jun.-Prof. Dr. Yvonne Peters and Chris Delitzsch. I know that time is always rare and thus I want to express my gratitude especially. Many thanks to the current and former PhD students and staff members of the 2nd Institute for all the interesting physics discussions, coffee breaks and constructive suggestions. Special thanks goes to Leonid Serkin and Olaf Nackenhorst. The network that exists and composes of former and current students of the institute generates a really unique atmosphere.
Beside the institute affiliates, I would like to express my gratitude to my lovely parents that extraordinarly supported me not only financial but mentally since I was born. They always showed understanding although some of my decisions in the past were not always the most logical and comprehensible ones. Furthermore, the fact that they never put any pressure on me and that they always encouraged me to make my own and free decisions in every area of my live formed my personality substantially. Thanks also to my sister and all of my friends. I am happy to be surrounded by people I love and appreciate. Thanks to everyone being appreciative of the lack of time I had within the last year.

Erklärung nach §18(8) der Prüfungsordnung für den Bachelor-Studiengang Physik und den Master-Studiengang Physik an der Universität Göttingen:

Hiermit erkläre ich, dass ich diese Abschlussarbeit selbständig verfasst habe, keine anderen als die angegebenen Quellen und Hilfsmittel benutzt habe und alle Stellen, die wörtlich oder sinngemäß aus veröffentlichten Schriften entnommen wurden, als solche kenntlich gemacht habe.
Darüberhinaus erkläre ich, dass diese Abschlussarbeit nicht, auch nicht auszugsweise, im Rahmen einer nichtbestandenen Prüfung an dieser oder einer anderen Hochschule eingereicht wurde.

Göttingen, den May 2, 2014

(Steffen Henkelmann)